Trigger Considerations for the Measurement of $B_s^0 \to D_s^- a_1^+$ with the ATLAS Experiment

Masterarbeit
zur Erlangung des akademischen Grades
Master of Science
(M.Sc.)

dem Fachbereich Physik der
Universität Siegen

vorgelegt von
B.Sc. Holger von Radziewski

Dezember 2007

Abstract

The ATLAS detector at the large hadron collider (LHC) will allow a broad range of studies in the field of particle physics, including the measurement of B_s^0 oscillations. The mixing analysis is based on reconstructing tagged B_s^0 decays, such as the fully hadronic $B_s^0 \to D_s^- a_1^+$ and $B_s^0 \to D_s^- \pi^+$ decay channels. The results may serve as input for a determination of $\Delta\Gamma_s$ and ϕ_s using $B_s^0 \to J/\psi(\mu^+\mu^-)\phi$ events.

In the high event rate environment of the LHC, an efficient trigger selection is indispensable. The trigger strategy for the $B_s^0 \to D_s^- a_1^+$ mixing analysis is based on the detection of a tagging muon and the reconstruction of $D_s^\mp$ particles by the high-level trigger.

In this thesis, an intermediate trigger efficiency is determined for the first-level muon trigger and the second-level $D_s^\mp$ trigger. The efficiency depends on the candidate search strategy used by the high-level trigger. A full scan within the inner detector offers an efficiency up to $(75.5 \pm 0.6)\,\%$ for reconstructable events, while a partial search only achieves $(68.9 \pm 0.7)\,\%$, but saves at least a factor of 2 of high-level trigger computing time due to less background hits.

Partial trigger rate estimates and a study of the computing power required by the second-level $D_s^\mp$ trigger are presented in order to assess how the $D_s^\mp$ trigger may be integrated into the trigger menu for low luminosities.

Contents

Part I

Physics Motivation

Chapter 1

Introduction to the Standard Model of Particle Physics

The subject of this thesis are trigger studies for the $B_s^0 \to D_s^- a_1^+$ channel, which can be used for probing oscillations of B_s^0 mesons (chapter 2). B_s^0 oscillations can be explained within the standard model (SM) [1–3] of particle physics (chapter 2) and constitute a means of probing several of the SM parameters.

1.1 Quarks and Leptons

Throughout this thesis, the convention

$$\boxed{\hbar = c = 1}$$

is used.

The particles of the SM are divided into the two groups of fermions (spin $S = \frac{1}{2} + n$) and bosons ($S = n$), $n = 0, 1, 2, \ldots$
The SM knows twelve fundamental types of particles with spin $\frac{1}{2}$ and their antiparticles. They can be arranged in six doublets.
The first three doublets

up-type, charge	$+\frac{2}{3}e$	$\begin{pmatrix} u \\ d \end{pmatrix}$	$\begin{pmatrix} c \\ s \end{pmatrix}$	$\begin{pmatrix} t \\ b \end{pmatrix}$
down-type, charge	$-\frac{1}{3}e$			
			increasing mass $\longrightarrow$	

represent the quarks, while the remaining doublets

charged leptons, charge	$-e$	$\begin{pmatrix} e \\ \nu_e \end{pmatrix}$	$\begin{pmatrix} \mu \\ \nu_\mu \end{pmatrix}$	$\begin{pmatrix} \tau \\ \nu_\tau \end{pmatrix}$
neutrinos, charge	0			

are the leptons (e is the elementary charge, see section 1.2).
The two times three doublets also represent the three generations of particles. The properties of the three quark doublets are similar, except for the masses. The same holds for the three generations of charged leptons (table 1.1). For neutrinos,

Table 1.1: Masses of elementary fermions [4]. The cited masses of the b and c quarks refer to the $\overline{\text{MS}}$ scheme. The t quark mass is obtained from Tevatron Run-I and Run-II (combined) [4].

Particle type	1^{st} generation mass [MeV]	2^{nd} generation mass [MeV]	3^{rd} generation mass [GeV]
up-type	$1.5 - 3.0$	1250 ± 90	174.2 ± 3.3
down-type	$3 - 7$	95 ± 25	4.20 ± 0.07
charged lepton	$0.51100 \pm 4 \times 10^{-8}$	$105.658 \pm 9 \times 10^{-6}$	$1.77699\,^{+\ 0.00029}_{-\ 0.00026}$

only upper bounds for the masses are known; the masses are non-zero, as proven by neutrino oscillation experiments. The mass hierarchy of the three generations cannot be derived intrinsically from the theoretical properties of the SM. This belongs to the most recognizable shortcomings of the SM.
Because the second- and third-generation charged fermions are each much heavier than the corresponding lower-generation particles and atoms are made only of first-generation fermions, the model of three generations evolved over time (see, e.g., [1]): Ever heavier particles were observed in astroparticle and accelerator experiments of increasing center-of-mass energies.
The existence of a fourth generation of leptons has experimentally been excluded [5]. Searches for fourth generation quarks have so far been without success [4].

1.2 Interactions and Composite Particles

SM particles participate in four types of interactions:

1. Gravity, which is not described by the SM, couples to the mass property of particles. In processes of particle physics, gravity can be neglected below the Planck scale, as its coupling constant is many orders of magnitude smaller than those of the SM interactions.

2. All particles with non-vanishing electric charges participate in the electromagnetic interaction, which is transmitted by photons.

3. The electromagnetic interaction is unified with the weak interaction in the electroweak interaction. The weak interaction couples to all fermions. It is transmitted via two types of massive exchange particles, the $W^{\pm}$ bosons with charge $\pm e$ and the neutral Z^0 boson.

4. The strong interaction couples to all quarks via 8 gluons, which each carry a color-anticolor pair of three colors. While quarks carry color, antiquarks carry anticolor. Observed particles are combinations of quarks: Mesons are states of a quark-antiquark pair (e.g., a $\bar{b}s$ quark pair forms a B_s^0 meson), baryons contain three quarks (valence quarks). In either case, the resulting particle has a vanishing color charge. Both types constitute the particle class of hadrons.

While the first two interaction types have long-range potentials proportional to r^{-1}, r being the distance, the third interaction is transmitted by massive particles and is hence a short-range interaction.
The strong force plays a special role because gluons can couple to other gluons (gluon self-coupling). This leads to the phenomenon of confinement: When the distance between the quarks increases, the potential energy of the gluon field reaches a level which allows the creation of quark-antiquark pairs. Therefore, particles like the proton contain in addition to the valence quarks uud numerous quark-antiquark pairs which are continuously produced and annihilate again (sea quarks).
These combinations only allow total charges that are integer multiples of e. Since leptons and antileptons always carry charges $\pm e$ or 0, all free particles (leptons and hadrons) therefore carry multiples of e, which is hence called the elementary charge.

Chapter 2

B_s^0 Oscillations

Section 2.1 explains how the observables from B_s^0 mixing analyses are connected to fundamental SM parameters. The time-dependent measurement of B_s^0 oscillations requires the reconstruction and discrimination of B_s^0 and $\bar{B}_s^0$ decays (section 2.2). At a hadron collider, this necessitates an efficient event selection already on the trigger level, as explained in section 2.3.

2.1 Theory of B_s^0 Oscillations

The SM interactions all conserve electromagnetic charge, color, lepton number, and baryon number. The electroweak interaction does not conserve quark flavor or lepton family numbers, though. While lepton family number violation gives rise to neutrino oscillations and to leptonic decays of heavy leptons, quark flavor violation is the base of flavor physics.
The coupling constants of $W^{\pm}$ bosons to quarks are given by the Cabibbo-Kobayashi-Maskawa (CKM) matrix elements for the various initial and final state flavors:

$$\begin{pmatrix} d \\ s \\ b \end{pmatrix} = \begin{pmatrix} V_{ud} & V_{us} & V_{ub} \\ V_{cd} & V_{cs} & V_{cb} \\ V_{td} & V_{ts} & V_{tb} \end{pmatrix} \begin{pmatrix} d' \\ s' \\ b' \end{pmatrix} \tag{2.1}$$

Hence, the determination of its entries plays a central role for flavor physics. The CKM matrix defines the unitary transformation between the mass eigenstates q' and the electro-weak eigenstates q [6, 7]. Applying the CKM matrix to the down-type quarks rather than their up-type partner quarks is convention.
The fact that the mass (or energy) eigenstates are no flavor eigenstates and vice versa leads to a non-diagonal form of the time evolution operator and therefore to particle-antiparticle mixing, i.e., the transformation of a neutral meson into its own antiparticle and vice versa [8, 9]. Let:

$$\begin{pmatrix} \alpha_1 \\ \alpha_2 \end{pmatrix} \equiv \alpha_1 \left| B_s^0 \right\rangle + \alpha_2 \left| \bar{B}_s^0 \right\rangle \qquad \text{with} \qquad |\alpha_1|^2 + |\alpha_2|^2 = 1$$

be a mixed state of a B_s^0 meson (consisting of a $\bar{b}s$ quark pair) and its antiparticle. In the case of a newly created B_s^0 (or $\bar{B}_s^0$) particle, the state is a flavor eigenstate

and hence has only one non-vanishing component:

$$\alpha_1 \cdot \alpha_2 = 0.$$

Its time evolution is given by the Schrödinger equation:

$$i\frac{d}{dt}\begin{pmatrix}\alpha_1(t)\\ \alpha_2(t)\end{pmatrix} = \left(\mathbf{M_s} - i\frac{\mathbf{\Gamma_s}}{2}\right)\begin{pmatrix}\alpha_1(t)\\ \alpha_2(t)\end{pmatrix} \tag{2.2}$$

with constant, Hermitian mass and decay matrices $\mathbf{M_s}$ and $i\mathbf{\Gamma_s}$.
The diagonal entries of $\mathbf{M_s}$ and $\mathbf{\Gamma_s}$ are equal due to the CPT theorem:

$$M_{s11} = M_{s22} = m_s \qquad \text{and} \qquad \Gamma_{s11} = \Gamma_{s22} = \Gamma_s,$$

and both matrices are symmetrical.
A base transformation leads to the time evolution of the mass eigenstates [8, 9]:

$$\left|B^0_{s\,L,H}\right\rangle = p\left|B^0_s\right\rangle \pm q\left|\bar{B}^0_s\right\rangle, \;\; |p|^2 + |q|^2 = 1 \tag{2.3}$$

$$\left(\mathbf{M_s} - i\frac{\mathbf{\Gamma_s}}{2}\right)\left|B^0_{s\,L,H}\right\rangle = \lambda_{L,H}\left|B^0_{s\,L,H}\right\rangle \Rightarrow \lambda_{L,H} = \left(m_s - \frac{i\Gamma_s}{2}\right) \pm \frac{q}{p}\left(M_{s12} - \frac{i\Gamma_{s12}}{2}\right) \tag{2.4}$$

and:

$$\frac{q}{p} = \sqrt{\frac{M^*_{s12} - \frac{i\Gamma^*_{s12}}{2}}{M_{s12} - \frac{i\Gamma_{s12}}{2}}}. \tag{2.5}$$

This allows the identification:

$$\lambda_{L,H} \equiv M_{L,H} - \frac{i\Gamma_{L,H}}{2}$$

with:

$$M_{L,H} = \mathrm{Re}(\lambda_{L,H}) \qquad \text{and} \qquad \Gamma_{L,H} = -2\mathrm{Im}(\lambda_{L,H}).$$

The time evolution operator for $\left|B^0_{s\,L,H}(t)\right\rangle$ can be expressed in terms of the eigenvalues $\lambda_{L,H}$:

$$\left|B^0_{s\,L,H}(t)\right\rangle = e^{-i\lambda_{L,H}t}\left|B^0_{s\,L,H}\right\rangle, \tag{2.6}$$

which, using (2.4), leads to the conclusion that the average mass and width of the mass eigenstates are equal to the properties of the flavor eigenstates:

$$\frac{M_H + M_L}{2} = m_s \qquad \text{and} \qquad \frac{\Gamma_H + \Gamma_L}{2} = \Gamma_s. \tag{2.7}$$

Equation (2.6) describes the time evolution of the mass eigenstates. We now use (2.3) to derive the time evolution of the initial state, which is either a $\left|B^0_s\right\rangle$ or a $\left|\bar{B}^0_s\right\rangle$ flavor eigenstate [8, 9]:

$$\begin{aligned}\left|B^0_s(t)\right\rangle &= \;\; g_+(t)\left|B^0_s\right\rangle + \frac{q}{p}g_-(t)\left|\bar{B}^0_s\right\rangle \\ \left|\bar{B}^0_s(t)\right\rangle &= \frac{p}{q}g_-(t)\left|B^0_s\right\rangle + \;\; g_+(t)\left|\bar{B}^0_s\right\rangle\end{aligned} \tag{2.8}$$

with:

$$\begin{aligned} g_{\pm}(t) &= \frac{1}{2}\left(e^{-i\lambda_L t} \pm e^{-i\lambda_H t}\right) \\ &= \frac{1}{2}\left(e^{-(iM_L+\frac{1}{2}\Gamma_L)t} \pm e^{-(iM_H+\frac{1}{2}\Gamma_H)t}\right) \qquad (2.9) \\ \overset{(2.7)}{\Rightarrow} |g_{\pm}(t)|^2 &= \frac{1}{2}e^{-\Gamma_s t}\left[\cosh\left(\frac{(\Gamma_L-\Gamma_H)t}{2}\right) \pm \cos\left((M_H-M_L)t\right)\right]. \qquad (2.10) \end{aligned}$$

At this point, we introduce the two positive quantities:

$$\Delta m_s \equiv M_H - M_L \qquad \text{and} \qquad \Delta\Gamma_s \equiv \Gamma_L - \Gamma_H, \qquad (2.11)$$

which determine the time evolution of the oscillating mesons. After calculating the norms of (2.8):

$$\begin{aligned} \eta^2 \equiv \left|\left|B_s^0(t)\right\rangle\right|^2 &= \int_0^\infty dt \left\langle B_s^0(t) \left| B_s^0(t)\right\rangle = \right. \frac{\Gamma_s}{2}\left(\frac{1+\left|\frac{q}{p}\right|^2}{\Gamma_s^2 - \frac{(\Delta\Gamma_s)^2}{4}} + \frac{1-\left|\frac{q}{p}\right|^2}{\Gamma_s^2+(\Delta m_s)^2}\right), \\ \bar{\eta}^2 \equiv \left|\left|\bar{B}_s^0(t)\right\rangle\right|^2 &= \int_0^\infty dt \left\langle \bar{B}_s^0(t) \left| \bar{B}_s^0(t)\right\rangle = \left|\frac{p}{q}\right|^2 \frac{\Gamma_s}{2}\left(\frac{1+\left|\frac{q}{p}\right|^2}{\Gamma_s^2 - \frac{(\Delta\Gamma_s)^2}{4}} - \frac{1-\left|\frac{q}{p}\right|^2}{\Gamma_s^2+(\Delta m_s)^2}\right), \end{aligned} \qquad (2.12)$$

we can calculate the the mixing and survival probabilities [8, 9]:

$$\begin{aligned} \mathcal{P}_{\text{mixing}}(t)\left(B_s^0 \to \bar{B}_s^0\right) &= \frac{1}{\bar{\eta}^2}\left|\left\langle B_s^0 \left|\bar{B}_s^0(t)\right\rangle\right|^2 = \frac{1}{\bar{\eta}^2}\left|\frac{p}{q}\right|^2 |g_-(t)|^2 \\ &= \frac{2}{\Gamma_s}\left(\underbrace{\frac{1+\left|\frac{q}{p}\right|^2}{\Gamma_s^2 - \frac{(\Delta\Gamma_s)^2}{4}}}_{\equiv a} - \underbrace{\frac{1-\left|\frac{q}{p}\right|^2}{\Gamma_s^2+(\Delta m_s)^2}}_{\equiv b}\right)^{-1} \\ &\quad \times \frac{1}{2}e^{-\Gamma_s t}\left[\cosh\left(\frac{\Delta\Gamma_s t}{2}\right) - \cos\left(\Delta m_s t\right)\right], \qquad (2.13) \\ \mathcal{P}_{\text{mixing}}(t)\left(\bar{B}_s^0 \to B_s^0\right) &= \frac{1}{\eta^2}\left|\left\langle \bar{B}_s^0 \left|B_s^0(t)\right\rangle\right|^2 = \frac{1}{\eta^2}\left|\frac{q}{p}\right|^2 |g_-(t)|^2 \\ &= \frac{2}{\Gamma_s}(a+b)^{-1}\left|\frac{q}{p}\right|^2 \times \frac{1}{2}e^{-\Gamma_s t}\left[\cosh\left(\frac{\Delta\Gamma_s t}{2}\right) - \cos\left(\Delta m_s t\right)\right], \end{aligned} \qquad (2.14)$$

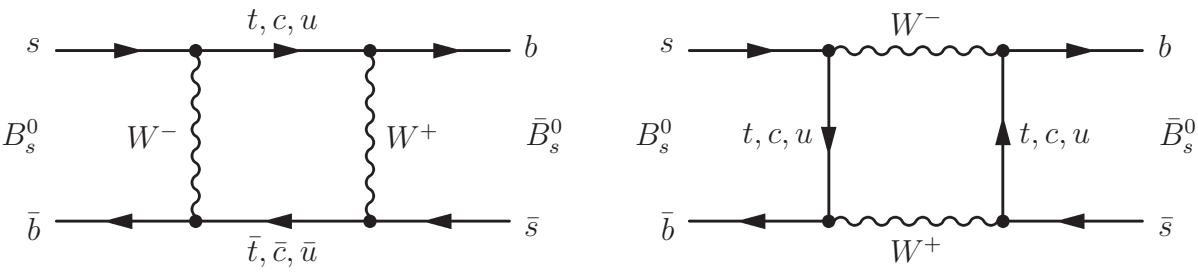

Figure 2.1: Lowest order Feynman diagrams for B_s^0 oscillations [12].

$$\begin{aligned}\mathcal{P}_{\text{survival}}(t)\left(B_s^0 \to B_s^0\right) &= \frac{1}{\eta^2}\left|\left\langle B_s^0 \left| B_s^0(t)\right\rangle\right|^2 = \frac{1}{\eta^2}\left|g_+(t)\right|^2 \\ &= \frac{2}{\Gamma_s}\left(a+b\right)^{-1} \quad \times \frac{1}{2}e^{-\Gamma_s t}\left[\cosh\left(\frac{\Delta\Gamma_s t}{2}\right) + \cos\left(\Delta m_s t\right)\right], \end{aligned} \tag{2.15}$$

$$\begin{aligned}\mathcal{P}_{\text{survival}}(t)\left(\bar{B}_s^0 \to \bar{B}_s^0\right) &= \frac{1}{\bar{\eta}^2}\left|\left\langle \bar{B}_s^0 \left| \bar{B}_s^0(t)\right\rangle\right|^2 = \frac{1}{\bar{\eta}^2}\left|g_+(t)\right|^2 \\ &= \frac{2}{\Gamma_s}\left(a-b\right)^{-1}\left|\frac{q}{p}\right|^2 \times \frac{1}{2}e^{-\Gamma_s t}\left[\cosh\left(\frac{\Delta\Gamma_s t}{2}\right) + \cos\left(\Delta m_s t\right)\right]. \end{aligned} \tag{2.16}$$

Neglecting CP violation, which is expected to be small in the B_s^0-$\bar{B}_s^0$ system [10,11], by setting:

$$\frac{q}{p} = 1, \tag{2.17}$$

the mixing and survival probabilities for B_s^0 and $\bar{B}_s^0$ mesons no longer discriminate between particle-to-antiparticle oscillations and antiparticle-to-particle oscillations:

$$\begin{aligned}\mathcal{P}_{\text{mixing}}(t)\ \left(B_s^0 \to \bar{B}_s^0\right) &= \mathcal{P}_{\text{mixing}}(t)\ \left(\bar{B}_s^0 \to B_s^0\right) \\ &= \frac{\Gamma}{2}e^{-\Gamma t}\left(1 - \frac{(\Delta\Gamma)^2}{4\Gamma^2}\right)\left[\cosh\left(\frac{\Delta\Gamma t}{2}\right) - \cos\left(\Delta m t\right)\right], \end{aligned} \tag{2.18}$$

$$\begin{aligned}\mathcal{P}_{\text{survival}}(t)\left(B_s^0 \to B_s^0\right) &= \mathcal{P}_{\text{survival}}(t)\left(\bar{B}_s^0 \to \bar{B}_s^0\right) \\ &= \frac{\Gamma}{2}e^{-\Gamma t}\left(1 - \frac{(\Delta\Gamma)^2}{4\Gamma^2}\right)\left[\cosh\left(\frac{\Delta\Gamma t}{2}\right) + \cos\left(\Delta m t\right)\right]. \end{aligned} \tag{2.19}$$

The two SM mixing processes of lowest order (figure 2.1) involve two charged current reactions and are dominated by the t quark contributions for the quark propagators.

2.2 Measurement Principle

In order to measure the quantities $\Delta\Gamma_s$ and Δm_s, a mixing analysis must be able to:

1. identify the decay of a B_s^0 meson or a $\bar{B}_s^0$ meson (decay reconstruction, section 7.1),

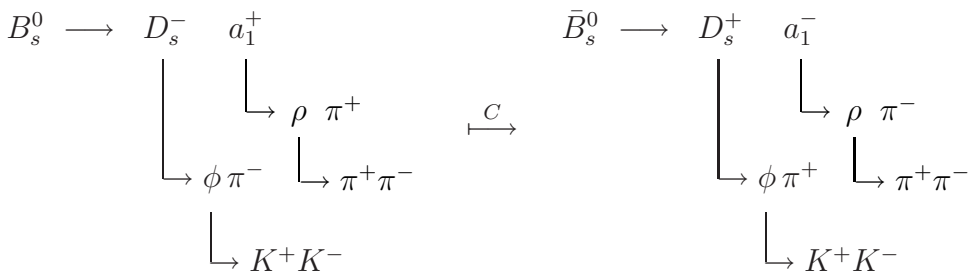

Figure 2.2: Signal topology of the $B_s^0 \to D_s^- a_1^+$ decay channel and the charge conjugated decay.

2. determine whether the meson was created as a particle or as an antiparticle (tagging), and

3. reconstruct the distance between the creation vertex and the decay vertex of the B_s^0 or $\bar{B}_s^0$ meson and its momentum. This allows the calculation of the proper decay time, which is equivalent to t in (2.13) to (2.16).

To meet the first and third requirement, the mixing analysis [12] (see also section 7.1) limits itself to the fully hadronic decay chain $B_s^0 \to D_s^- a_1^+$ plus the associated $\bar{B}_s^0$ decay (figure 2.2). It thus measures Δm_s using fully reconstructable events.
Events are tagged by requiring the decay of the b quark produced in association with the $\bar{b}$ quark from the signal channel to contain a muon (or an antimuon for the charge conjugated decay). In case of a charged production reaction $W^- \to \mu^- \nu_\mu$, the charge of the tagging muon is correlated with the initial state on the signal side (other-side tagging).
The mixing analysis using the $B_s^0 \to D_s^- a_1^+$ channel complements the study of the $B_s^0 \to D_s^- \pi^+$ channel, whose topology only differs in the particle produced in association with the D_s^- and which also supplies a means of measuring Δm_s. Both efforts are being combined in [13].
The results of these mixing analyses will be fed into the $B_s^0 \to J/\psi(\mu^+\mu^-)\phi$ analysis for determining $\Delta\Gamma_s$ and the CP violating phase ϕ_s. Because all final state particles of the $B_s^0 \to D_s^- a_1^+$ channel are charged hadrons, their tracks can be used to reconstruct the decay vertex and the four momentum of the B_s^0 meson.

2.3 Event Selection Requirements

The above studies will be performed on data from a pp collider at a center of mass energy of 14 TeV and a bunch crossing rate of 40 MHz (see also chapter 4). Due to the complexity of the events, only a small fraction of the events can be recorded (section 5.2).
The total cross-section for pp reactions is concluded from cosmic ray experiments (figure 2.3) to be of the order $\mathcal{O}(100\,\text{mb})$. This is eight orders of magnitude larger than the signal cross-section for $B_s^0 \to D_s^- a_1^+$ requiring an additional muon of a

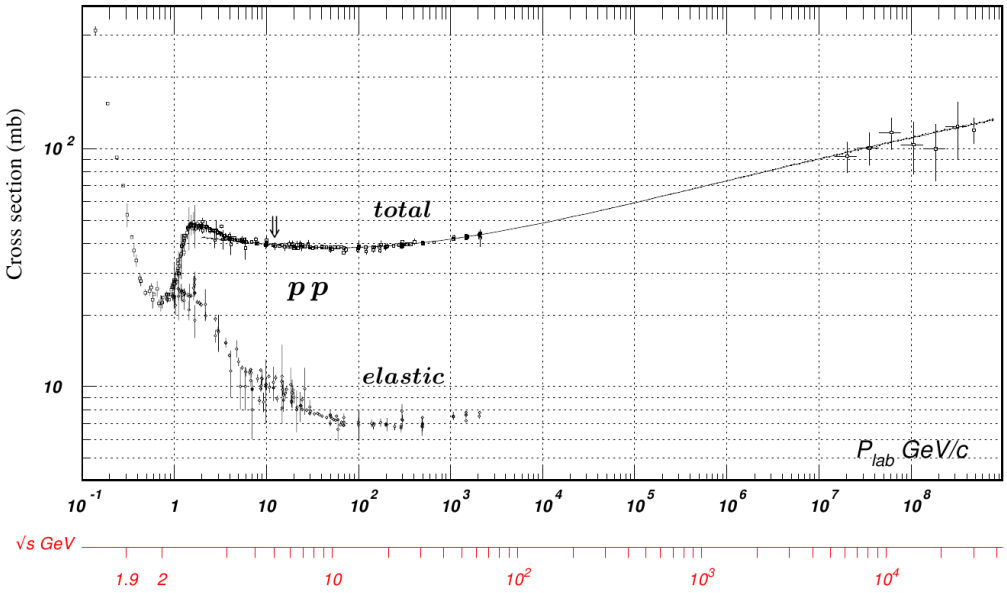

Figure 2.3: Cross-section of pp reactions in dependence of the center-of-mass energy (lower scale) [4]. For LHC energies $\sqrt{s} \approx 14\,\text{TeV}$, only results from cosmic ray air shower measurements are available. Other hadron accelerators capable of achieving intermediate energies were designed as $p\bar{p}$ colliders.

transverse momentum p_T of 6 GeV or more for tagging. This value is estimated from PythiaB (see also section 6.1.1) studies to be $(6 \pm 3)\,\text{nb}$, taking into account the large uncertainty of the branching ratio of $B_s^0 \to D_s^- a_1^+$, which is concluded from the branching ratio of the $B^0 \to D^- a_1^+$ process [14]. Background cross-sections like $b\bar{b} \to X$ (with the same muon requirement) are estimated to be $(6.144 \pm 0.016)\,\mu\text{b}$ [15]. The uncertainty on the production cross-sections for b quark pairs, which affects both signal and background cross-sections, is estimated to be a factor of 2 in either direction [16]. In contrast to most pp processes, the detector signature of this background channel resembles the signal, as it contains jets and a potential tagging muon. This similarity necessitates the use of tracking data within trigger algorithms in order to reject background events while maintaining a high efficiency for signal events.
Also, this preselection heavily affects the prospects of the offline mixing analysis, as the trigger strategy may introduce a bias by rejecting signal events and therefore affects the number of events available.

2.4 Previous Measurements

The mixing of B mesons has first been observed by the ARGUS [17, 18] and CLEO [19] collaborations in the B^0-$\bar{B}^0$ system. A B^0 meson consists of a $\bar{b}d$ quark-antiquark pair. Neither detector could resolve B^0 decay lengths sufficiently accurately for a time-dependent analysis. Hence, results for the mixing parameter Δm_d (defined in analogy to (2.11)) of B^0 mesons could only be deduced from counting B^0 decays and $\bar{B}^0$ decays in tagged events, which does not yield a level of precision which is

competitive to results from time-dependent analyses.
The mixing of B mesons has been extensively analyzed for B^0 mesons by the ALEPH, BABAR, Belle, CDF, DØ, DELPHI, L3, and OPAL collaborations. The world average result is dominated by the B factories BABAR and Belle [20]:

$$\Delta m_d = (0.508 \pm 0.003\,(\text{stat.}) \pm 0.003\,(\text{sys.}))\,\text{ps}^{-1}.$$

In contrast to B_s^0-$\bar{B}_s^0$ oscillations, the value of $\frac{\Delta\Gamma_d}{\Gamma_d}$ is negligible for B^0-$\bar{B}^0$ mixing [21]:

$$\frac{\Delta\Gamma_d}{\Gamma_d} < 0.18 \text{ at } 95\% \text{ confidence level},$$

while:

$$\frac{\Delta\Gamma_s}{\Gamma_s} \in [-0.01, +0.51] \text{ at } 95\% \text{ confidence level},$$
$$\frac{\Delta\Gamma_s}{\Gamma_s} = +0.206\ ^{+\ 0.106}_{-\ 0.111}$$

is concluded in [20].
In the B_s^0-$\bar{B}_s^0$ system, experiments with center-of-mass energies below the order $\mathcal{O}(1\,\text{TeV})$ cannot resolve Δm_s, as the oscillation length is smaller by a factor of $\frac{\Delta m_d}{\Delta m_s}$, compared to B^0-$\bar{B}^0$ oscillations. For Δm_s, DØ obtained [22] a direct two-sided bound of:

$$17\,\text{ps}^{-1} < \Delta m_s < 21\,\text{ps}^{-1} \text{ at } 90\% \text{ confidence level},$$

shortly followed by the first observation of B_s^0 oscillations at CDF [23]:

$$\Delta m_s = (17.77 \pm 0.10\,(\text{stat.}) \pm 0.07\,(\text{sys.}))\,\text{ps}^{-1}.$$

Chapter 3

Scope of this Thesis

This thesis summarizes the trigger studies performed for the $B_s^0 \to D_s^- a_1^+$ analysis with ATLAS.
After the introduction into the physics motivation in part I, part II briefly describes the experimental setup, consisting of the large hadron collider (chapter 4) and the ATLAS detector (chapter 5). Section 5.2 introduces the trigger strategy.
Part III explains the analysis technique employed: Chapter 6 introduces the production of Monte Carlo data, and chapter 7 introduces the main aspects of the offline analysis and of the trigger studies for the $B_s^0 \to D_s^- a_1^+$ channel.
Part IV presents the results of the trigger studies:

- Chapter 8 evaluates the bias, that each part of the trigger selection imposes on the kinematic distributions of the particles involved in the signal.
- Chapter 9 summarizes trigger efficiencies of the different trigger items involved. Results for signal efficiencies and background rejections are given as well as a discussion how these quantities are affected by different trigger settings.
- Chapter 10 gives an overview of the impact of the trigger on the number of events available for the mixing analysis and describes which background event rates the LVL2 trigger has to deal with.
- Chapter 11 uses the results from chapters 9 and 10 to evaluate the computing time requirements of the $D_s^\mp$ trigger signature and states important next steps for the trigger studies for the $B_s^0 \to D_s^- a_1^+$ analysis.
- Chapter 12 summarizes part IV.

Part II

ATLAS Experiment

Chapter 4

Large Hadron Collider

The large hadron collider (LHC) is a two-ring synchrotron, employing superconducting magnets, currently under construction in the circular tunnel formerly used by the large electron-positron collider (LEP). It is part of the European laboratory for particle physics (CERN) in Geneva. The LHC will be operated alternately to collide protons (pp mode) and to provide heavy-ion collisions. The latter mode is not discussed within this thesis.
The LHC will provide hadron-hadron collisions for four major detectors, which are introduced in section 4.2 and chapter 5. While the ATLAS and CMS detectors require pp collisions at high luminosity for their main physics programs, the demands of LHC-b and ALICE differ.

4.1 Specifications

For the particle acceleration, the CERN accelerator chain, consisting of a linear accelerator, a booster, a proton synchrotron, and the super proton synchrotron, is used for injection of the hadrons (figure 4.1) [25].
In the case of pp operation, the relativistic energy of the injected protons is 450 GeV per proton. The given circumference of the LEP tunnel [25] dictates the circumference of the LHC ring:

$$2\pi r = 26\,660\,\mathrm{m}.$$

The magnetic dipole field for the superconducting dipole magnets of the LHC has a nominal value [25] of:

$$B = 8.33\,\mathrm{T}.$$

For the design of the LHC, this allows a maximal center-of-mass energy of:

$$\sqrt{s} = 14\,\mathrm{TeV} \text{ for } pp \text{ collisions [25]},$$

which is a factor of seven higher than the corresponding value for $p\bar{p}$ collisions at the TEVATRON [26].

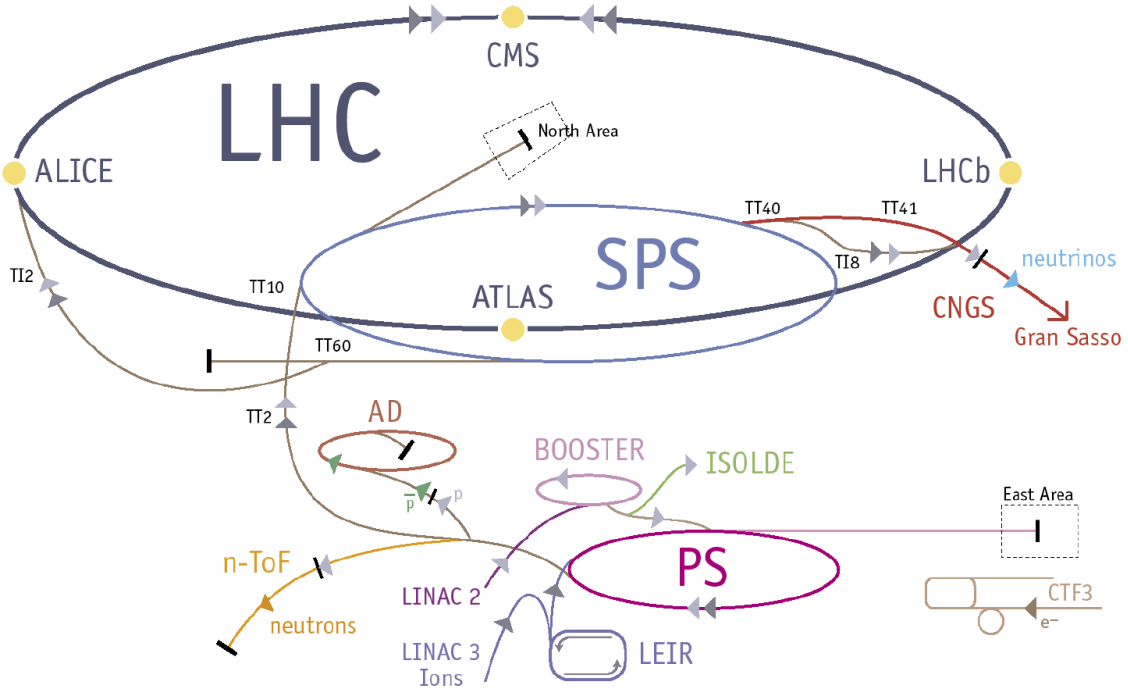

Figure 4.1: Schematic view of the CERN accelerators [24].

The beams will consist of up to 2808 bunches per beam, each containing up to 1.15×10^{11} protons. A peak luminosity of $\mathcal{L} = 10^{34}\,\mathrm{cm}^{-2}\mathrm{s}^{-1}$ for the interaction points of the ATLAS and CMS detectors can be achieved [25].
However, the LHC will be operated at lower luminosities at the beginning. A scenario used for the preparation of physics analyses [16] anticipates:

1. an initial luminosity of $\mathcal{L} = 10^{31}\,\mathrm{cm}^{-2}\mathrm{s}^{-1}$, followed by
2. a luminosity of $\mathcal{L} = 10^{32}\,\mathrm{cm}^{-2}\mathrm{s}^{-1}$ up to a total integrated luminosity of about $100\,\mathrm{pb}^{-1}$.
3. Several fb^{-1} shall be collected at $\mathcal{L} = 10^{33}\,\mathrm{cm}^{-2}\mathrm{s}^{-1}$ and $\mathcal{L} = 2 \times 10^{33}\,\mathrm{cm}^{-2}\mathrm{s}^{-1}$, before
4. the LHC runs at the design luminosity of $\mathcal{L} = 10^{34}\,\mathrm{cm}^{-2}\mathrm{s}^{-1}$.

The exact luminosity evolution depends on various circumstances, especially the status of beam and detector commissioning.
As the luminosity is increased to above $\mathcal{O}(10^{32}\,\mathrm{cm}^{-2}\mathrm{s}^{-1})$, the pp interaction cross-section estimates indicate there will be more than one pp interaction per event on average (pileup). As the root mean square of the bunch length is about 7.55 cm, the coordinate of the reconstructed primary interaction vertices along the beam axis can be used to separate final state particles from the various interactions. For pp running, about 2.3 interactions per event are anticipated for $\mathcal{L} = 10^{33}\,\mathrm{cm}^{-2}\mathrm{s}^{-1}$ and 23 interactions per event for the design luminosity. The consequences of pileup are not taken into consideration within this thesis.

4.2 Major Experiments

4.2.1 ALICE Experiment

A large ion collider experiment (ALICE) [27] is designed mainly to study the physics of heavy-ion collisions, especially properties of the quark-gluon plasma. Besides collisions of lead ions, studies of collisions of lighter ions and of protons are anticipated. pp collision studies are mainly used to provide reference data for heavy ion physics, but they are also part of the ALICE physics program [27].
For particle detection, ALICE possesses a central detector inside a large solenoid for the measurement of hadrons, electrons, and photons as well as a forward muon detector on one side. The central detector covers the polar angle range $45\,^\circ < \theta < 135\,^\circ$ (measured from the beam axis pointing forward). It consists of an inner tracking system which employs silicon detectors, a time projection chamber, and three subdetectors for particle identification: a time-of-flight detector, a ring imaging Cherenkov detector, and a transition radiation detector. The muon spectrometer covers the polar angle range $2\,^\circ < \theta < 9\,^\circ$ of the forward region. The ALICE trigger system consists of trigger chambers in the forward detector and a scintillator array to select cosmic radiation events [27].

4.2.2 ATLAS Detector

The ATLAS detector is introduced in chapter 5.

4.2.3 CMS Detector

The compact muon solenoid (CMS) is a general-purpose detector. Its capabilities complement those of the ATLAS detector. The design of the CMS detector is dominated by a large superconducting solenoid providing a magnetic field of 4 T for the tracking and calorimeter regions. The return field is conducted through iron plates which also serve as absorbers for the muon spectrometer. They make the CMS detector the heaviest of the four large LHC detectors [28].
The CMS detector possesses a silicon pixel detector and a silicon microstrip detector. The calorimetry consists of a lead tungstate scintillator calorimeter and a brass/scintillator sampling hadron calorimeter. The high magnetic field of the solenoid allows a good momentum resolution up to the highest momenta accessible at the LHC. For muons, this is achieved by four consecutive muon stations [28].

4.2.4 LHC-b Detector

The LHC-b detector is a dedicated apparatus for studies of B-physics and CP violation at the LHC. Due to the large number of b-quark pairs produced in pp collisions with momenta almost parallel to the beam axis, the LHC-b detector is assembled completely on one side of the interaction point [29], so that the detector geometry resembles that of a fixed-target experiment. A vertex detector provides precise resolution of the decay vertices. It is followed by a ring imaging Cherenkov detector

(for particle identification) and the tracking system, a part of which is located inside the field of a dipole magnet for momentum resolution. Another ring imaging Cherenkov detector, calorimeters, and muon detectors complete the detector. The entire detector covers the polar angle range (measured from the forward direction) of 10 to 300 mrad for the bending plane of charged particles and 10 to 250 mrad in the perpendicular plane [29].
Because of the large cross-section for b-quark production, the LHC-b detector is designed for a luminosity of $\mathcal{L} = 10^{32}\,\mathrm{cm}^{-2}\mathrm{s}^{-1}$ to avoid effects of pileup (section 4.1). It can therefore only be operated at lower luminosities than the ATLAS and CMS detectors [25]. Due to the good coverage of the forward direction and the optimization of the physics program for B-physics, the LHC-b detector will be able to collect a large number of B-physics events at $\mathcal{L} = 10^{32}\,\mathrm{cm}^{-2}\mathrm{s}^{-1}$, even more than the other experiments at the design luminosity of the LHC.

Chapter 5

ATLAS Detector

This chapter describes the features of the ATLAS detector in general (section 5.1) and its trigger system (section 5.2).

ATLAS Coordinate System

Throughout this thesis, space coordinates refer to the ATLAS coordinate system [30] and the derived spherical (r, ϕ, θ) or cylindrical (r, ϕ, z) coordinate systems:

- The x-axis points to the center of the LHC ring.
- The y-axis points upwards.
- The z-axis completes a right-handed coordinate system: $\vec{e}_z = \vec{e}_x \times \vec{e}_y$.

The pseudorapidity η is defined in terms of the azimuthal angle θ [30]:

$$\eta = -\ln \tan\left(\frac{\theta}{2}\right)$$

5.1 Detector Parts and Magnetic Field Layout

The ATLAS detector (proposed in [31], figure 5.1) is a general-purpose detector. The name, a toroidal LHC apparatus (ATLAS), hints at the most visible design feature, i.e., the toroidal magnet layout in the outermost detector part.
From the interaction point outwards, the ATLAS detector consists of the inner detector, the electromagnetic and hadronic calorimeters, and the muon spectrometer. The inner detector operates inside a superconducting air-core solenoid, the central solenoid, which provides a magnetic field of 2 T. Outside the solenoid, the electromagnetic and hadronic calorimeters are situated. They are surrounded by the muon spectrometer, most of which lies within the field of superconducting air-core toroid magnets, maintaining a peak field of 3.9 T in the barrel toroid magnet and up to 4.1 T in the end-cap toroid magnets [30].
Because of the described layout of the magnetic fields, the tracks of charged particles are bent in the r-ϕ plane within the central solenoid and in the r-z plane as they pass through the toroid magnets.

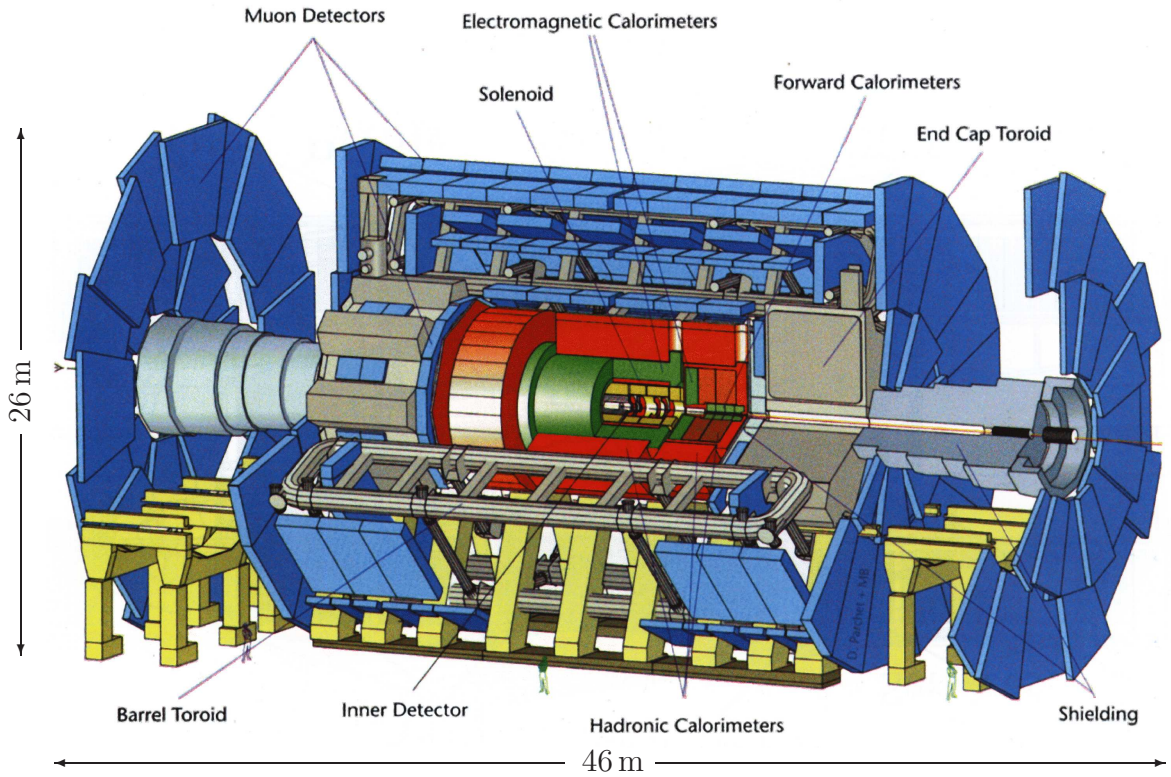

Figure 5.1: The ATLAS detector [30]. The general layout is described in section 5.1.

Each sub-detector consists of parts covering the transverse region ($|\eta|$ small), called barrels, and parts covering the forward directions ($|\eta|$ large), called end-caps.

5.1.1 Inner Detector

The goal of the inner detector (figure 5.2) is to provide precision tracking data while minimizing multiple scattering of particles.

In order to achieve this, the inner detector consists of a silicon pixel detector (situated nearest to the interaction point), a silicon microstrip detector, called the semiconductor tracker (SCT), and a straw-tube tracker, which is called transition radiation tracker (TRT), all placed within the magnetic field of the central solenoid [30].

By this design, the space-point resolution is maximized in the area nearest to the interaction point, containing three pixel layers (typical pixel size $50 \times 400\,\mu$m) and eight SCT strip layers (four times two small-angle stereo layers with a strip pitch of $80\,\mu$m). The limiting factors for the number of layers of silicon detectors are the amount of material introduced and costs. In order to improve the tracking, the straw tubes (4 mm in diameter) of the TRT add about 36 space points per track [30]. The TRT also supplies a means to discriminate between electrons and photons, as signals from transition radiation (originating from the passage of a charged particle through a radiator between the straws) pass a higher readout threshold than signals from ionizations by the incident particle [30].

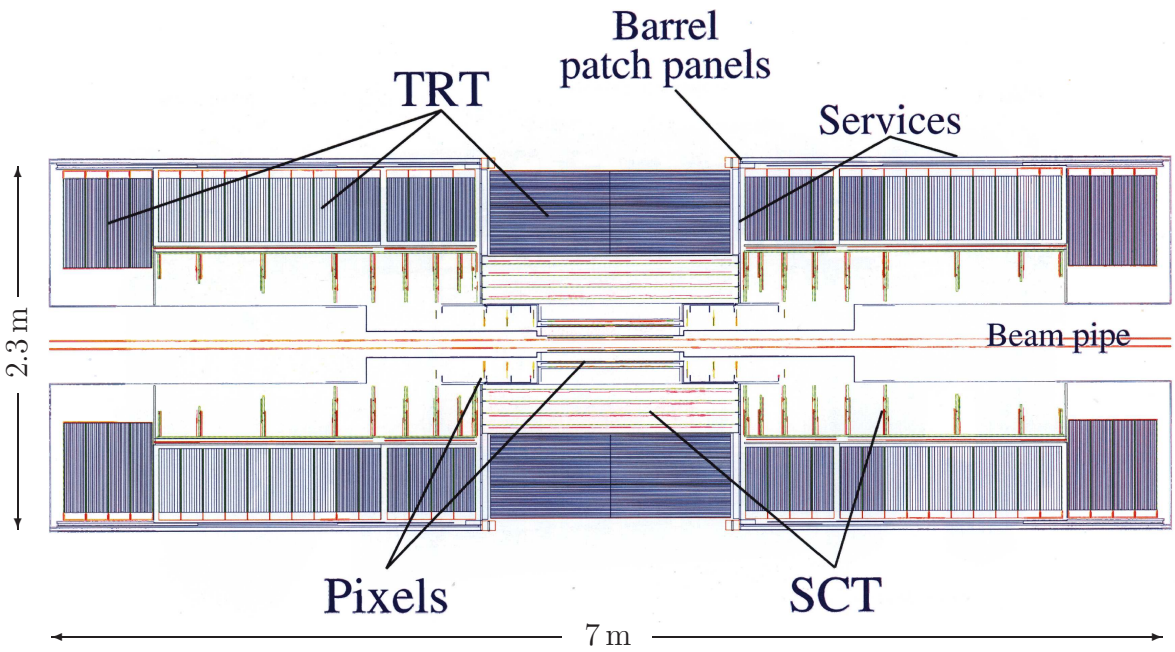

Figure 5.2: The ATLAS inner detector [30]. Section 5.1.1 explains the sub-detectors.

5.1.2 Calorimeters

Outside the central solenoid, the electromagnetic and hadronic calorimeters are placed (figure 5.3). As the electromagnetic calorimeter is to measure energy deposited by less penetrating particles than the hadronic calorimeters, it is placed closer to the interaction point.

The electromagnetic sampling calorimeters strive for a higher energy resolution than the hadronic calorimeters to enhance the resolution for jet energy and missing energy. The electromagnetic calorimeters feature a finer granularity than the hadronic calorimeters. In order to resolve the entrance point of the incident particle of the shower more precisely, the innermost sampling of the electromagnetic calorimeters (to a depth of about six radiation lengths X_0) provides increased precision in the central detector region ($|\eta| < 2.5$) [30].

The hadronic scintillator-tile calorimeter (used in the barrel region, covering pseudorapidities up to $|\eta| \approx 1.7$) and the hadronic end-cap calorimeter (covering the pseudorapidity range $1.5 < |\eta| < 3.2$) are shielded from the interaction point by the tracking detectors and the electromagnetic calorimeter, which are in total equivalent to approximately 1.2 hadronic interaction lengths or about $25X_0$. Both the electromagnetic and hadronic calorimeter systems extend to $|\eta| \approx 3.2$ [30].

Because the overall detector dimensions do not permit the use of both a dedicated electromagnetic and a dedicated hadronic calorimeter for $|\eta| > 3.2$, the region up to $|\eta| \approx 4.9$ is covered by a high-density forward calorimeter to contain the hadronic showers on a short range [30]. To preserve a good energy resolution for electromagnetic showers, the section closest to the interaction point uses copper (while the other two sections use tungsten). Also, the granularity becomes coarser from the section closest to the interaction point (cell size $2.0\,\mathrm{cm}^2$) outwards (cell size in the outer section $5.6\,\mathrm{cm}^2$) [33].

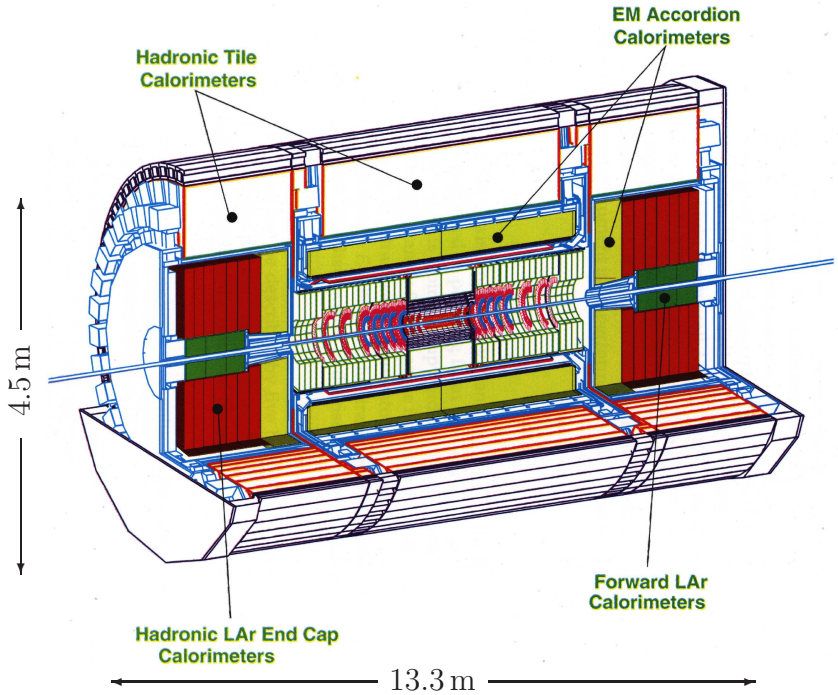

Figure 5.3: The ATLAS calorimeter system [30]. The word "accordion" alludes to the folded shape of the Kapton electrodes and lead absorber plates in the electromagnetic calorimeters, which enhances ϕ symmetry [30, 32].

While the time resolutions of the electromagnetic and hadronic calorimeters are of the order of a few nanoseconds, their signal peaking times of about 40 ns are longer than the bunch crossing period of 25 ns. This leads to a so-called pileup effect: Hits from previous bunch crossings show in consecutive events [32]. This effect must not be confused with the overlay effect that occurs for more than one *pp* reaction per bunch crossing, which is also called pileup (section 4.1).

5.1.3 Muon Spectrometer

The muon spectrometer (figure 5.4) is located outside the calorimeter system, covering the volume of the air-core toroid magnets, which provide a large magnetic field volume while minimizing multiple scattering. The muon spectrometer defines the overall dimensions of the ATLAS experiment: The barrel part consists of three stations at radii of approximately 5 m, 7.5 m, and 10 m. The end-cap region also contains three muon stations, the third set of which is placed at $z = \pm 23$ m [30].
Because muon detectors cannot simultaneously offer both the required spatial resolution for precision physics and the time resolution needed for triggering on single bunch crossings, both dedicated trigger chambers and separate precision chambers are used in the muon spectrometer [30].
For the precision chambers, monitored drift tubes (MDTs) are used in the barrel region and all but the innermost end-caps, offering a single wire resolution of about 80 μm with a maximum drift time of approximately 700 ns. In regions exposed to higher rates (the part of the innermost end-cap with $2 < |\eta| < 2.7$), cathode strip

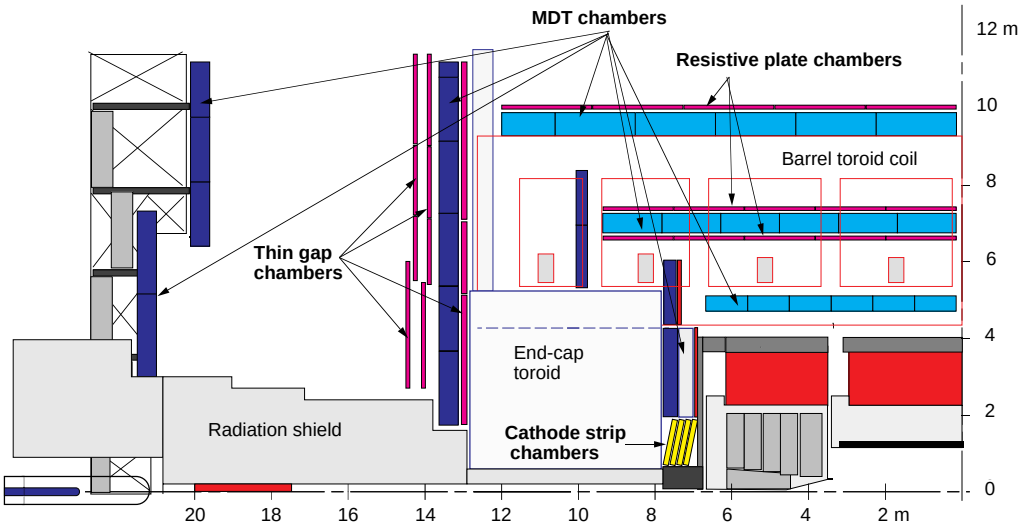

Figure 5.4: The ATLAS muon spectrometer (1/4 section) [34]. The sketch shows the central gap in the muon system: In the plane with $z = 0$, cables and services of the inner detector, the central solenoid, and the calorimeters are led out of the detector, which does not allow the placement of muon chambers [30].

chambers are employed, as they offer lower drift times of about 30 ns [34]. The trigger chambers are described in section 5.2.2.
In the barrel part, the muon spectrometer precision stations lie before, within, and right behind the toroid coils. Two trigger stations are located within the coils and one behind the toroid magnet. The end-cap muon system also has one precision chamber station placed before the toroid, with cathode strip chambers covering the region exposed to the highest rates. The middle precision chamber station and all three trigger stations are placed right behind the end-cap toroid, followed at a distance of about 6 m by the third precision chamber. From three muon track points, the muon momentum is determined. Due to the size of the muon spectrometer, the position and deformation of each of its parts is monitored to optimize precision [30]. As the η coordinate limits the momentum resolution, precision chambers are only used to resolve this coordinate — with the exception of the innermost barrel, which employs two orthogonal layers of precision chambers only. Throughout the rest of the muon spectrometer, the η coordinate of hits is measured both by precision and trigger chambers, while the ϕ coordinates are measured only by trigger chambers (section 5.2.2) [34].

5.2 ATLAS Trigger System

The LHC will provide bunch crossings every 25 ns, corresponding to an event rate of 40 MHz. As the readout of ATLAS events corresponds to about 1.5 MBytes of detector data every 25 ns, a trigger system must select the data relevant to physics analyses online for storage ($\mathcal{O}(100\,\text{Hz})$ total from all signatures in the trigger menu) and discard all other events [35], resulting mostly from minimum bias processes [36].

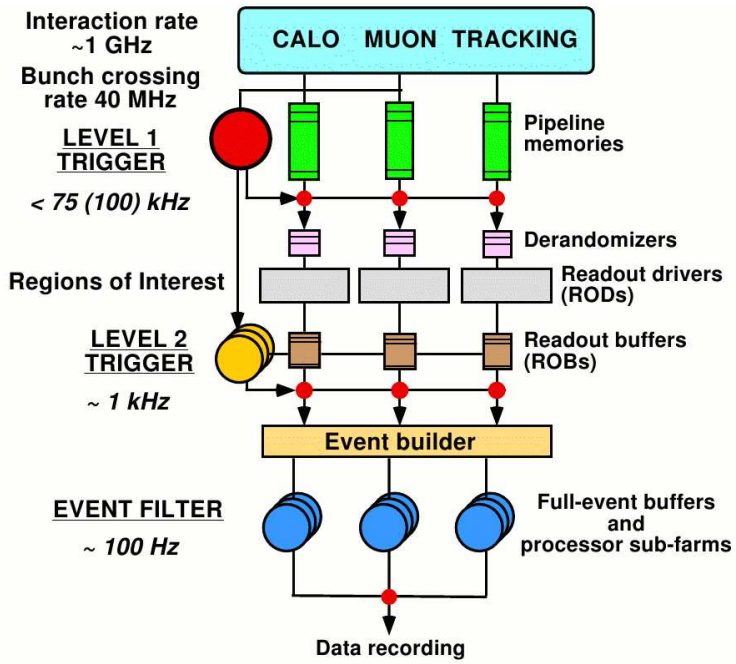

Figure 5.5: Block diagram of the ATLAS Trigger/DAQ system [35]. Calorimeter and muon responses induce a LVL1 trigger decision and supply regions of interest. The total data is held in buffers until the HLT requests it. As a first stage of the HLT, the LVL2 trigger runs on the detector data from the Regions of Interest. The EF then processes the complete event data assembled by the Event Builder or a selected subset [35].

To achieve the necessary rejection while maintaining a high efficiency for the physics processes of interest, ATLAS features a three-level trigger system (figure 5.5) [31]:

- The first-level trigger (LVL1) (section 5.2.2) is implemented in hardware and is sensitive to jets, electromagnetically interacting particles, and muons [36];
- the level 2 trigger (LVL2) and the
- event filter (EF) make up the software high-level trigger (HLT) (section 5.2.3), running consecutively on an online computer farm [35].

The further an event progresses through this chain, the more completely the event is taken into account: LVL1 accepts events based on coincidences of the hardware trigger, LVL2 runs fast algorithms on partial detector data (from regions of interest (RoIs), section 5.2.2), and the EF can processes the complete event data (if necessary), using algorithms similar to those used for offline analyses. The trigger system rejects a majority of the incoming events at each stage in order to refine the ultimate event selection, which is then recorded [35].
Therefore, the event data must be held in pipeline memories until the HLT requests it (based upon the LVL1 decision), requiring the data acquisition (DAQ) system to be able to handle about 160 GBytes/s of compressed data coming from the read-out links [35].

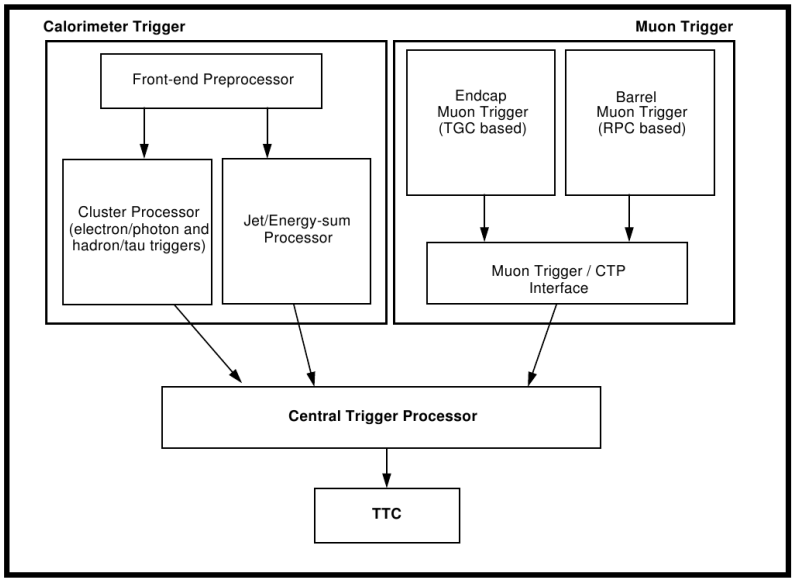

Figure 5.6: Block diagram of the LVL1 trigger system [36]. Calorimeter trigger and muon trigger data is processed by the central trigger processor. The LVL1 decision induced is then passed on to the timing, trigger, and control (TTC) system.

In order not to exceed the maximum buffer depths, the LVL1 trigger needs to take less than 2.5 μs between the corresponding bunch crossing and the LVL1 accept signal. LVL2 algorithms are required to execute in about 1-10 ms, depending on the event considered [30]. For EF algorithms, up to 1 s of computing time is acceptable.

5.2.1 Trigger Bandwidths

The LVL1 trigger can be operated at output rates up to about 100 kHz [35]. The bandwidth of each trigger level is limited by the computing power offered by the HLT and the available data recording rate, the former depending on the available hardware and its price development. Also, the algorithms running on the HLT (with their respective required computing times) and the demands on the trigger menu are still subject to change, complicating predictions of trigger bandwidths.

The LVL2 trigger is therefore designed to deal with a LVL1 output rate of 100 kHz, which is above the ATLAS baseline of 75 kHz [35]. 75 kHz is cited as the maximum readout rate the initial system can handle [37]. The HLT computing in the initial setup will be able to deal with a LVL1 output rate of approximately 40 kHz, which is about half of what is stated in the final design specifications of the HLT [37].

The event builder will be able to sustain an event-building rate of about 2 kHz, and the achievable EF output bandwidth will be a sustained event rate of 200 Hz from the beginning of data taking if the performance criteria regarding computing times and efficiencies are met by the HLT algorithms [37].

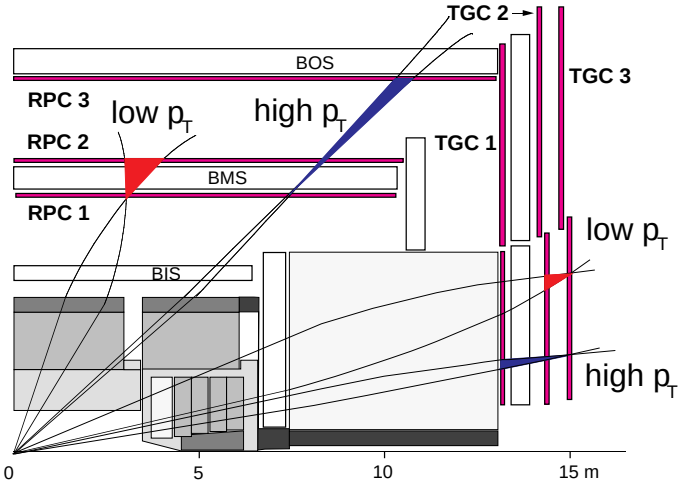

Figure 5.7: The ATLAS muon trigger system (1/4 section through one of the toroid coils) [34]. In these sectors, small barrel stations (BIS, BMS, and BOS) are used because of the toroid coils. The sketch illustrates the trigger logic for the barrel and end-cap regions.

5.2.2 First-Level Trigger

The LVL1 trigger (figure 5.6) consists of the muon and calorimeter triggers, the various results of which induce a LVL1 trigger decision from the Central Trigger Processor, which can store up to 96 menu items. These trigger items can be combined signatures and may be subjected to prescaling, i.e., considering only a fraction of the events fulfilling a trigger condition [36].

Muon Trigger System

Apart from the precision chambers of the muon spectrometer (section 5.1.3), the ATLAS detector features fast muon chambers for triggering (figures 5.4 and 5.7), bunch crossing identification, and measurements of the polar angle ϕ of hits [30].
The muon trigger system covers the pseudorapidity range $|\eta| < 2.4$. In each barrel trigger station, two orthogonal layers of resistive plate chambers (RPCs) are used, thin gap chambers (TGCs) are used in the end-cap trigger stations. The RPCs have a space-time resolution of about $1\,\text{cm} \times 1\,\text{ns}$ [30], and the TGCs also resolve to below 25 ns with 99% efficiency, enabling the use of the muon trigger for bunch crossing identification [34].
The six transverse momentum (p_T) thresholds of the muon trigger system (three for muons with low transverse momenta p_T and three for high-p_T muons) are stored in lookup tables and can be adjusted to control passing rates and acceptances [36]. These thresholds will be exclusive, i.e., fulfillment of one signature does not mean the passing of all signatures corresponding to lower p_T values.
The trigger logic (depicted in figure 5.7) is based on coincidence matrices: A hit of the middle station (called pivot station) induces a check for hits in the inner or outer station of the barrel and end-cap regions, respectively. It is tested if a hit

occurred within the defined neighborhood around a straight line extrapolation from interaction point to pivot station hit (defining a "road") in this second station. In this case, the event passes the LVL1 muon trigger, unless the second hit occurred in the central part of the road corresponding to muon tracks exceeding the lowest high transverse momentum threshold. For high-p_T muons, a hit close to the road in the outer or inner station is required for trigger passes in the barrel and end-cap regions, respectively, to enhance momentum discrimination [38].
Positive trigger decisions of the LVL1 muon trigger are verified by the HLT ("muon confirmation"), which additionally uses data from the precision muon chambers and from the inner detector [30].

Calorimeter System

The ATLAS calorimeter trigger system uses the calorimeter data in two ways:

- The cluster processor uses the full calorimeter granularity for electron/photon and hadron/tau triggers, and
- the jet/energy-sum processor merges energy deposits from adjacent hits in the electromagnetic calorimeter to so-called trigger towers, whose granularity and angular coordinates match those of the elements of the hadronic calorimeters: $(\Delta\eta \times \Delta\phi) = (0.1 \times 0.1)$ for $|\eta| < 2.5$. The trigger towers become coarser for larger values of $|\eta|$. This information is used for triggering on high transverse energy (E_T), missing transverse energy, and total scalar-E_T [36].

The jet trigger information also contains the polar and azimuthal coordinates of the center of the energy deposit. From this information, an RoI is built to allow the use of partial detector data by the LVL2 trigger.

5.2.3 High-Level Trigger

The HLT is to further refine the event selection commenced by LVL1. It runs on an online computer farm at the SDX1 building above the ATLAS pit, where it receives the RoI information and readout data from the computers in cavern USA15, adjacent to the ATLAS pit [39]. The HLT nodes are placed in racks, each containing 31 dual-CPU nodes [37].
Of the thirty-six computer racks of the initial HLT setup, eight racks are reserved for EF running. The other twenty-eight racks can be assigned either to run LVL2 or EF algorithms, depending on the trigger menu and the experimental conditions [37].
The algorithms running on LVL2 (using data from the RoIs provided by LVL1) and on EF (with access to the full event data) are developed bearing in mind the input requirements of the offline analyses of the various channels at ATLAS. Their performance greatly impacts their integration into the trigger menu, keeping in mind the limitations of the maximum HLT latencies and passing rates (chapter 11).
The evolution of the HLT computing power depends on the overall budget and on the development of hardware costs. It is also limited by the total available space in the computer racks.

Part III

Monte Carlo Production, Reconstruction, and Data Analysis

Chapter 6

Monte Carlo Production

In order to prepare the analysis of data from the ATLAS detector, the ATLAS computing framework Athena [40] is used to simulate the response of the ATLAS detector to physics processes. The physics processes are provided by the Monte Carlo (MC) generation software Pythia [41].
The datasets used within this thesis originate from production for the ATLAS computing system commissioning (CSC) effort (section 6.2) and from local production [42].

6.1 Procedure

The production of MC data input for an Athena-based physics analysis is performed in several separate steps. This allows validating each part of the production process. As each step is very demanding in terms of computing power, this step-wise approach also carries the advantage of saving resources, e.g., during validation efforts.

6.1.1 Generation

The Pythia event generator is used to simulate the interactions following pp collisions at 14 TeV center-of-mass energy. For the generation of the datasets used within this thesis, the default parton density function `CTEQ6L1` [43] of Pythia release 6.403 has been used, employing an underlying event tuning for extrapolation from TEVATRON to LHC center-of-mass energies [15].
For a validation of the consecutive MC production steps as well as of the reconstruction and the offline analysis, the intermediate and final state particles generated by Pythia and their properties are stored and included in the output files of all consecutive production steps (MC truth).
Pythia simulates a hard scattering process of partons inside the protons after the simulation of initial state radiation. Cuts on the resulting states can be applied (`ckin` values) to improve the generation efficiency. `ckin 3` constitutes a lower bound (given in GeV) of the transverse momentum of the hard $2 \rightarrow 2$ scattering process [41]. A `ckin 3` value of 6 GeV is used as reference value.

After considering final state radiation as well as multi-particle interactions, a hadronization process is simulated for the resulting quark and gluon states. Consequently, PYTHIA simulates the decay of unstable particles.
For a more efficient and controlled production of events containing B mesons, the PythiaB interface [44] to PYTHIA is used. It allows a rejection of generated events, which do not contain the specified signal decay, already after the `ckin` cuts have been applied. In addition, PythiaB allows setting selection cuts on quark pairs. These settings influence both the cross-sections calculated by PYTHIA and the kinematic distributions of the generated particles. PythiaB has been used for the generation of all signal and background datasets used in this thesis. Selection cuts for the generated quark states are set by the `cutbq` variable.
Only a quark or an antiquark of the specified flavor (b for all but the charm background sample) has to pass the given selection cuts per event for the background samples.
For the signal samples, both a b quark and a $\bar{b}$ quark have to pass the selection cuts:

$$p_T(b,\bar{b}) > 6\,\text{GeV}\ (\text{“}\texttt{BsDsA1mu6}\text{”}) \quad \text{and} \quad p_T(b,\bar{b}) > 4\,\text{GeV}\ (\text{“}\texttt{BsDsA1mu4}\text{”}), \tag{6.1}$$

$$\left|\eta(b,\bar{b})\right| < 2.5 \text{ for } \texttt{BsDsA1mu6} \text{ and } \texttt{BsDsA1mu4}, \tag{6.2}$$

$$\left|\eta(b,\bar{b})\right| < 4.5 \text{ for } \texttt{bbmu6X}, \texttt{bbmu4X}, \text{ and } \texttt{ccmu4X}. \tag{6.3}$$

The labels “`mu6`” and “`mu4`” refer to cuts requiring a muon above the p_T threshold and within the approximate rapidity acceptance of the muon spectrometer:

$$p_T(\mu) > 6\,\text{GeV} \text{ for } \texttt{mu6} \text{ datasets} \quad \text{and} \quad p_T(\mu) > 4\,\text{GeV} \text{ for } \texttt{mu4} \text{ datasets}, \tag{6.4}$$

$$|\eta(\mu)| < 2.5 \text{ for all datasets.} \tag{6.5}$$

Otherwise, the generated event is discarded.
For the signal datasets, also cuts on the kaons and pions within the event are set:

$$|\eta(K,\pi)| < 2.5, \tag{6.6}$$

$$p_T(K,\pi) > 0.5\,\text{GeV}. \tag{6.7}$$

The cross-sections obtained for the generated events are given by PYTHIA and may be used for cross-section estimates. By evaluating the output of multiple generation jobs, the statistical errors of these estimates is assessed. Leading order and next-to-leading order cross-section values for the production of b quark pairs at 14 TeV center-of-mass energy are attached to a systematic uncertainty. It is estimated to be a factor of 2 in either direction [16].

6.1.2 Detector Simulation

The final state particles generated by PYTHIA are propagated through the detector, using the Geant4 detector simulation software [45]. This step uses a detailed detector

description to simulate the interaction of the final state particles with the electromagnetic fields and matter within the detector. The `ATLAS-CSC-01-02-00` detector description [46] has been used for the simulation of all datasets. This detector description uses a complex magnetic field map and a misaligned detector geometry. It also introduces additional material into the detector description for an evaluation of how the detector performances of the inner detector and the calorimeter depend on the amount of material introduced. For comparison, the additional material is only introduced in the upper detector hemisphere, corresponding to $\phi > 0$.

6.1.3 Hit Digitization

From the results of the detector simulation, the detector response is determined during the hit digitization step. The resulting hit maps are stored into raw data object files, which represent a realistic simulation of the data provided by the detector electronics.

6.1.4 Reconstruction

The event reconstruction prepares the hit digitization data for the offline analysis. In the case of MC data, it simulates the reaction of the detector electronics, such as the trigger system, to the hits. Consequently, the event reconstruction applies algorithms for combining detector hits to tracks, calorimeter clusters, etc. The resulting analysis object data (AOD) no longer contains hits, reducing the amount of data stored per event.
Data from the ATLAS detector will be subjected to the same reconstruction procedure, as far as the steps after the data processing after the trigger decision are concerned. The detector data will also be saved in the AOD format. This data format constitutes the input for the offline analysis [12] used within this thesis.
The trigger simulation uses the trigger configuration `CSC-06-900GeV` [47] to simulate the trigger output based on the trigger menu foreseen [48] for the initial luminosity $\mathcal{L} = 10^{31}\,\mathrm{cm}^{-2}\mathrm{s}^{-1}$ provided by the LHC. Each high-level trigger (HLT) level runs feature extraction (FEX) algorithms, which provide input for trigger hypothesis algorithms, that determine the trigger decision for their respective trigger signatures. The B-physics trigger uses hit data from the inner detector in order to reconstruct particle candidates. For the given datasets, the track reconstruction efficiency for tracks from the end-caps of the inner detector is reduced by about 10 to 15 % [49] due to a bug[1] in Athena release 12, which was used for reconstruction. The HLT simulation for the datasets used lacks two features relevant to the trigger studies:

- The simulation of the HLT muon confirmation (section 5.2.2) is not operational in Athena release 12. Therefore, the results given as LVL2 efficiencies within this thesis only refer to the $D_s^{\mp}$ trigger. Events will only be considered by the event filter (EF) $D_s^{\mp}$ signature if the appropriate LVL2 muon signature is fulfilled.

[1] solved in recent releases [49]

- The EF $D_s^{\mp}$ trigger decision is not available for the given datasets.

Therefore, neither the HLT muon confirmation nor the EF $D_s^{\mp}$ results are covered by this thesis despite their relevance for the overall trigger efficiency.

6.1.5 LVL2 Trigger CPU Time Measurements

In order to obtain information on the computing time required by the LVL2 $D_s^{\mp}$ trigger signature, reconstruction must be run in a mode that avoids interference by other algorithms. This is achieved by creating a byte stream file from raw data objects files and running a reconstruction job that only simulates the HLT algorithms necessary for the trigger element examined (section 7.2.3).

6.2 Datasets

For this thesis, datasets from two sources have been used:

- The computing grid installed to provide the computing resources for MC production and data analysis for the LHC experiments ("Grid") is a very complex and powerful computing system. It is used for MC production and offline analysis as a proof of concept within the ATLAS computing system commissioning (CSC) effort.

- The batch queue system of a computer cluster[2] running a 32 bit linux system was used. The Athena installation is uniform for the cluster nodes and therefore constitutes a reliable computing resource for MC production and offline analysis.

As the context of this thesis is given by contributing trigger studies to the CSC effort [13], CSC datasets produced on the Grid were used wherever possible. For the analysis of background processes contributing to trigger rates, three CSC datasets were employed:

- The `bbmu6X` dataset contains $b\bar{b} \rightarrow \mu 6X$ processes.

- The `bbmu4X` sample provides $b\bar{b} \rightarrow \mu 4X$ processes.

- The `ccmu4X` data sample consists of events from $c\bar{c} \rightarrow \mu 4X$ processes.

The signal datasets were produced on `SiMPLE`:

- The `BsDsA1mu6` dataset contains $B_s^0 \rightarrow D_s^- a_1^+(\mu 6)$ processes.

- The `BsDsA1mu4` sample consists of $B_s^0 \rightarrow D_s^- a_1^+(\mu 4)$ events.

[2]Siegen multi-processor linux environment (SiMPLE) of the particle physics group at the University of Siegen

The most important properties of the datasets used are summarized in table A.1.
The `BsDsA1mu4` dataset was produced on `SiMPLE`, as the datasets of the CSC effort did not include $B_s^0 \rightarrow D_s^- a_1^+(\mu 4)$ events without muons with a p_T of more than 6 GeV.
The `BsDsA1mu6` data sample was used instead of the corresponding Grid dataset in order to perform a separate study of LVL2 particle candidates originating from a full scan or from a region of interest. This cannot be done using the CSC datasets. However, the `BsDsA1mu6` sample has been validated against the Grid dataset in terms of the quantities relevant to the offline analysis [13, 14] and the trigger simulation.

Chapter 7

$B_s^0 \to D_s^- a_1^+$ Offline Analysis and Trigger Studies

The $B_s^0 \to D_s^- a_1^+$ analysis has been implemented by T. Stahl [12]. It uses analysis object data (AOD) to probe events for $B_s^0 \to D_s^- a_1^+$ decays and the charge conjugated decay. The signal samples do not contain $\bar{B}_s^0$ decays. In the following chapters, $B_s^0 \to D_s^- a_1^+$ refers to both the decay denoted and the charge conjugated decay unless otherwise stated. Since the results from the MC trigger simulation are also included in the AOD, the $B_s^0 \to D_s^- a_1^+$ analysis constitutes a good platform for trigger studies: Both simulated physics and trigger data are available, allowing an analysis of the various correlations.

7.1 Offline Analysis Steps and Cuts

In order to search for $B_s^0 \to D_s^- a_1^+$ event signatures, the $B_s^0 \to D_s^- a_1^+$ analysis code [12] uses reconstructed tracks from AOD, fits vertices, and applies cuts. The analysis performs the following steps:

1. Information from tracking, vertexing, and a muon reconstruction algorithm is retrieved. In the case of MC generated data, also truth information is retrieved for evaluation and validation purposes.

2. Jet region of interest (RoI) multiplicities and decision information for various trigger signatures are read out [50] from the trigger simulation results (section 7.2).

3. Information about the reconstructed primary vertex is retrieved.

4. In case MC truth processing is enabled, the analysis code searches the truth data for the particles from the decay chain and their tracks, the true primary vertex, and the muon with the highest transverse momentum, which is assumed to be the tagging muon. In 44276 out of 50000 events from the `BsDsA1mu6` dataset ($(88.55 \pm 0.14)\,\%$), the charge of the muon with the highest true transverse momentum matches the initial flavor of the B_s^0 meson, supporting this assumption.

5. The analysis code retrieves the data from the second-level (LVL2) B-physics trigger [50]. This includes particle candidates and results from fast vertex fits. In addition, the information from which RoI the candidate tracks for the D_s^- and ϕ particles originate is obtained (only possible for the `BsDsA1mu6` dataset).

6. A similar set of information is retrieved for the event filter (EF) $D_s^{\mp}$ trigger signature [50], which is not subject of these studies because of configuration problems of the high-level trigger (HLT) simulation (section 6.1.4).

7. The initial flavor is determined by the `BFlavourTagger` algorithm by using the reconstructed muon information of the muon with the highest p_T in the event. The algorithm shall be extended to also consider additional muons if applicable. The result of the `BFlavourTagger` tagging algorithm is read out for an evaluation of the mistag fraction, i.e., the fraction of the events assigned the wrong initial flavor. By comparing the tagging result to MC truth information, the performance of the `BFlavourTagger` algorithm can be probed.

8. Cuts on the reconstructed tracks are performed:

   - Events with less than three positive or less than three negative tracks are rejected, as the signal contains six final state particles with charges of $\pm e$, adding up to a total charge of zero.
   - Only tracks with a pseudorapidity:

     $$|\eta(\text{tracks})| < 2.5, \tag{7.1}$$

     which is the range covered by the inner detector, are used for event reconstruction.

9. The algorithm searches for ϕ candidates, using reconstructed tracks with a transverse momentum:

   $$p_T > 1.5\,\text{GeV} \tag{7.2}$$

   as kaon candidates. Only track pairs with opposite charges and with projected opening angles in ϕ and θ:

   $$\left|\Delta\phi(K^+, K^-)\right| < 10\,^\circ, \tag{7.3}$$
   $$\left|\Delta\theta(K^+, K^-)\right| < 10\,^\circ \tag{7.4}$$

   between the reconstructed direction vectors at the interaction point are considered.

10. A vertex fit is performed for each passing track pair with an invariant mass $m(K^+K^-)$ passing a loose mass window cut centered on the ϕ mass:

    $$0.869413\,\text{GeV} < m(K^+K^-) < 1.169413\,\text{GeV}. \tag{7.5}$$

Thus, the number of vertex fits which are likely to fail or yield bad candidates is reduced.

A cut on the invariant mass obtained from each successful vertex fit:

$$1.007833\,\mathrm{GeV} < m(\phi) < 1.030993\,\mathrm{GeV} \tag{7.6}$$

is applied. The mass window corresponds to ranges of 2σ (obtained from a Gaussian fit) left and right of the ϕ meson mass (2σ cut). Consequently, a cut on the χ^2 of the vertex fit is performed:

$$\chi^2(K^+K^-) < 7. \tag{7.7}$$

The χ^2 cut is to eliminate vertex candidates with less than 1% probability for a common vertex (fit probability).

11. In order to form $D_s^\mp$ candidates, the passing ϕ candidates are then combined with tracks fulfilling:

$$p_T(\pi^\mp_{D_s^\mp}) > 1.5\,\mathrm{GeV}, \tag{7.8}$$

assuming the track to originate from a pion. After a loose mass cut around the $D_s^\mp$ mass:

$$1.8185\,\mathrm{GeV} < m(K^+K^-\pi^\mp) < 2.1185\,\mathrm{GeV}, \tag{7.9}$$

a vertex fit is performed, cutting on:

$$\chi^2(D_s^\mp) < 12 \qquad (1\%\text{ fit probability}) \tag{7.10}$$

and rejecting all candidates from the vertex fit outside the set $D_s^\mp$ mass range, which is again obtained from a Gaussian fit:

$$1.9215\,\mathrm{GeV} < m(D_s^\mp) < 2.0155\,\mathrm{GeV} \qquad (2\sigma\text{ mass range}). \tag{7.11}$$

12. Analog to the process of probing ϕ candidates, ρ candidates are formed from track pairs of opposite charge (pion hypothesis) fulfilling:

$$\measuredangle(\pi^+,\pi^-) < 0.650, \tag{7.12}$$

with the opening angle:

$$\measuredangle(\pi^+,\pi^-) = \sqrt{(\Delta\phi(\pi^\pm))^2 + (\Delta\eta(\pi^\pm))^2}.$$

The cut is chosen in order to achieve an efficiency of 95% for true ρ candidates.

A vertex fit is performed for each ρ candidate passing a loose mass cut centered on the ρ mass (applied on the mass value obtained using track fits):

$$375.8\,\mathrm{MeV} < m(\pi^+\pi^-) < 1175.8\,\mathrm{MeV} \tag{7.13}$$

is done. After a χ^2 cut:

$$\chi^2(\pi^+\pi^-) < 7 \qquad (1\% \text{ fit probability}), \tag{7.14}$$

the same mass cut is applied on the result from the vertex fit:

$$375.8\,\text{MeV} < m(\rho) < 1175.8\,\text{MeV}. \tag{7.15}$$

13. Analog to the D_s^- candidate search, sets of one additional track and the ρ candidate track pairs are used to evaluate a_1^+ candidates from track triplets:

$$\chi^2(\pi^+\pi^-\pi^+) < 12\ (1\% \text{ fit probability}), \tag{7.16}$$
$$0.730\,\text{GeV} < m(\pi^+\pi^-\pi^+) < 1.730\,\text{GeV}, \tag{7.17}$$
$$0.730\,\text{GeV} < m(a_1^+) < 1.730\,\text{GeV}. \tag{7.18}$$

Additionally, a cut on the opening angle of the reconstructed momentum of the ρ candidate and the track:

$$\measuredangle(\rho, \pi^-) < 0.585 \tag{7.19}$$

is performed, tuned to achieve an efficiency of 95% among true $a_1^\pm$ candidates.

14. As combining three charged pions produces double $a_1^\pm$ candidates, additional candidates originating from the same triplet are discarded.

15. When combining $D_s^\pm$ and $a_1^\mp$ candidates of opposite charge, the combination is checked for tracks that were used both for forming the $D_s^\pm$ candidate and the $a_1^\mp$ candidate. Such combinations are discarded. A loose mass cut around the B_s^0 mass:

$$5.1193\,\text{GeV} < m(2K\,4\pi) < 5.6193\,\text{GeV} \tag{7.20}$$

is applied to the resulting track sextuplets.

16. The passing sextuplets are then subjected to a vertex fit. A χ^2 cut is applied:

$$\chi^2(B_s^0) < 27 \qquad (1\% \text{ fit probability}). \tag{7.21}$$

17. A cut on the proper time of the B_s^0 candidates is applied, in order to improve background rejection:

$$t(B_s^0) > 0.4\,\text{ps}. \tag{7.22}$$

A loose cut on the three-dimensional impact parameter (b) of the decay vertex of the B_s^0 candidates and the reconstructed primary vertex is performed:

$$b(B_s^0) < 55\,\mu\text{m}. \tag{7.23}$$

A cut:

$$d_{xy}(B_s^0) > 0 \tag{7.24}$$

on the transverse decay length (d_{xy}) of the B_s^0 candidates is applied for background rejection. The sign of d_{xy} is positive if the reconstructed transverse momentum of the B_s^0 candidate and the vector from the reconstructed primary vertex to the decay vertex point into the same direction.

As the spacial resolution of the proper time resolution for the B_s^0 candidates is proportional to the transverse momentum, a cut:

$$p_T(B_s^0) > 10\,\text{GeV} \tag{7.25}$$

is performed.

18. A cut on the invariant mass of the B_s^0 (obtained from the vertex fit) is applied:

$$5.2693\,\text{GeV} < m(B_s^0) < 5.4693\,\text{GeV}. \tag{7.26}$$

19. Per event, only the B_s^0 with the best vertex fit result (minimal χ^2) is stored. It will be used for the mixing analysis, which is performed using the amplitude fit method and currently uses random-generated input [12].

The subset of events from a dataset that pass these selection cuts is labelled "selection cut passes" in this thesis. The share of the selection cut passes for each dataset used is given in the dataset summary (table A.1).
Depending on the analysis job options, the remaining steps are skipped for the event if one of the above steps fails. Especially, the analysis can be set to ignore events failing given trigger conditions or failing to meet constraints on the track fit mass calculated for the D_s^- and ϕ candidates by the LVL2 B-trigger (section 9.3).
The reconstructed and true (if available) kinematic variables, trigger decisions, etc. are stored into N-tuples. They can be used for further analysis using the ROOT data analysis framework [51].

7.2 Trigger-Aware Analysis

The trigger studies are performed in two steps:

1. During the $B_s^0 \to D_s^- a_1^+$ analysis, trigger information is read from AOD and can be used to impose a trigger condition on a dataset: By setting a job option, the analysis job can be set to test whether the events fulfill a certain trigger condition. The other events are flagged as failing the trigger selection and further decay reconstruction is skipped.

2. By comparing N-tuples with different sets of trigger requirements from the same dataset, trigger efficiencies can be obtained and their dependence on event characteristics, such as the transverse momenta of the particles from the decay, can be examined.

7.2.1 Trigger Decision

The trigger simulation of Athena release 12 creates within the AOD a `TriggerDecision` object, which contains the information which trigger conditions were fulfilled. The `TriggerDecision` object is retrieved, it is checked whether a signature is defined for the run, and it is requested whether or not the trigger signature is fulfilled for an event. The signatures are identified by character strings, which by convention begin with `L1_` for the LVL1 trigger signatures and `L2_` or `EF_` for HLT signatures. For the different datasets, the following trigger conditions are evaluated:

1. No trigger requirement, i.e., all events are considered. Trigger efficiencies given in this thesis always refer to this entity.

2. Events passing the `L1_BJT15` signature of the LVL1 trigger: This signature is to indicate an energy deposition of 4 GeV or more within a jet RoI of 4×4 trigger towers (in the coordinates $\eta \times \phi$). It is used for seeding (i.e., initiating the execution) of the LVL2 RoI-based B-trigger. A discussion of the choice of threshold is given in section 11.3. The resulting condition is abbreviated by `JT0X` within this thesis, `X` being the threshold in GeV. The number `15` in the `L1_BJT15` signature name refers to the jet energy value in GeV above which the trigger efficiency is approximately constant. The threshold energy describes the trigger condition better, which is why the `JT0X` notation is used within this thesis.

3. Events passing the LVL1 single-muon trigger: This trigger condition may be adjusted to match events passing any exclusive muon signature with a p_T threshold equal to or higher than a given value. The resulting inclusive condition is abbreviated by `MU0X+` within this thesis, `X` being the threshold in GeV. It may be combined with any of the LVL2 conditions. The logical 'and' operator is denoted by `&&`. The thresholds in the trigger simulation of the given datasets are set from the `CSC-06-900GeV` trigger menu [47]. This trigger menu offers a low-p_T muon trigger menu including one open window threshold `L1_MU00` (`MU00+` for the inclusive signature), which requires a coincidence between two low-p_T trigger stations (section 5.2.2). The open window corresponds to a p_T threshold of about 4 GeV, which is dependent on the detector region and the muon charge sign because of the small curvature radius of low-p_T muons. The `CSC-06-900GeV` low-p_T muon trigger menu is completed by thresholds of 5 and 6 GeV (`L1_MU05`, `L1_MU06`). The high-p_T muon trigger menu contains thresholds of 11, 20 and 40 GeV.

4. Events passing the LVL2 $D_s^{\pm}$ RoI trigger [50]: The `L2_BsDsPhiPi` trigger signature is seeded by `JT04` and searches for $D_s^{\pm}$ candidates from reconstructed tracks from the given jet RoI. This is done by combining track pairs of opposite charge to form ϕ candidates, which are then combined with another track each to form $D_s^{\pm}$ candidates. The trigger decision is based on mass cuts on the candidate track combinations, which are assigned invariant masses by applying mass hypotheses on the reconstructed momenta. Fast vertex fits are

performed for the ϕ and $D_s^{\pm}$ candidates, but information from the vertex fits is not used for the trigger decision so far.

5. Events passing the LVL2 $D_s^{\pm}$ full scan (FS) trigger [50]: The `L2_BsDsPhiPi-FullSCan` trigger signature is seeded by the LVL1 muon trigger (`MU00+` in `CSC-06-900GeV`). It performs the same steps as the `L2_BsDsPhiPi` trigger item, but using tracking information from the full inner detector.

7.2.2 Invariant Masses from LVL2 Track Fits

For an evalution of the LVL2 $D_s^{\pm}$ trigger performance, tracking and vertex data reconstructed by the LVL2 trigger is stored in the AOD using `TrigL2Bphys` objects. For offline studies of the LVL2 trigger mass resolution, the particle candidates are retrieved, and it is checked which particle from a given set of particle hypotheses the B-physics trigger judged the candidate to be. Via the `TrigL2Bphys` objects, the reconstructed invariant masses calculated from `IDSCAN` track fits and a set of final state particle mass hypotheses can be obtained. From a fast vertex fit using these tracks, the χ^2 and the number of degrees of freedom of the vertex fit are available. The information within the `TrigL2Bphys` objects allows an evaluation of the mass cuts performed by the trigger. From the datasets used (appendix A.1), only the `BsDsA1mu6` dataset (locally produced) contains RoI identification information which can be associated with the particle candidates (section 9.3).
A study of how the mass resolution changes with the true pseudorapidity of the B_s^0 meson is described in section 9.3. This section also explains how changing the LVL2 cut on the invariant mass of the $D_s^{\pm}$ candidates from the asymmetric range around the $D_s^{\pm}$ mass, which is set in Athena release 12, to a symmetric range affects the trigger efficiency. This is done by extending the $B_s^0 \to D_s^- a_1^+$ analysis by an option to reject events without trigger particle candidates ($D_s^{\pm}$ and ϕ) inside given mass ranges.

7.2.3 Measurement of High-Level Trigger Computing Time

The evaluation of the timing requirements of the LVL2 $D_s^{\pm}$ trigger is performed in three steps for the RoI-based trigger:

1. For an evaluation of the RoI multiplicity for background events, `L1JetObject` information is extracted from AOD [50].

2. In order to estimate the event rate for the contributing background channels, cross-sections obtained from PythiaB studies (section 6.1.1) are used. The product of RoI multiplicity and background event rate yields the rate at which the HLT processes RoIs (seeding rate).

3. The computing time requirements of the two implementations of the LVL2 $D_s^{\pm}$ trigger have been measured with 2000 $b\bar{b} \to \mu 6X$ events on a dedicated 3 GHz

CPU[1]. The timing jobs use analysis data in the byte stream format, which simulates data flow from the detector. The reconstruction job only executes the LVL2 algorithm in question and records timing data, avoiding system load by other algorithms.

For the FS implementation, the HLT computing time requirement is obtained from the expected LVL1 muon trigger rate and the FS processing time per event obtained from a separate run over the same 2000 events, executing only the algorithms on which the FS trigger signature depends.
Multiplying the seeding rate and the average LVL2 computing time ($t_{\mathrm{FS,RoI}}$) gives the number of parallel LVL2 processing units occupied by each trigger strategy. As track reconstruction is the main contribution to the HLT computing time, the computing time required by the RoI-based algorithm is shorter than for a full scan of the inner detector (section 11.1). For this reason, the FS algorithm is envisaged to be used for initially low background event rates only. As the luminosity provided by the accelerator is increased, the RoI trigger implementation shall be used in order to use as little HLT computing time as possible while avoiding to introduce prescaling, i.e., considering only a fraction of the events fulfilling a trigger condition.

7.3 Computation of Trigger Efficiencies

7.3.1 Definition of the Problem

For a trigger element, the distribution of a quantity (e.g., the p_T of one of the particles from the $B_s^0 \to D_s^- a_1^+$ decay chain) is given as a histogram for all events to which the trigger element is applied (entries N_i) and another histogram for all events which are accepted by the trigger element (entries k_i).
From this information, the trigger efficiency for each bin shall be concluded and assigned an confidence interval.

7.3.2 Solution using the ROOT `TGraphAsymmErrors` Class

Both the problem and the solution are described in [52]. Several commonly used error assessment strategies prove to be inapt for trigger studies:

- Poissonian errors: This method will assign different errors to a statistical event (N_i, k_i) and its complement $(N_i, N_i - k_i)$. Especially, measured efficiencies of zero, i.e., $k_i = 0 < N_i$, will be assigned an error value of zero.

- Binomial errors: This method solves the asymmetry issue of the Poissonian error assignment, but underestimates the errors for high ($k_i \approx N_i$) and low ($k_i \approx 0 < N_i$) trigger efficiencies.

These problems can be avoided by the following ansatz [52]:

[1] Intel Pentium 4

A flat a priori probability distribution $P(\epsilon_i; N_i)$ of the efficiency from zero to one is assumed. This assumption allows a reversal of the assertion given by the measurement using the Bayesian theorem:

$$P(\epsilon_i; k_i, N_i) = \frac{1}{C} P(k_i; \epsilon_i, N_i) P(\epsilon_i; N_i). \tag{7.27}$$

In this equation, $P(\epsilon_i; k_i, N_i)$ is the probability density function of ϵ_i for given values of k_i and N_i in bin i. This distribution is to be described by the efficiency value ϵ_i cited and the error value assigned to it. C is determined from the normalization of the distribution. The probability $P(k_i; \epsilon_i, N_i)$ for a certain number of passes k_i resulting from the true efficiency ϵ_i and a known number of total events in the bin N_i can be calculated from the binomial distribution:

$$P(k_i; \epsilon_i, N_i) = \binom{N_i}{k_i} \epsilon_i^{k_i} (1 - \epsilon_i)^{N_i - k_i}. \tag{7.28}$$

Using the beta function for calculating the normalization, this leads to:

$$P(\epsilon_i; k_i, N_i) = \frac{(N_i + 1)!}{k_i!(N_i - k_i)!} \epsilon_i^{k_i} (1 - \epsilon_i)^{N_i - k_i}. \tag{7.29}$$

For $k_i \neq \frac{N_i}{2}$, $P(\epsilon_i; k_i, N_i)$ is asymmetric, and the mean and the mode of the distribution are not equal:

$$\begin{aligned} \text{mean}(\epsilon_i) &= \frac{k_i + 1}{N_i + 2}, \\ \text{mode}(\epsilon_i) &= \frac{k_i}{N_i}. \end{aligned}$$

The asymmetry of $P(\epsilon_i; k_i, N_i)$ is small for combinations of:

$$\text{large values of } N_i \tag{7.30}$$

and:

$$|\text{mode}(\epsilon_i) - 0.5| < 0.5, \tag{7.31}$$

i.e., efficiencies significantly different from 0 and 1. For this case, [52] recommends the citation of the mean for the measured value and the square root of the variance as measurement error for an analytical approximation.
For trigger studies, the assertions (7.30) and (7.31) fail in several cases:

1. Bins of the histograms for all events, which contain a small number of entries, may result in significantly asymmetric probability density functions.

2. The means of the asymmetric probability density functions are biased towards efficiency values near 0.5. For efficient background rejection or signal acceptance, this poses a problem, as the bias is larger for these cases.

In case the above method is likely to give biased results, the ROOT framework offers a `TGraphAsymmErrors` constructor, which takes two pointers to histograms as arguments: The first histogram contains the distribution for the events passing the trigger, and the second histogram contains the distribution for all events. It evaluates the efficiency values and errors in the following way: The mode of ϵ_i is used for estimating efficiency values. This carries the advantage of imposing no bias. For assigning error values, the shortest error range is chosen in such a way that the integral over the error range is equal to 68.3%. Up to ROOT version 5.16, this is done numerically with too little precision for finding reliable error values for bins with larger numbers of entries. This was fixed by patching the source code to increase precision [53]. ROOT version 5.16 (with the patch applied) has been used for creating the efficiency plots and all efficiency numbers stated within this thesis. In order to improve the algorithm, an approximation of the inverse beta function will be included in ROOT version 5.18 [53].

Part IV

Results of the Trigger Studies for $B_s^0 \to D_s^- a_1^+$

Chapter 8

Kinematic Distributions

Apart from its impact on the event numbers available for the offline analysis, the trigger strategy affects the kinematic distributions of the particles from the $B_s^0 \to D_s^- a_1^+$ decay chain. The reason is the dependence of trigger acceptances on quantities such as the transverse energy of the event.
Hence, analyses depending on the shape of kinematic distributions need to take the bias caused by the trigger strategy into account.

8.1 Samples without Trigger Requirement

8.1.1 $B_s^0 \to D_s^- a_1^+$ Signal Datasets

For the signal datasets `BsDsA1mu6` and `BsDsA1mu4`, the true values of the kinematic variables for the particles from the decay chain as well as for the muon with the highest p_T in the event ($\mu_{\text{highest } p_T}$) are available from the N-tuples.
The cuts applied to the signal events during generation are recapitulated in table 8.1.
The `BsDsA1mu4` dataset has been generated for trigger studies in the low-p_T regime. A looser generation cut on the p_T of one muon in the event has been applied for studying the low-p_T area (figure 8.1(b)). Other kinematic cuts also had to be loosened in order to avoid biasing the p_T distributions of the muon and the final state particles of the signal decay (section 6.1.1).
The true p_T distributions of the B_s^0 mesons (figure 8.1(a)) show "smeared" cut-offs at the p_T cut values of the b quarks. The distribution extends into the region outside the generation cut (6.1) on the p_T of the b quark because the hadronization impacts

Table 8.1: Recapitulation of the generation cuts of the signal samples.

$p_T(b, \bar{b}) > 6\,\text{GeV}$ for `BsDsA1mu6` and $p_T(b, \bar{b}) > 4\,\text{GeV}$ for `BsDsA1mu4`	(6.1)
$\left\lvert\eta(b, \bar{b})\right\rvert < 2.5$ for `BsDsA1mu6` and `BsDsA1mu4`	(6.2)
$\left\lvert\eta(b, \bar{b})\right\rvert < 4.5$ for `bbmu6X`, `bbmu4X`, and `ccmu4X`	(6.3)
$p_T(\mu) > 6\,\text{GeV}$ for `mu6` datasets and $p_T(\mu) > 4\,\text{GeV}$ for `mu4` datasets	(6.4)
$\lvert\eta(\mu)\rvert < 2.5$ for all datasets	(6.5)

the p_T of the B_s^0 mesons.
The pseudorapidity distributions of the B_s^0 mesons (figure 8.1(e)) for the `BsDsA1mu6` and `BsDsA1mu4` datasets hardly extend into the area outside the tracking coverage, as an η cut (6.6) is applied on all final state particles.
As no cuts are applied to azimuthal components of the particle momenta, the true ϕ distributions for all particles of the decay chain agree with rectangular distributions.
The proper time distributions of the B_s^0 particles within the two signal datasets agree well (figure 8.1(c)).
The D_s^- particle is to be reconstructed by the LVL2 trigger. It is a daughter particle of the B_s^0 meson. Therefore its kinematic distributions resemble those of the B_s^0 meson (figure B.1).
The cut-off of the p_T spectrum of $\mu_{\text{highest } p_T}$ (figure 8.1(b)) is more pronounced than for the B_s^0 mesons, as the p_T cut (6.4) is applied to the muon directly. Cut (6.1) on the p_T of the opposite-side b-quark can also be verified, as it does not affect the shape of the p_T distributions (figure 8.1(d)) in the vicinity of the cut-off.
Cut (6.5) on the η values of one muon per event is seen in figure 8.1(f). The muons outside (6.5) are explained by stressing that the generation cuts (6.4) and (6.5) are not necessarily applied to $\mu_{\text{highest } p_T}$ if there are additional muons within the event that pass the p_T cut.
Kinematic distributions for the six final state particles of the signal decay are shown in appendix B.1.1. The kinematic distributions of the two signal datasets are similar. The only exceptions to this are influences of cut (6.1) on the low-p_T regions, analog to what has been discussed for the B_s^0 mesons.

8.1.2 $b\bar{b} \to \mu X$ Samples

The $b\bar{b} \to \mu 6X$ and $b\bar{b} \to \mu 4X$ samples contain only background processes. Hence, from the MC truth, only the $\mu_{\text{highest } p_T}$ distributions are evaluated (figure B.7).
p_T cuts of 6 and 4 GeV, respectively, have been applied to one muon per event within the data samples, leading to similar kinematic distributions for $\mu_{\text{highest } p_T}$ as for the signal datasets. Except for the different p_T cuts, the kinematic distributions for $\mu_{\text{highest } p_T}$ for the $b\bar{b} \to \mu 6X$ and $b\bar{b} \to \mu 4X$ datasets show no significant differences.

8.2 Trigger Effects

The kinematic distributions of the B_s^0 mesons and $\mu_{\text{highest } p_T}$ are evaluated for events passing certain trigger conditions, which leads to the trigger efficiencies, when applying the method described in section 7.3.2.

8.2.1 LVL1 Muon Trigger

The change of the kinematic distributions introduced by the LVL1 muon trigger is studied for the example of the `MU06+` signature, as the other low-p_T thresholds are below the generation cut for the muons in the `BsDsA1mu6` and `bbmu6X` datasets.

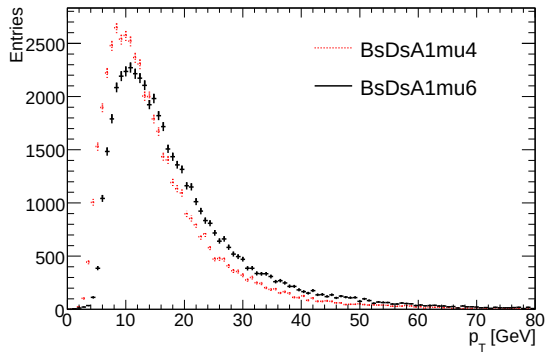

(a) $p_T^{\text{truth}}(B_s^0)$

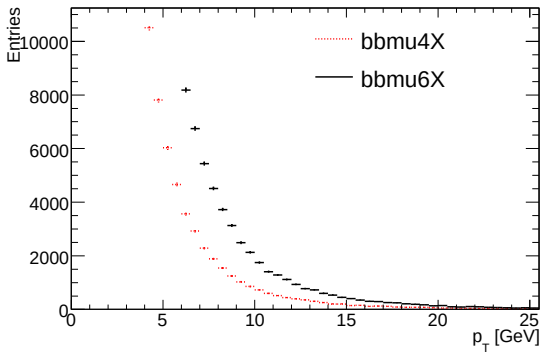

(b) $p_T^{\text{truth}}(\mu_{\text{highest } p_T})$

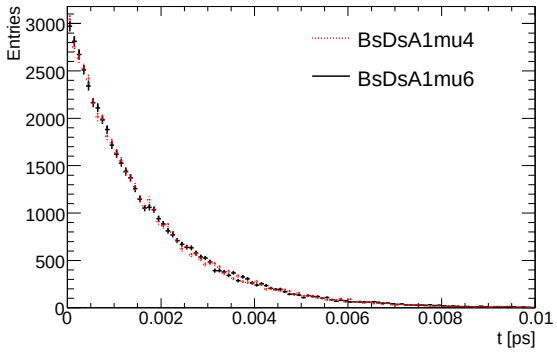

(c) $t^{\text{truth}}(B_s^0)$

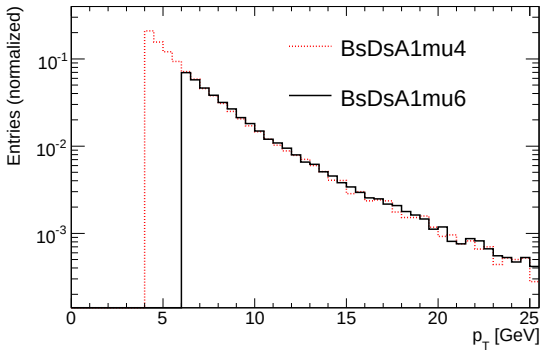

(d) $p_T^{\text{truth}}(\mu_{\text{highest } p_T})$ (normalized)

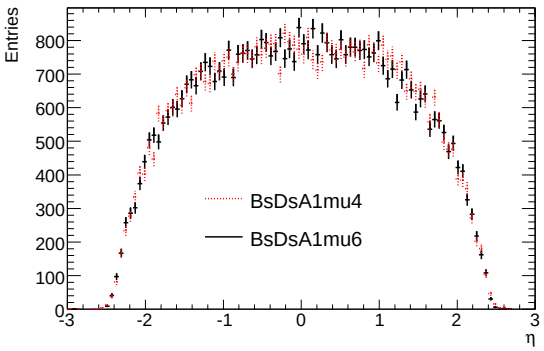

(e) $\eta^{\text{truth}}(B_s^0)$

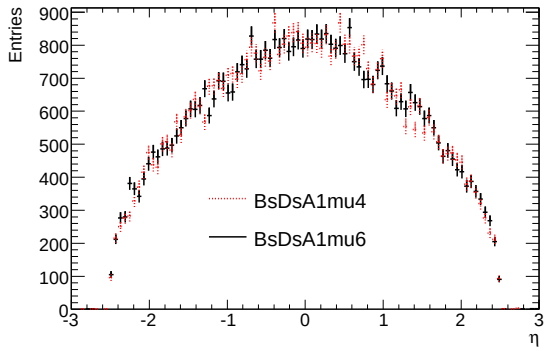

(f) $\eta^{\text{truth}}(\mu_{\text{highest } p_T})$

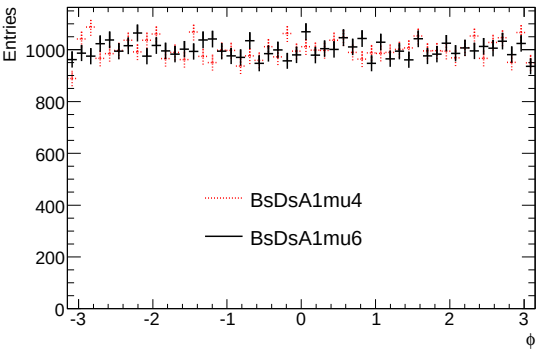

(g) $\phi^{\text{truth}}(B_s^0)$

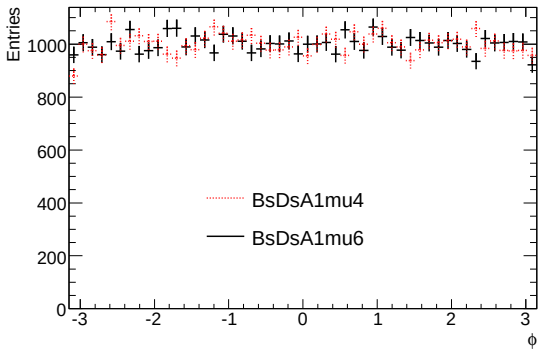

(h) $\phi^{\text{truth}}(\mu_{\text{highest } p_T})$

Figure 8.1: Distributions of the kinematic variables p_T, η and ϕ of the B_s^0 particles and $\mu_{\text{highest } p_T}$ as well as the proper decay time t^{truth} of the B_s^0 particles in the `BsDsA1mu6` and `BsDsA1mu4` samples (MC truth). The normalized p_T distributions of $\mu_{\text{highest } p_T}$ (logarithmic scale) show that the shape of the p_T distribution is unaffected by the different generation cuts.

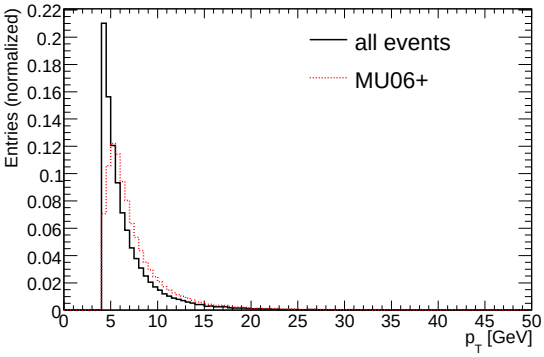

(a) $p_T^{\text{truth}}(\mu_{\text{highest } p_T})$ in `BsDsA1mu4` sample

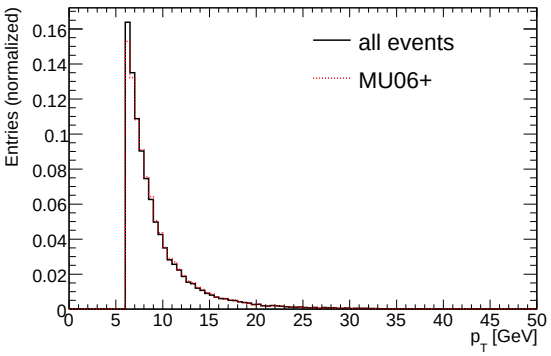

(b) $p_T^{\text{truth}}(\mu_{\text{highest } p_T})$ in `BsDsA1mu6` sample

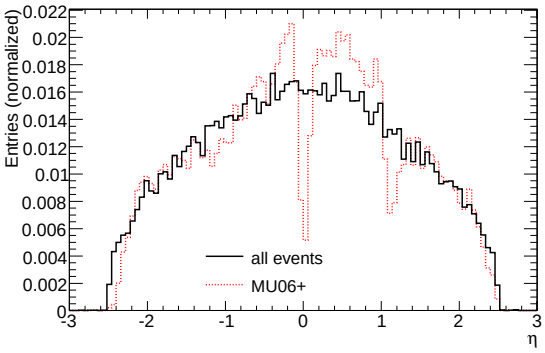

(c) $\eta^{\text{truth}}(\mu_{\text{highest } p_T})$ in `BsDsA1mu4` sample

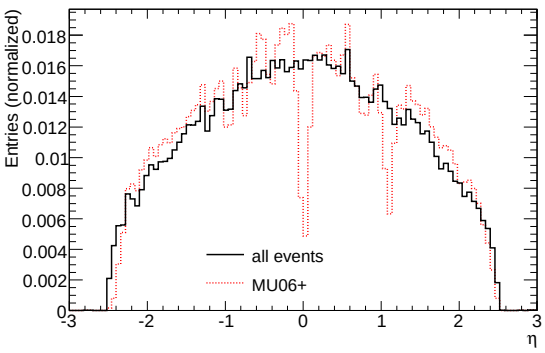

(d) $\eta^{\text{truth}}(\mu_{\text{highest } p_T})$ in `BsDsA1mu6` sample

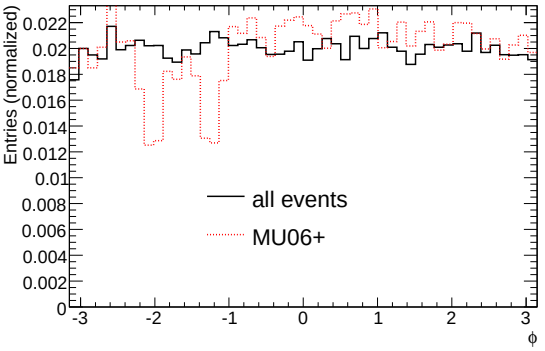

(e) $\phi^{\text{truth}}(\mu_{\text{highest } p_T})$ in `BsDsA1mu4` sample

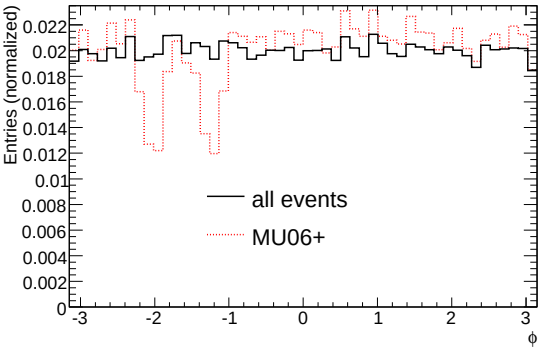

(f) $\phi^{\text{truth}}(\mu_{\text{highest } p_T})$ in `BsDsA1mu6` sample

Figure 8.2: Distributions of the kinematic variables of $\mu_{\text{highest } p_T}$ in the `BsDsA1mu4` and `BsDsA1mu6` samples (MC truth), taking into account only events passing `MU06+` (normalized with respect to the number of entries). The dips in the η and ϕ distributions are caused by "blind spots" of the LVL1 muon trigger (section 9.1.1). In η, the reduction of the efficiency is much smaller for $\eta = -1$ than for $\eta = 1$ (barrel-end-cap transition regions). This is due to the dominance of negative muons in the signal samples.

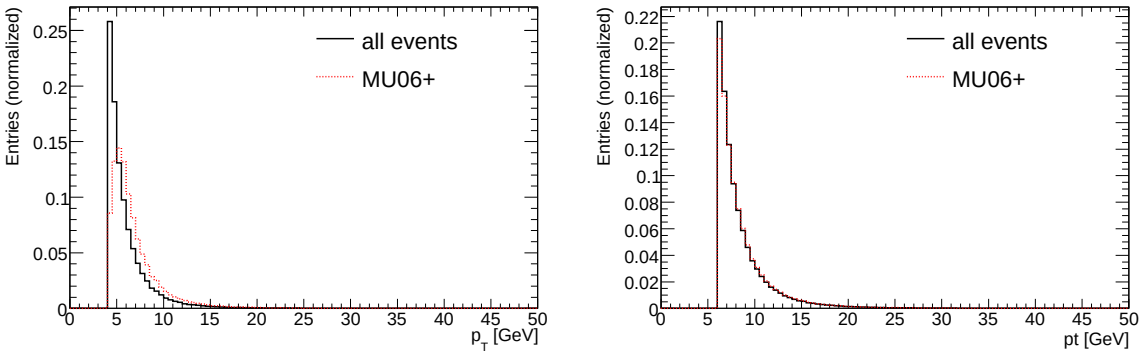

(a) $p_T^{\text{truth}}(\mu_{\text{highest } p_T})$ for `bbmu4X` sample

(b) $p_T^{\text{truth}}(\mu_{\text{highest } p_T})$ for `bbmu6X` sample

Figure 8.3: Normalized p_T distributions (with respect to the number of entries) of $\mu_{\text{highest } p_T}$ in the `bbmu4X` and `bbmu6X` samples (MC truth), taking into account only events passing `MU06+`.

The `MU06+` trigger hardly affects the p_T distributions of the `BsDsA1mu6` and `bbmu6X` datasets (figures 8.2(b) and 8.3(b)). For the `BsDsA1mu4` and `bbmu4X` datasets, though, the spectra are shifted to higher p_T values (figures 8.2(a) and 8.3(a)). These shifts are caused by the fraction of events in the two samples without muons above the p_T threshold.
For the LVL1 muon trigger, a change of the η and ϕ distributions is expected because of its measurement principle, which is susceptible to gaps between muon trigger chambers (figures 8.2 and 8.4), see also section 9.1.1.
The change due to "blind spots" is expected to differ for the signal and background datasets, as negative muons dominate the signal datasets, which only contain B_s^0 decays, but no $\bar{B}_s^0$ decays, as explained in section 7.1. The `bbmu6X` and `bbmu4X` datasets contain $(50.05 \pm 0.10)\,\%$ and $(50.09 \pm 0.16)\,\%$ negative $\mu_{\text{highest } p_T}$, respectively. In the other half of the events, $\mu_{\text{highest } p_T}$ carries a positive charge.

8.2.2 LVL1 Jet Trigger

The LVL1 jet trigger hardly affects the p_T distributions of the B_s^0 mesons, as the `JT04` threshold offers a high acceptance even for the low-p_T events of the `BsDsA1mu4` sample. For the `BsDsA1mu4` dataset, the p_T spectrum is slightly shifted towards higher p_T values (figure B.6), and there is no discernable difference in the η distributions. The ϕ distributions for both signal datasets show an asymmetry in ϕ (figure 8.5): For $\phi < 0$, a larger share of the events pass `JT04` than for $\phi > 0$. The reason for this lies within the detector description used: `ATLAS-CSC-01-02-00` introduces additional material in the upper detector hemisphere ($\phi > 0$), which adds to the amount of material in front of the calorimeter system, affecting its response.

8.2.3 LVL2 $D_s^{\pm}$ Trigger

For the `BsDsA1mu6` sample, three effects are observed both for the trigger signature using regions of interest (RoIs) and the trigger signature based on a full scan (FS):

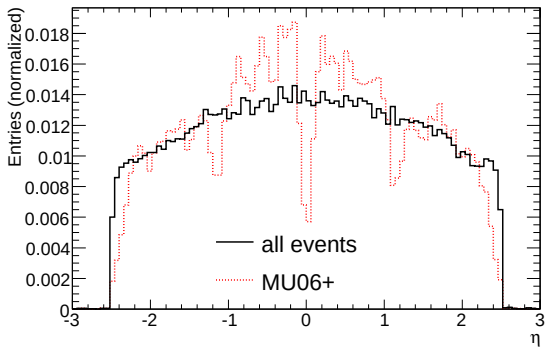

(a) $\eta^{\text{truth}}(\mu_{\text{highest } p_T})$ in `bbmu4X` sample

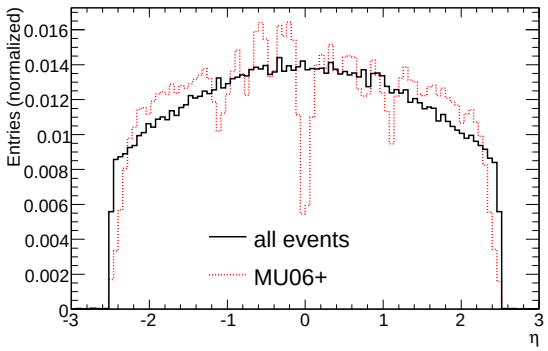

(b) $\eta^{\text{truth}}(\mu_{\text{highest } p_T})$ in `bbmu6X` sample

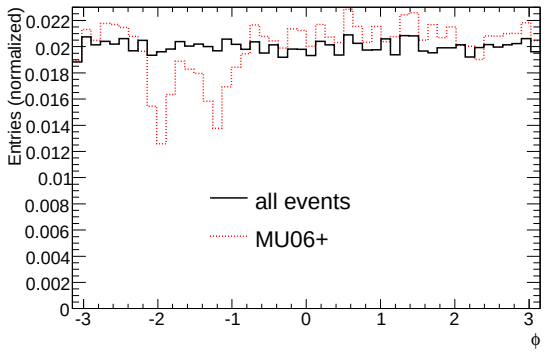

(c) $\phi^{\text{truth}}(\mu_{\text{highest } p_T})$ in `bbmu4X` sample

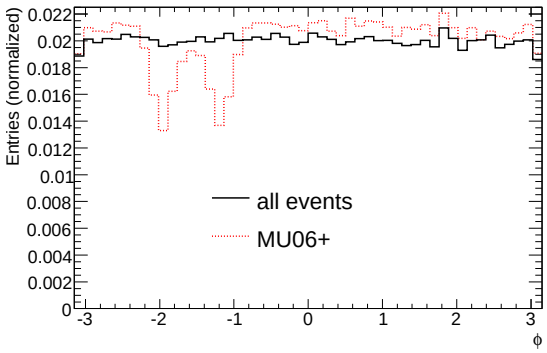

(d) $\phi^{\text{truth}}(\mu_{\text{highest } p_T})$ in `bbmu6X` sample

Figure 8.4: η and ϕ distributions of $\mu_{\text{highest } p_T}$ in the `bbmu4X` and `bbmu6X` samples (MC truth), taking into account only events passing `MU06+` (normalized with respect to the number of entries). The same "dips" as in figure 8.2 are observed.

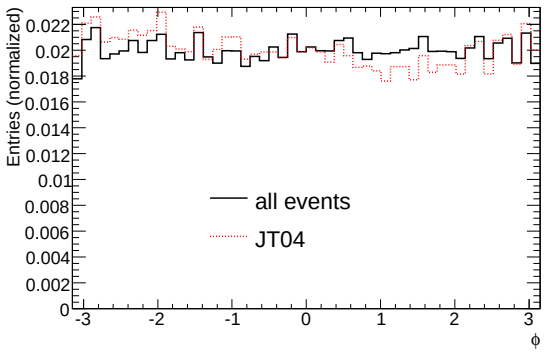

(a) $\phi^{\text{truth}}(B_s^0)$ in `BsDsA1mu4` sample

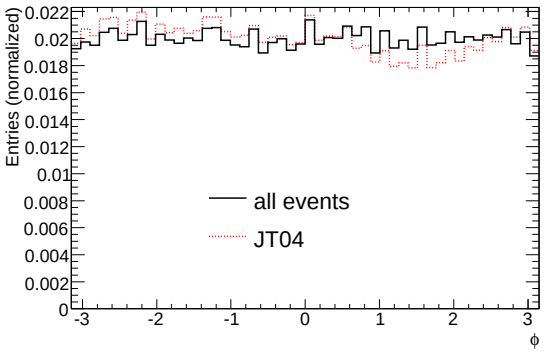

(b) $\phi^{\text{truth}}(B_s^0)$ in `BsDsA1mu6` sample

Figure 8.5: ϕ distributions of the B_s^0 particles in the `BsDsA1mu4` and `BsDsA1mu6` samples (MC truth), taking into account only events passing `JT04` (normalized with respect to the number of entries). The asymmetry in ϕ is a feature of the `ATLAS-CSC-01-02-00` detector description, which describes additional material introduced into the detector description for $\phi > 0$ (section 6.1.2).

1. Figure 8.6 shows a shift of the p_T distributions towards higher values for events passing LVL2. The shift is more pronounced for the RoI-based approach (section 9.1.1). The common part of the shift is due to an increased reconstruction efficiency of the LVL2 $D_s^{\mp}$ trigger for high-p_T events (see section 9.1.1).

2. The kinematic distributions for LVL2 passes are narrower in η. Both the shift to higher p_T values and a reduced track reconstruction efficiency in the endcap regions contribute to this. The reduction is caused by a bug in the track reconstruction code of the second-level (LVL2) trigger and is estimated to be about 10 to 15 % [49].

3. Both the ϕ distributions for `MU06+` and for `LVL2&&MU06+` show less entries in the region $1 < \phi < 2$. This is an effect of the LVL1 muon trigger: The ϕ range in question corresponds to the detector region opposite the detector feet, which reduce the trigger efficiency for opposite-side muons. This leads to less events passing the FS-based trigger for B_s^0 directions $1 < \phi < 2$. In the case of the `RoI` trigger, also the extra material added in `ATLAS-CSC-01-02-00` deteriorates the calorimeter performance for $\phi > 0$, impacting the efficiency of the RoI-based trigger.

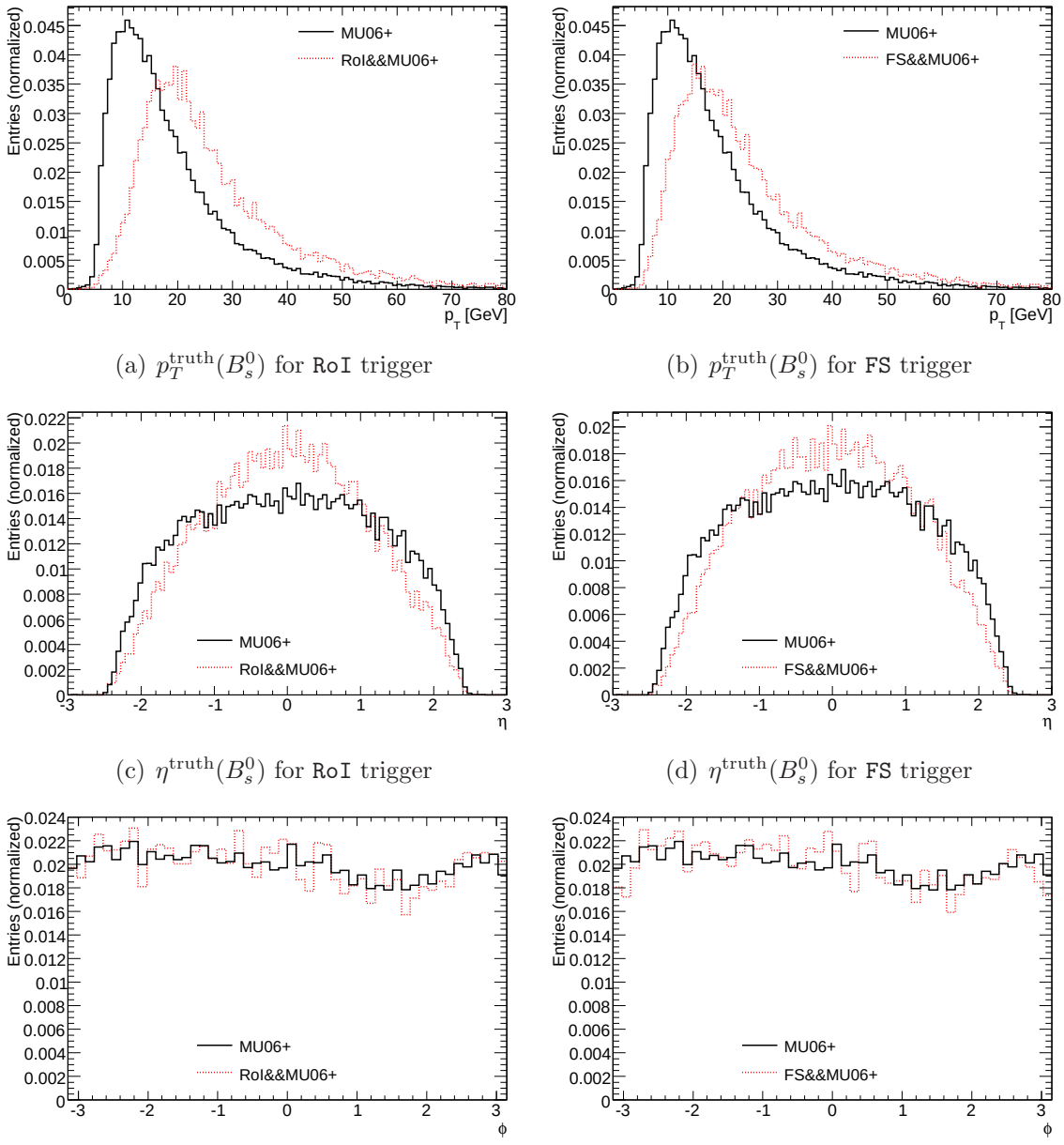

(a) $p_T^{\text{truth}}(B_s^0)$ for `RoI` trigger

(b) $p_T^{\text{truth}}(B_s^0)$ for `FS` trigger

(c) $\eta^{\text{truth}}(B_s^0)$ for `RoI` trigger

(d) $\eta^{\text{truth}}(B_s^0)$ for `FS` trigger

(e) $\phi^{\text{truth}}(B_s^0)$ for `RoI` trigger

(f) $\phi^{\text{truth}}(B_s^0)$ for `FS` trigger

Figure 8.6: Normalized distributions (with respect to the number of entries) of the kinematic variables of the B_s^0 particles in the `BsDsA1mu6` sample (MC truth), comparing events passing `MU06+` and events that also pass `RoI` and `FS`. The LVL2 trigger selection in both cases prefers events with higher p_T values (`RoI` more than `FS`, see also section 9.1.1) and hence also events with small values of $|\eta|$.

Chapter 9

Trigger Efficiency

Trigger efficiencies are obtained by considering two distributions of a kinematic variable upon which different trigger requirements have been imposed. Within this chapter, studies about the general dependence of trigger efficiencies on kinematic variables ("all events") are summarized and the subset of events passing the $B_s^0 \to D_s^- a_1^+$ selection cuts ("selection cut passes") are separately examined. The latter study is of special interest for understanding how the event numbers available for a mixing analysis are affected by the trigger strategy.
For an analysis of the rate at which the LVL2 $D_s^\mp$ trigger algorithm based on regions of interest (RoIs) is initiated (seeding rate), section 9.2 presents RoI multiplicities for the datasets used.
Section 9.3 compares the mass resolution of the LVL2 trigger to the mass windows for the $D_s^\mp$ and ϕ candidates.

9.1 Trigger Acceptance

9.1.1 Acceptance for All Events

The LVL1 muon trigger is limited by the design criterion that it needs to be able to resolve events from consecutive bunch crossings. Due to this requirement and the need to limit the LVL1 latency to a maximum of 2.5 μs, fast muon chambers offering a less precise p_T measurement are employed (section 5.2.2). In order to maintain both a high signal efficiency and a good background rejection, the coincidence matrices of the LVL1 muon trigger correspond to a loose p_T cut: The efficiency curves extend significantly into the region below the respective thresholds (figures 9.1 and 9.2). The LVL2 trigger provides a means of confirming the LVL1 decision with data from precision chambers and from the inner detector [30]. The LVL2 muon confirmation is not discussed within this thesis, as it is not available in the datasets used.
The dependence of the `MU06+` trigger acceptance on the transverse momentum of the muon with the highest p_T in the event ($\mu_{\text{highest } p_T}$) is shown in figures 9.1(a) and 9.1(b) for the signal datasets. As expected, the largest part of the rising edge of the trigger efficiency in dependence of the p_T of $\mu_{\text{highest } p_T}$ can only be seen in the `mu4` samples.

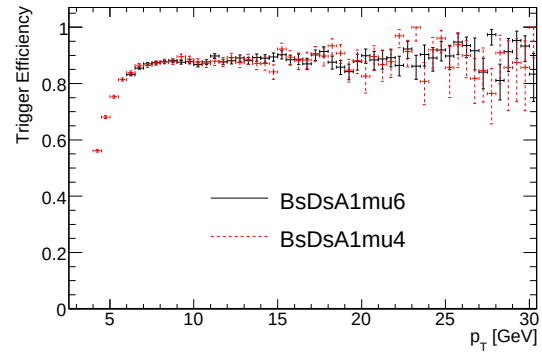

(a) $p_T^{\text{truth}}(\mu_{\text{highest } p_T})$ for `MU00+`

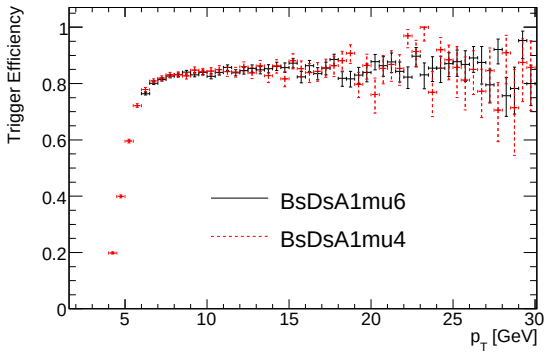

(b) $p_T^{\text{truth}}(\mu_{\text{highest } p_T})$ for `MU06+`

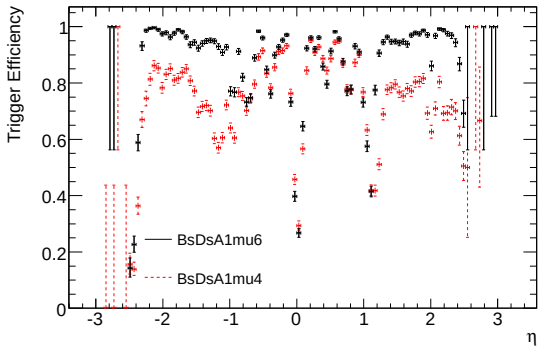

(c) $\eta^{\text{truth}}(\mu_{\text{highest } p_T})$ for `MU00+`

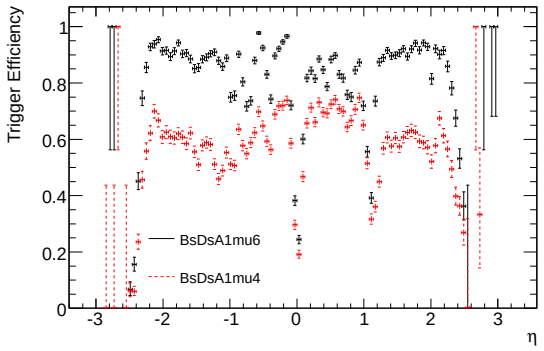

(d) $\eta^{\text{truth}}(\mu_{\text{highest } p_T})$ for `MU06+`

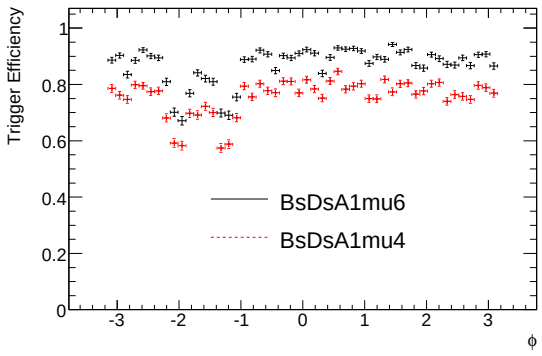

(e) $\phi^{\text{truth}}(\mu_{\text{highest } p_T})$ for `MU00+`

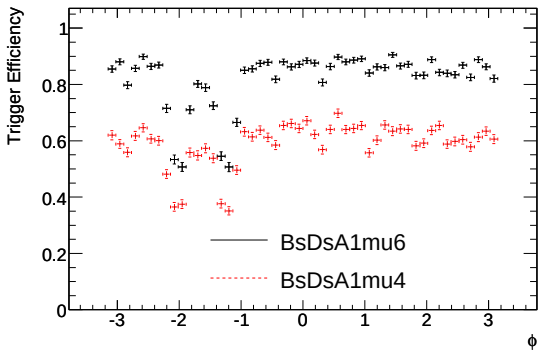

(f) $\phi^{\text{truth}}(\mu_{\text{highest } p_T})$ for `MU06+`

Figure 9.1: Trigger efficiencies for the `MU00+` and `MU06+` trigger signatures in dependence of the kinematic variables of $\mu_{\text{highest } p_T}$ in the `BsDsA1mu6` and `BsDsA1mu4` datasets. The overall trigger acceptance for `BsDsA1mu4` is significantly lower because a fraction of the events has no muon above the p_T treshold.

Table 9.1: Overview: Trigger Efficiencies. The numbers given are percentages. The black numbers refer to all events, while the red numbers concern the subset of the selection cut passes only. The LVL2 results for the `BsDsA1mu6` sample (gray background) refer to the adjusted LVL2 mass cuts, which reduce the efficiencies by 0.4 % (section 9.3).

Trigger signature	`BsDsA1mu6` [%]	`BsDsA1mu4` [%]	`bbmu6X` [%]	`bbmu4X` [%]	`ccmu4X` [%]
`MU00+`	86.77 ± 0.15	75.65 ± 0.19	86.60 ± 0.07	71.74 ± 0.14	70.4 ± 0.2
	87.2 ± 0.5	77.8 ± 0.7	93^{+5}_{-8}	100^{+0}_{-17}	0^{+44}_{-0}
`MU05+`	82.60 ± 0.17	68.4 ± 0.2	81.91 ± 0.08	63.51 ± 0.15	62.1 ± 0.2
	83.1 ± 0.6	71.6 ± 0.8	73^{+10}_{-12}	100^{+0}_{-17}	0^{+44}_{-0}
`MU06+`	81.90 ± 0.17	58.9 ± 0.2	81.00 ± 0.08	52.28 ± 0.16	50.4 ± 0.2
	82.4 ± 0.6	63.7 ± 0.8	73^{+10}_{-12}	100^{+0}_{-17}	0^{+44}_{-0}
`JT04`	98.38 ± 0.06	96.77 ± 0.08	94.93 ± 0.04	94.34 ± 0.07	97.14 ± 0.08
	99.43 ± 0.11	99.02 ± 0.16	100^{+0}_{-7}	100^{+0}_{-17}	100^{+0}_{-44}
`FS&&MU00+`	32.7 ± 0.2	23.79 ± 0.19	3.79 ± 0.04	2.08 ± 0.05	2.82 ± 0.08
	79.8 ± 0.6	71.9 ± 0.8	67^{+11}_{-12}	100^{+0}_{-17}	0^{+44}_{-0}
`FS&&MU05+`	31.1 ± 0.2	21.70 ± 0.18	3.60 ± 0.04	1.91 ± 0.04	2.51 ± 0.07
	76.1 ± 0.6	66.0 ± 0.8	47^{+12}_{-11}	100^{+0}_{-17}	0^{+44}_{-0}
`FS&&MU06+`	30.9 ± 0.2	19.13 ± 0.18	3.57 ± 0.04	1.71 ± 0.04	2.20 ± 0.07
	75.5 ± 0.6	58.6 ± 0.8	47^{+12}_{-11}	100^{+0}_{-17}	0^{+44}_{-0}
`RoI&&MU00+`	28.5 ± 0.2	19.82 ± 0.18	3.40 ± 0.04	1.80 ± 0.04	2.43 ± 0.07
	72.8 ± 0.7	64.0 ± 0.8	67^{+11}_{-12}	60^{+18}_{-20}	0^{+44}_{-0}
`RoI&&MU05+`	27.2 ± 0.2	18.09 ± 0.17	3.23 ± 0.04	1.66 ± 0.04	2.20 ± 0.07
	69.5 ± 0.7	58.8 ± 0.8	47 ± 12	60^{+18}_{-20}	0^{+44}_{-0}
`RoI&&MU06+`	27.0 ± 0.2	16.10 ± 0.16	3.21 ± 0.04	1.50 ± 0.04	$1.95^{+0.07}_{-0.06}$
	68.9 ± 0.7	52.5 ± 0.8	47 ± 12	60^{+18}_{-20}	0^{+44}_{-0}

Figures 9.1(c) and 9.1(d) show areas of reduced muon trigger efficiency in η:

1. At $\eta \approx 0$, a passage for cables and services for the inner detector does not allow the placement of muon trigger chambers (figure 5.4).

2. The transition from barrel-shaped detectors to the end-caps at $\eta \approx \pm 1$ affects muons of opposite charge differently: While the signal samples show a more pronounced drop of the trigger efficiency for $\eta \approx +1$ (negative muons affected) than for $\eta \approx -1$ (positive muons affected), this effect is symmetrical for the background samples, which contain approximately equal shares of events with a positive $\mu_{\text{highest } p_T}$ and events with negative $\mu_{\text{highest } p_T}$ (figures 9.2(c) and 9.2(d)).

3. There are very few muons outside pseudorapidity range of $|\eta| < 2.5$. They originate from events with a muon passing both the p_T and η cuts and a second muon with a higher p_T and outside the η cut ($|\eta| < 2.5$). Due to the muon trigger coverage ($|\eta| < 2.4$), the trigger decision depends only on the first muon.

The overall muon trigger efficiency differences between both data samples in the η and ϕ distributions (figure 9.1) are caused by the reduced trigger acceptance for low-p_T muons contained in the `BsDsA1mu4` dataset. The difference is therefore more pronounced for the `MU06+` trigger signature than for `MU00+`.
The trigger efficiencies in dependence of ϕ (figures 9.1(e) and 9.1(f)) show areas of reduced acceptance at $\phi \approx -2$ and $\phi \approx -1$, which are caused by the detector feet. A more detailed examination of the "blind spots" of the barrel part of the muon trigger has been performed in [38].
Similar efficiency plots for the `bbmu4X` and `bbmu6X` samples are found in figure 9.2.
From all events of the datasets, LVL1 muon trigger efficiencies of 81-87 % are concluded for low-p_T signatures of the LVL1 muon trigger on `mu6` samples. The acceptances for the `mu4` datasets are significantly lower, see table 9.1.
The LVL1 jet trigger offers a good acceptance of above 90 % even for events with a p_T of about 4 GeV (figure 9.3). Due to the different cuts on transverse momenta for the `BsDsA1mu6` and `BsDsA1mu4` samples, the numbers of events with $p_T(B_s^0) < 6\,\text{GeV}$ are very different for the two datasets. The $B_s^0 \to D_s^- a_1^+$ analysis imposes a p_T cut on the reconstructed B_s^0 mesons of 10 GeV, for which the trigger acceptance is above 95 %. It is important to note that these studies cannot determine how the LVL1 jet trigger efficiency for the RoI containing the B_s^0 decay depends on the energy threshold. This can neither be done by the RoI multiplicity study described in section 9.2. To determine the efficiency for the RoIs containing passing $D_s^\mp$ candidates, re-running reconstruction with different LVL1 jet trigger thresholds as RoI seeds would be necessary.
The efficiencies of the LVL2 trigger signatures based on a full scan or an RoI-based search, requiring a trigger muon of at least 6 GeV on LVL1, are denoted by `LVL2&&MU06+`. Their dependencies on kinematic variables of the event are shown in figure 9.5. The efficiency differences in figures 9.5(a) and 9.5(b) between the signal datasets originate from the `MU06+` trigger signature. This is concluded from figures 9.5(c) and 9.5(d): The muon trigger rejects a large share of the events with $p_T(\mu_{\text{highest } p_T})$ below the threshold of 6 GeV.
The trigger efficiency in dependence of the p_T of the B_s^0 meson is lower for the `RoI&&MU06+` trigger than for the `FS&&MU06+` trigger, especially in the low-p_T area (figure 9.6). Due to this effect, the overall efficiencies of the FS trigger are about 3-4 % higher than those of the RoI-guided approach (see also table 9.1). The dependencies of the `LVL2&&MU06+` trigger efficiencies on the η and ϕ distributions of $\mu_{\text{highest } p_T}$ are again dominated by the `MU06+` trigger, showing the same low-p_T cut-off effect (figure 9.4).

9.1.2 Acceptance for Reconstructable Events

In order to examine the impact of the trigger strategy on the number of events available for the mixing analysis, the quality of the events passing the trigger has to be taken into account: Only those events passing the selection cuts of the $B_s^0 \to D_s^- a_1^+$ analysis contribute to the mixing analysis.
Figure 9.7 shows the dependence of the trigger efficiency for selection cut passes on

Table 9.2: Mean and root mean square of the RoI multiplicity distributions (figure 9.8) for the background samples in dependence of the jet RoI energy threshold. A strong anticorrelation between the energy threshold and the mean RoI multiplicity is observed.

Threshold	bbmu4X		bbmu6X		ccmu4X	
	Mean	RMS	Mean	RMS	mean	RMS
4 GeV	2.847	1.746	2.883	1.754	3.235	1.759
5 GeV	1.301	1.244	1.441	1.295	1.643	1.300
6 GeV	0.703	0.952	0.881	1.046	0.998	1.048
7 GeV	0.454	0.786	0.634	0.911	0.703	0.900

the transverse momentum of the B_s^0 meson. For both requirements `RoI&&MU06+` and `FS&&MU06+`, the distributions agree above $p_T(B_s^0) > 20\,\text{GeV}$. For lower p_T values, the `RoI&&MU06+` trigger offers a higher efficiency than the `RoI&&MU06+` trigger. There are two contributions to the difference in the efficiencies: On the one hand, the RoI containing the $D_s^{\mp}$ decay products is less likely to pass the energy threshold of the RoI trigger in this p_T region. Judging from the trigger efficiency of the `JT04` trigger for low p_T values of the B_s^0 meson (figure 9.3), this contribution is small for p_T values above 10 GeV. In order to check the influence of the RoI energy threshold, rerunning the reconstruction with different LVL1 jet trigger seeds would be necessary. On the other hand, the lower transverse boost may allow the decay products of the $D_s^{\mp}$ meson to escape the RoI in the case of a B_s^0 meson of low p_T, causing a reduction of the RoI trigger efficiency.
The $B_s^0 \to D_s^- a_1^+$ analysis cuts on the reconstructed $p_T(B_s^0) > 10\,\text{GeV}$. According to the kinematic distributions of the p_T of the B_s^0 mesons in the samples (figure 8.1(a)), most reconstructed B_s^0 mesons will fall into this range. Therefore, the overall efficiencies for reconstructable events from the `BsDsA1mu4` and `BsDsA1mu6` samples are about 6-8 % higher for the FS-based approach than for the RoI-based trigger strategy (see also table 9.1).

9.2 Multiplicity of LVL1 Jet Regions of Interest

The RoI multiplicity for background processes is an important input for trigger timing studies (chapter 11). Together with background event rates (chapter 10), it determines at which rate the LVL2 $D_s^{\mp}$ trigger is seeded.
Therefore, the RoI multiplicity has to be adjusted to a value that results in a LVL2 seeding rate the high-level trigger (HLT) can handle. This is achieved by setting the jet RoI energy threshold: The higher the threshold energy is set, the fewer RoIs per event pass the threshold requirement. The results for the `bbmu6X`, `bbmu4X`, and `ccmu4X` data samples are shown in figure 9.8 and table 9.2.
Figures 9.8(d) and 9.8(e) show the RoI multiplicity distributions obtained from `L1JetObjects` within the signal samples. The numbers of entries in the bin corresponding to zero RoIs is of particular interest: From this information, the efficiency of the LVL1 jet trigger for different thresholds is obtained (table 9.3). A comparison

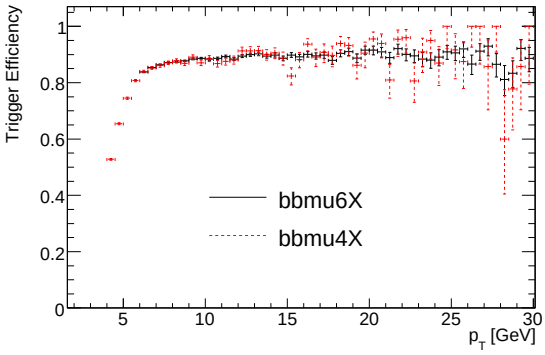

(a) $p_T^{\text{truth}}(\mu_{\text{highest } p_T})$ for MU00+

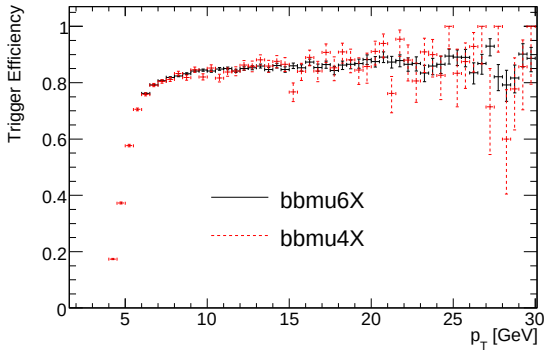

(b) $p_T^{\text{truth}}(\mu_{\text{highest } p_T})$ for MU06+

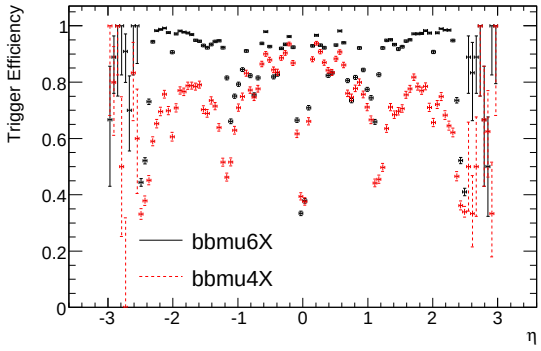

(c) $\eta^{\text{truth}}(\mu_{\text{highest } p_T})$ for MU00+

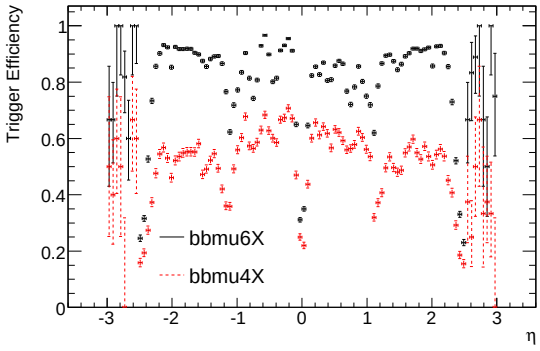

(d) $\eta^{\text{truth}}(\mu_{\text{highest } p_T})$ for MU06+

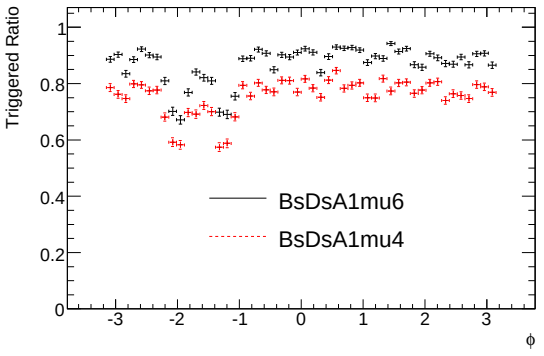

(e) $\phi^{\text{truth}}(\mu_{\text{highest } p_T})$ for MU00+

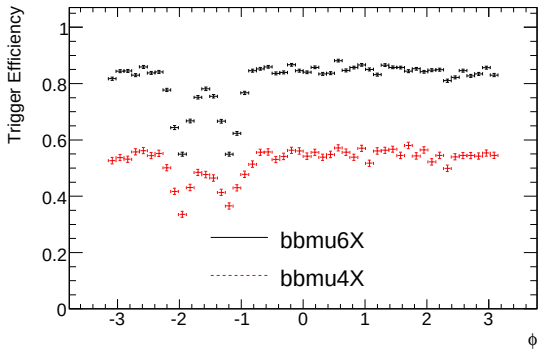

(f) $\phi^{\text{truth}}(\mu_{\text{highest } p_T})$ for MU06+

Figure 9.2: Trigger efficiencies for the MU00+ and MU06+ trigger signatures in the bbmu6X and bbmu4X datasets.

Table 9.3: Jet trigger efficiencies for the signal samples obtained from the L1JetObjects. The efficiency difference of about 0.4 % to the values cited in table 9.1 is caused by an additional cut applied on the L1JetObjects: $|\eta| < 2.4$.

Threshold	BsDsA1mu4 [%]	BsDsA1mu6 [%]
4 GeV	96.31±0.08	98.00±0.06
5 GeV	81.82±0.17	88.63±0.14
6 GeV	65.8±0.2	76.86±0.19
7 GeV	54.4±0.2	67.1±0.2

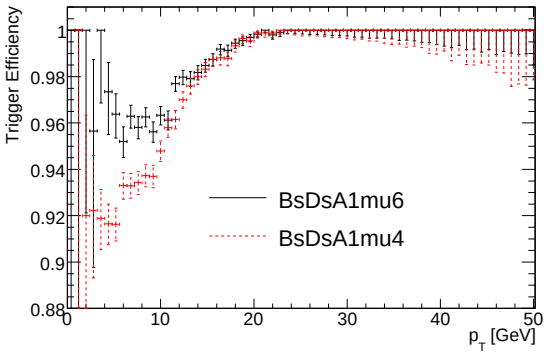

(a) $p_T^{\text{truth}}(B_s^0)$

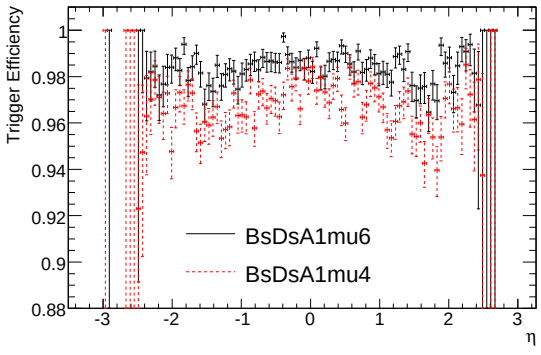

(b) $\eta^{\text{truth}}(B_s^0)$

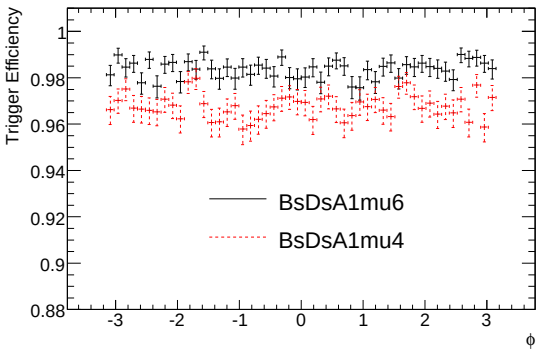

(c) $\phi^{\text{truth}}(B_s^0)$

Figure 9.3: Trigger efficiencies for the `JT04` trigger signature in dependence of the kinematic variables of the B_s^0 mesons in the `BsDsA1mu6` and `BsDsA1mu4` datasets (zero suppressed). The differences between the η and ϕ distributions of the `BsDsA1mu6` and `BsDsA1mu4` datasets are caused by the fraction of the events with B_s^0 mesons with low p_T values. This fraction is larger in the `BsDsA1mu4` sample.

to table 9.1 reveals an efficiency difference of about 0.4 % for the `JT04` trigger signatures. The reason is an additional cut on the pseudorapidity of the `L1JetObjects` $|\eta| < 2.4$, which is applied before evaluating the RoI multiplicity. This cut ensures that most of the RoI is located within the pseudorapidity range covered by the tracking detectors.

However, these numbers constitute a good estimate of the dependence of the LVL1 jet trigger acceptance on the energy threshold. They cannot be used for exact LVL2 estimates, because it cannot be concluded whether the RoIs failing a stricter threshold requirement contain the $D_s^{\mp}$ decay. Therefore, a study with different LVL2 RoI seeding thresholds is necessary to determine the effect on the RoI trigger efficiency.

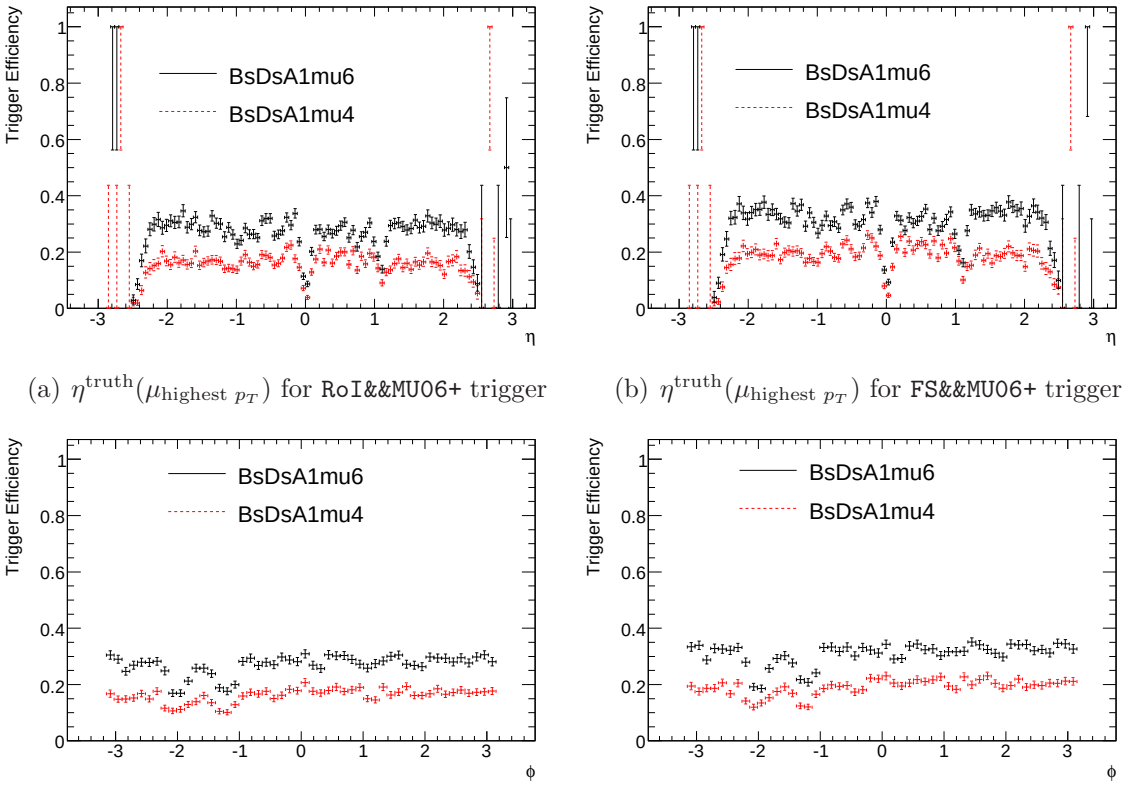

(a) $\eta^{\text{truth}}(\mu_{\text{highest } p_T})$ for `RoI&&MU06+` trigger

(b) $\eta^{\text{truth}}(\mu_{\text{highest } p_T})$ for `FS&&MU06+` trigger

(c) $\phi^{\text{truth}}(\mu_{\text{highest } p_T})$ for `RoI&&MU06+` trigger

(d) $\phi^{\text{truth}}(\mu_{\text{highest } p_T})$ for `FS&&MU06+` trigger

Figure 9.4: Trigger efficiencies as functions of η and ϕ of $\mu_{\text{highest } p_T}$ for the `RoI&&MU06+` and `FS&&MU06+` trigger signatures in the `BsDsA1mu6` and `BsDsA1mu4` datasets. The differences between the η- and ϕ-dependent efficiencies of the two samples are caused by the LVL1 muon trigger.

9.3 LVL2 Mass Cuts

The invariant mass obtained from track combinations is the means by which the LVL2 $D_s^{\mp}$ hypothesis algorithm judges whether to accept or reject particle candidates. Therefore, it is crucial to check how the invariant mass window applied by the LVL2 $D_s^{\mp}$ hypothesis algorithm relates to the invariant mass resolution of the LVL2 track reconstruction performed by the LVL2 feature extraction. An evaluation of the results written to the `TrigL2Bphys` objects allows to check the set of mass cuts in the `CSC-06-900GeV` trigger menu:

$$1908\,\text{MeV} < m(D_s^{\mp}) < 2040\,\text{MeV}, \tag{9.1}$$

$$1005\,\text{MeV} < m(\phi) < 1035\,\text{MeV}. \tag{9.2}$$

If a $D_s^{\mp}$ candidate passes cut (9.1) and its associated ϕ candidate simultaneously passes cut (9.2), the event is accepted by the LVL2 $D_s^{\mp}$ trigger.
The distributions of the invariant masses obtained from LVL2 track fits for the ϕ and $D_s^{\mp}$ candidates are shown in figure 9.9 for the `BsDsA1mu6` and `bbmu6X` datasets. Note that the distributions for the FS- and RoI-guided approaches closely resemble each

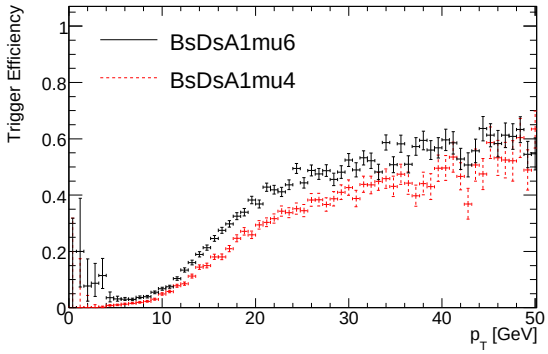

(a) $p_T^{\text{truth}}(B_s^0)$ for `RoI&&MU06+` trigger

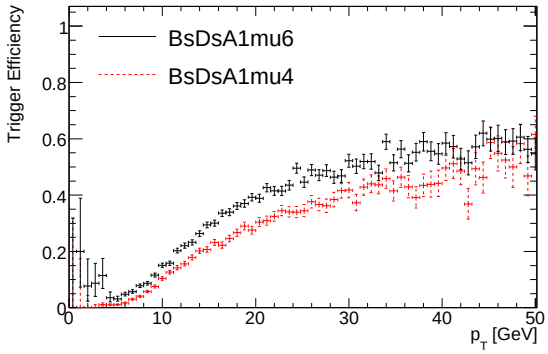

(b) $p_T^{\text{truth}}(B_s^0)$ for `FS&&MU06+` trigger

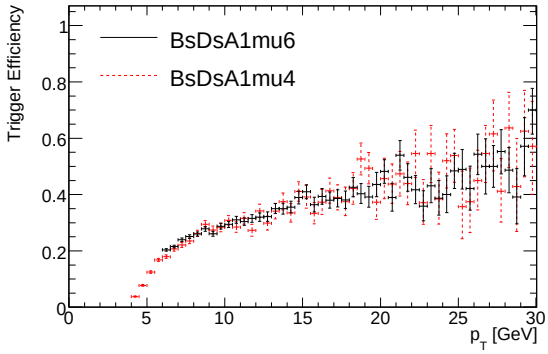

(c) $p_T^{\text{truth}}(\mu_{\text{highest } p_T})$ for `RoI&&MU06+` trigger

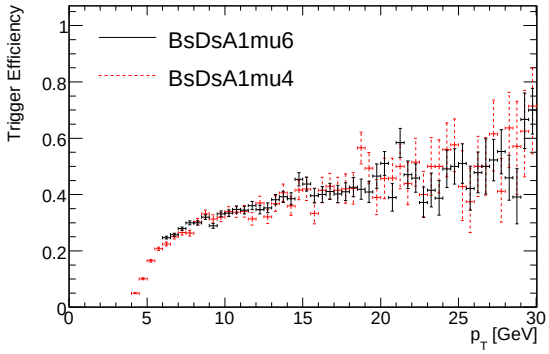

(d) $p_T^{\text{truth}}(\mu_{\text{highest } p_T})$ for `FS&&MU06+` trigger

Figure 9.5: Trigger efficiencies in dependence of the p_T of the B_s^0 meson and of $\mu_{\text{highest } p_T}$ for the `RoI&&MU06+` and `FS&&MU06+` trigger signatures in the `BsDsA1mu6` and `BsDsA1mu4` datasets.

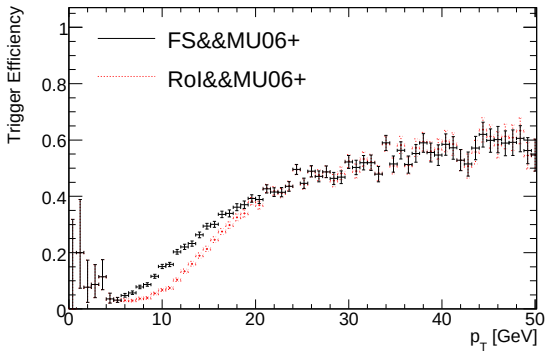

(a) $p_T^{\text{truth}}(B_s^0)$ for `BsDsA1mu6`

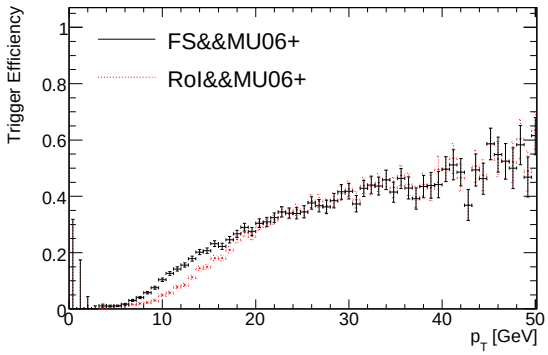

(b) $p_T^{\text{truth}}(B_s^0)$ for `BsDsA1mu4`

Figure 9.6: Trigger efficiencies in dependence of the p_T of the B_s^0 meson for the `RoI&&MU06+` and `FS&&MU06+` trigger signatures in the `BsDsA1mu6` and `BsDsA1mu4` datasets. For both datasets, the efficiency of the FS-based trigger is higher than the efficiency of the RoI-based trigger in the low-p_T area.

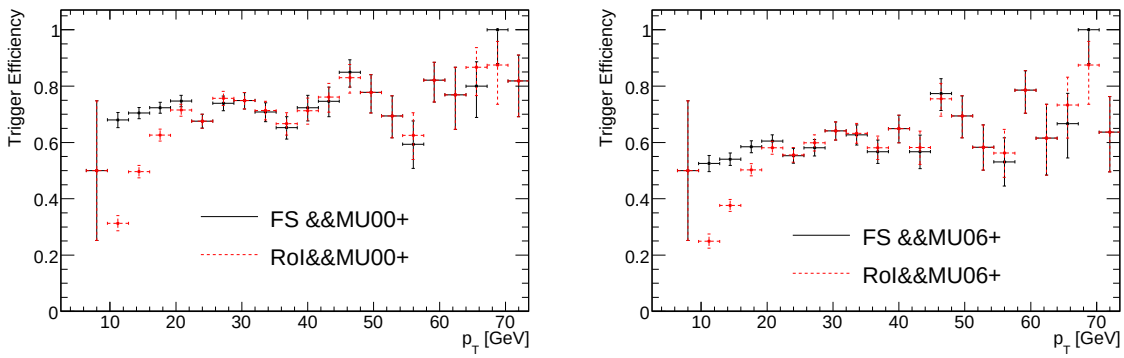

(a) `LVL2&&MU00+` (b) `LVL2&&MU06+`

Figure 9.7: Trigger efficiencies for the `LVL2&&MU00+` and `LVL2&&MU06+` trigger signatures as a function of the p_T of the B_s^0 meson for the selection cut passes in the `BsDsA1mu4` dataset.

other. The signal peaks are approximately centered on the PDG mass values, on top of combinatorial background, that is, candidates from other track combinations within the signal events. For an evaluation of the mass resolutions, only truth matched candidates from events with a p_T of the B_s^0 meson of at least 10 GeV are used (figure 9.10). This cut corresponds to cut (7.25) on the reconstructed p_T of the B_s^0 meson performed by the offline analysis. For these candidates, the results for the FS- and RoI-based trigger strategies agree well.
The origins of the $D_s^\pm$ and ϕ candidates (FS or RoI) can only be evaluated by the offline analysis for the `BsDsA1mu6` dataset. The other datasets do not permit a separate evaluation of candidates originating from FS or from RoIs.
Note that the LVL2 $D_s^\mp$ mass cut (9.1) is asymmetric around the $D_s^\mp$ mass [4]:

$$m_{\mathrm{PDG}}(D_s^\mp) = (1968.2 \pm 0.5)\,\mathrm{MeV},$$

while the ϕ mass cut is symmetric:

$$m_{\mathrm{PDG}}(\phi) = (1019.460 \pm 0.019)\,\mathrm{MeV}.$$

The asymmetric mass range is an error within the trigger settings, as the mass distributions (figure 9.10) for true and background candidates do not motivate choosing an asymmetric mass window.
The trigger decision by the $D_s^\mp$ trigger can be reproduced from the `TrigL2Bphys` data. It is thus checked how changing the LVL2 $D_s^\mp$ mass range to a symmetric interval inside the range implemented in Athena release 12 affects the LVL2 efficiency. The observed efficiency for signal events is only 0.4 % lower for any of the `LVL2&&MU0X+` signatures, both for all events and for selection cut passes only, when changing (9.1) to

$$1908\,\mathrm{MeV} < m(D_s^\mp) < 2028\,\mathrm{MeV}, \tag{9.3}$$

which has therefore been set in the next Athena release 13.

Table 9.4: Results of Gaussian fits to figure 9.11. The mass resolution decreases with increasing $|\eta|$.

Pseudorapidity range	Mean $D_s^{\mp}$ candidate mass [MeV]	σ of $D_s^{\mp}$ candidate mass distribution [MeV]
all	1966.9±0.3	21.7±0.3
$\lvert\eta\rvert < 1$	1967.3±0.3	19.3±0.3
$1 < \lvert\eta\rvert < 1.5$	1965.8±0.8	26.3±1.0
$\lvert\eta\rvert > 1.5$	1965.6±1.3	32±2
Fit range [MeV]	$1930 < m(D_s^{\mp}) < 2005$	
Pseudorapidity range	Mean ϕ candidate mass [MeV]	σ of ϕ candidate mass distribution [MeV]
all	1019.55±0.05	5.07±0.06
$\lvert\eta\rvert < 1$	1019.63±0.06	4.75±0.06
$1 < \lvert\eta\rvert < 1.5$	1019.46±0.12	5.31±0.13
$\lvert\eta\rvert > 1.5$	1019.32±0.18	6.1±0.2
Fit range [MeV]	$1010 < m(\phi) < 1030$	

From figure 9.10, the LVL2 invariant mass resolution is obtained by fitting Gaussian functions to the mass distributions of the ϕ and $D_s^{\mp}$ candidates. However, a Gaussian function can only approximate the detector resolution, as the mass resolution depends on the pseudorapidity of the B_s^0 meson (figure 9.11 and table 9.4).
The mass resolution is better for the barrel region ($|\eta| < 1$) than for the transition ($1 < |\eta| < 1.5$) or end-cap regions ($|\eta| > 1.5$). This effect is also seen [14] in the offline analysis[1] (table 9.5), which also resolves candidate masses better for transverse directions of flight of the particles. No significant changes in the mean reconstructed masses of the LVL2 trigger are observed. The better overall performance of the offline analysis is anticipated, because offline track fitting algorithms are optimized for precision rather than for saving computing time. Event filter (EF) algorithms are expected to reach similar resolutions as the offline analysis, as more computing time is permissible per processed event and similar reconstruction code will be used.
In the approximation of a Gaussian resolution function fit to figure 9.10, the mass ranges for the $D_s^{\mp}$ mesons (9.3) and the ϕ mesons (9.2) correspond to $2.8\,\sigma$ and $3.0\,\sigma$ centered on the mean values, respectively. Assuming normal distributions, these ranges should contain more than 99 % of the proper candidates, which is sufficient for the LVL2 trigger.
As mentioned in section 7.2.1, the trigger decision does not consider the results of the LVL2 vertex fits. From these vertex fits, invariant masses for the particle candidates are extracted (figures 9.12(a) and 9.12(b)).
The mass values from the vertex fits are correlated with those obtained from the reconstructed tracks (figures 9.12(c) and 9.12(d)). As the two-dimensional distributions contain entries for which the reconstructed masses from both methods differ, a HLT trigger simulation performing cuts on the invariant masses taken from the vertex fits should be performed. Thus, it could be checked how the signal effi-

[1] For these studies, a $B_s^0 \to D_s^- a_1^+(\mu 6)$ sample produced on the Grid has been used.

Table 9.5: Results of Gaussian fits to figure 9.11 compared to results of the $B_s^0 \to D_s^- a_1^+$ offline analysis [14].

Pseudorapidity range	σ of $D_s^\mp$ candidate mass distribution [MeV]	
	LVL2 FS trigger	Offline analysis [14]
all	21.7±0.3	17.99±0.18
$\lvert\eta\rvert < 1$	19.3±0.3	15.33±0.16
$1 < \lvert\eta\rvert < 1.5$	26.3±1.0	21.8±0.6
$\lvert\eta\rvert > 1.5$	32±2	33±2
Fit range [MeV]	$1930 < m(D_s^\mp) < 2005$	
Pseudorapidity range	σ of ϕ candidate mass distribution [MeV]	
	LVL2 FS trigger	Offline analysis [14]
all	5.07±0.06	3.91±0.05
$\lvert\eta\rvert < 1$	4.75±0.06	3.66±0.05
$1 < \lvert\eta\rvert < 1.5$	5.31±0.13	3.96±0.10
$\lvert\eta\rvert > 1.5$	6.1±0.2	4.9±0.2
Fit range [MeV]	$1010 < m(\phi) < 1030$	$1013 < m(\phi) < 1026$

ciencies and background rejections of the LVL2 $D_s^\mp$ trigger implementations from trigger decisions based on vertex fits relate to the values currently obtained. Also, applying a loose cut on the vertex fit probability $P(\chi^2)$ could improve background rejection [50].

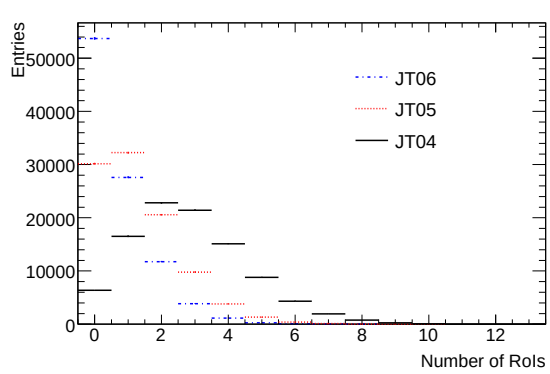

(a) `bbmu4X`

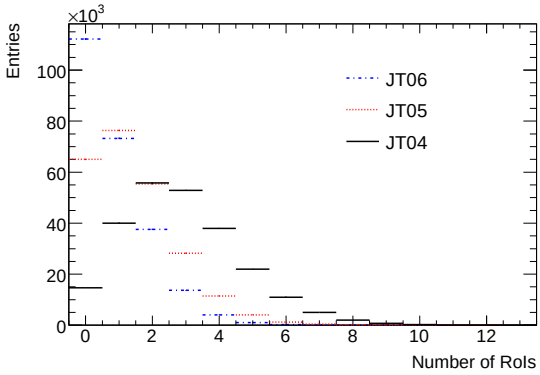

(b) `bbmu6X`

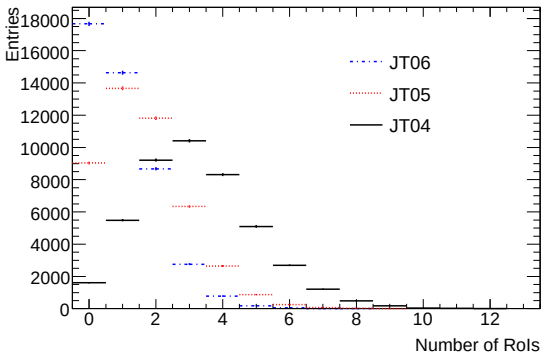

(c) `ccmu4X`

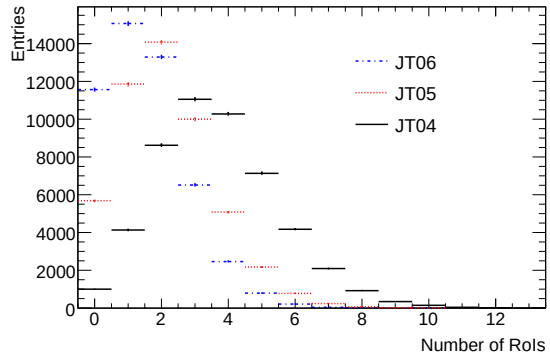

(d) `BsDsA1mu4`

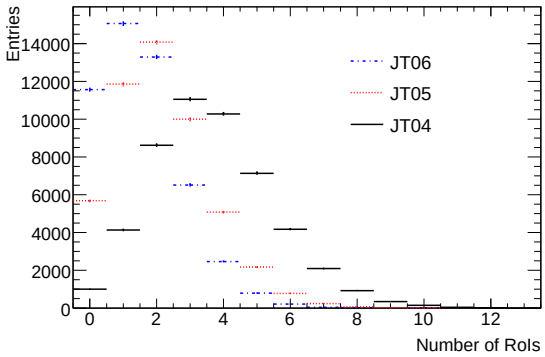

(e) `BsDsA1mu6`

Figure 9.8: RoI multiplicity distributions for the background and signal samples in dependence of the jet RoI energy threshold.

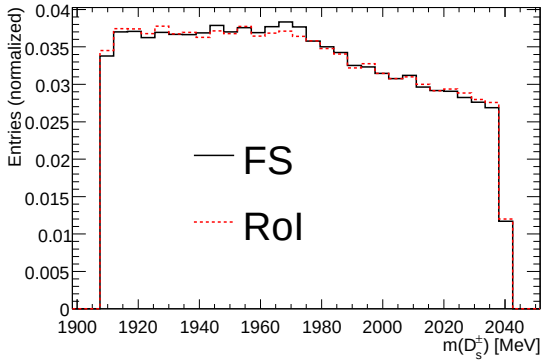

(a) $D_s^{\pm}$ candidate masses for `BsDsA1mu6`

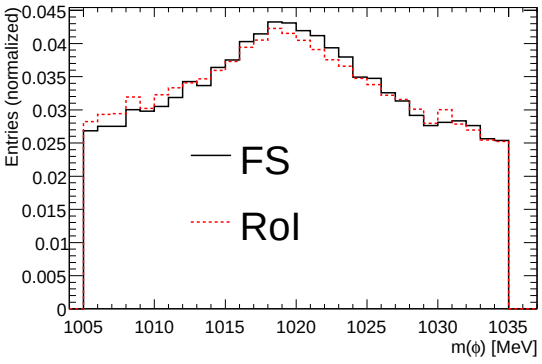

(b) ϕ candidate masses for `BsDsA1mu6`

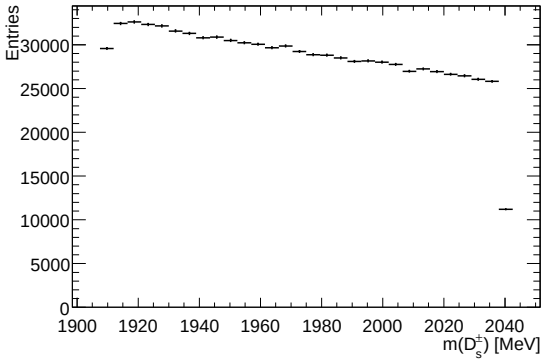

(c) $D_s^{\pm}$ candidate masses for `bbmu6X`

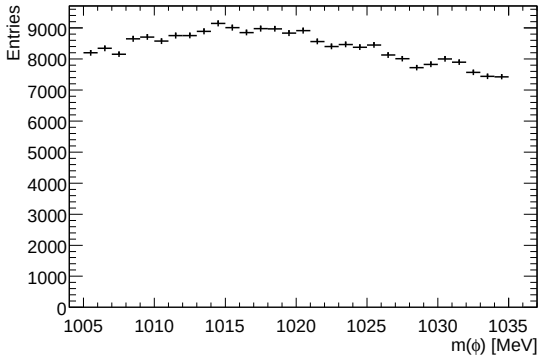

(d) ϕ candidate masses for `bbmu6X`

Figure 9.9: LVL2 particle candidate masses from track fits for the `BsDsA1mu6` and `bbmu6X` datasets. Only the signal dataset allows a discrimination of candidates originating from the FS- or RoI-based algorithms. Therefore, the mass distributions for the `bbmu6X` dataset contain candidates from both algorithms.

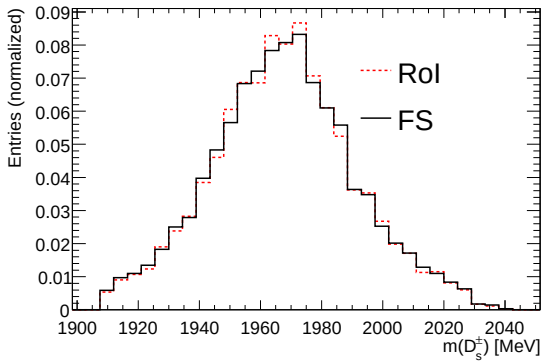

(a) true $D_s^{\pm}$ candidates

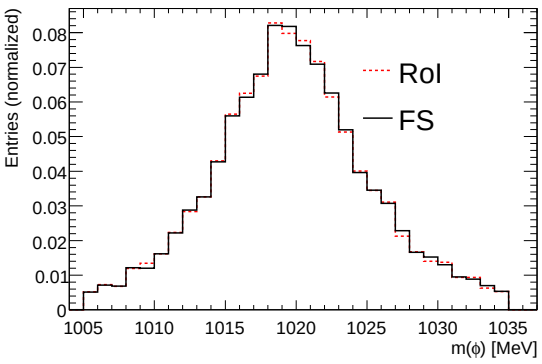

(b) true ϕ candidates

Figure 9.10: LVL2 particle candidate masses from track fits for the truth-matched $D_s^{\pm}$ and ϕ candidates from the `BsDsA1mu6` dataset (normalized with respect to the number of entries), separated by origin (FS or RoI). Only events with a p_T of the B_s^0 meson of 10 GeV or above are considered.

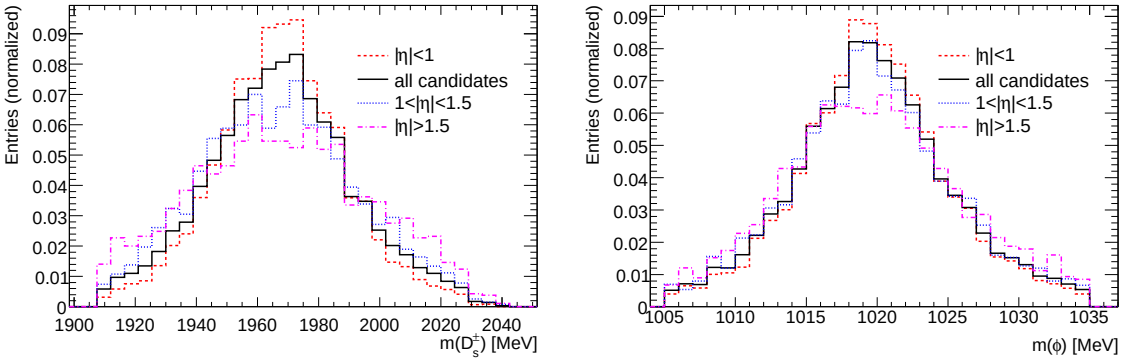

(a) $D_s^{\pm}$ candidates (b) ϕ candidates

Figure 9.11: Normalized distributions (with respect to the number of entries) of the invariant track masses (LVL2 trigger) for $D_s^{\pm}$ and ϕ candidates separated with respect to the pseudorapidity of the B_s^0 meson. Only events from the `BsDsA1mu6` data sample with a p_T of the B_s^0 meson of 10 GeV or above are considered. For both candidate types, the mass resolution decreases with increasing $|\eta|$.

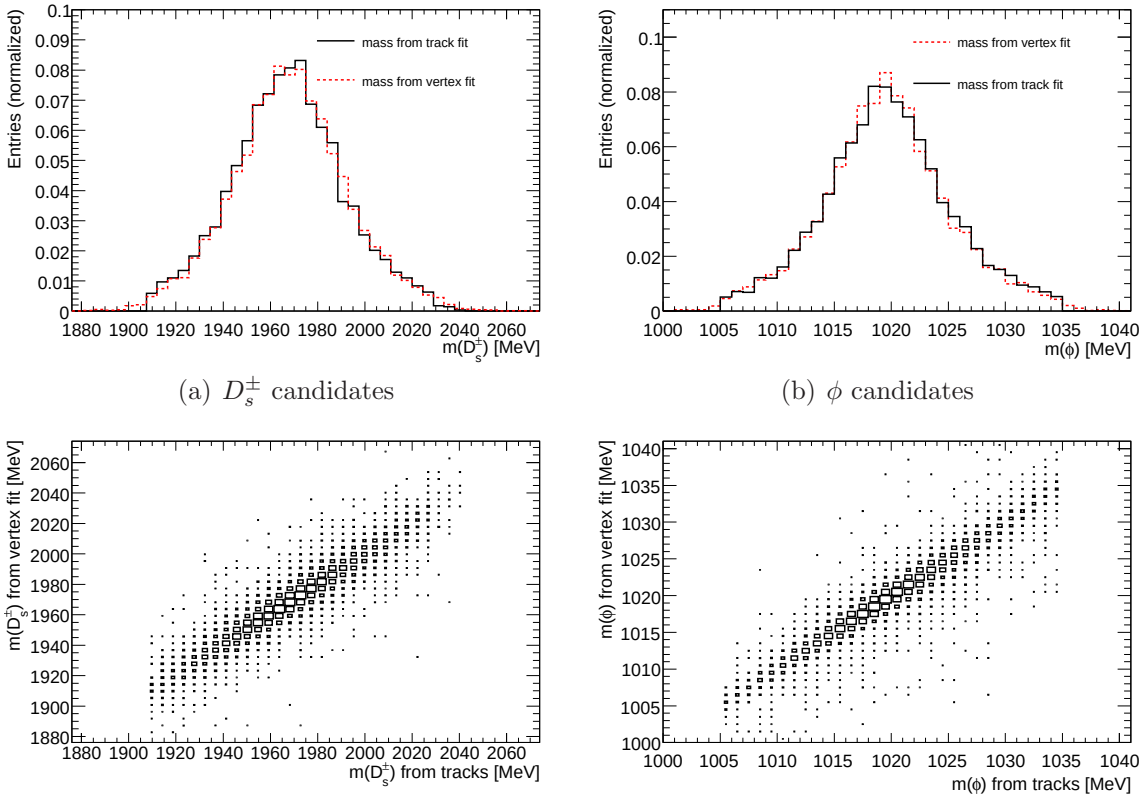

(a) $D_s^{\pm}$ candidates (b) ϕ candidates

(c) correlation for $D_s^{\pm}$ candidates (d) correlation for ϕ candidates

Figure 9.12: Comparison of FS candidate masses from LVL2 track fits and from LVL2 vertex fits for the `BsDsA1mu6` dataset. Only events with a p_T of the B_s^0 meson of 10 GeV or above are considered.

Chapter 10

Event Rate Estimates

From the output of the MC generation jobs, cross-sections and hence event rates are concluded (section 6.1.1). Event rate estimates allow to check two crucial issues:

1. The feasibility of any physics analysis depends on the number of events available for analysis, which is affected by the trigger efficiency for signal events.

2. As described in section 5.2, the overall passing rate of each trigger level is strictly limited. Therefore, the input rates of each trigger level and the rate at which rate events are finally accepted by the event filter (EF) need to be studied.

Both points of interest can only be studied in a limited way within this thesis, as the trigger simulation for the available datasets does not provide decision information of the high-level muon trigger and the EF $D_s^{\mp}$ trigger.
The anticipated luminosity evolution (section 4.1) also affects both aspects, requiring a flexible trigger strategy because of the large cross-section uncertainties (section 2.3): On one hand, event rates will scale with the luminosity provided by the LHC. On the other hand, the detector hit maps of the events will become more complex with increasing luminosity (pileup): For design luminosity, about 23 *pp* interactions per bunch crossing are expected. The effects of pileup are not discussed within this thesis.

10.1 $B_s^0 \to D_s^- a_1^+$ Signal

As the branching ratio for B_s^0 decays to $D_s^- a_1^+$ has not yet been measured, it has to be concluded from the branching ratio of the process $B^0 \to D^- a_1^+$, which requires an estimate of the error associated with the cross-sections for $B_s^0 \to D_s^- a_1^+$ processes [14]:

$$\sigma\left(B_s^0 \to D_s^- a_1^+(\mu 6)\right) = (\ 5.78 \pm 0.03\,(\text{stat.}) \pm 3.22\,(\text{BR}))\,\text{pb}, \tag{10.1}$$
$$\sigma\left(B_s^0 \to D_s^- a_1^+(\mu 4)\right) = (13.64 \pm 0.08\,(\text{stat.}) \pm 7.60\,(\text{BR}))\,\text{pb}. \tag{10.2}$$

The error estimates [14] do not take the uncertainty of the b quark pair production cross-section into account, which is estimated to be a factor of 2 in either direction [16]. The suffix ($\mu 6$) denotes the generation cut (6.4) of 6 GeV, while ($\mu 4$) refers to the generation cut value of 4 GeV and therefore includes $B_s^0 \to D_s^- a_1^+(\mu 6)$ processes. The signal event rate contributions $\left(R\left(B_s^0 \to D_s^- a_1^+\right)\right)$ are very small for LHC luminosities:

$$\mathcal{L} \leq 10^{34}\,\mathrm{cm}^{-2}\mathrm{s}^{-1} \Rightarrow \begin{cases} R\left(B_s^0 \to D_s^- a_1^+(\mu 6)\right) = \mathcal{L} \cdot \sigma\left(B_s^0 \to D_s^- a_1^+(\mu 6)\right) \leq 0.06\,\mathrm{Hz}, \\ R\left(B_s^0 \to D_s^- a_1^+(\mu 4)\right) = \mathcal{L} \cdot \sigma\left(B_s^0 \to D_s^- a_1^+(\mu 4)\right) \leq 0.14\,\mathrm{Hz}. \end{cases}$$

The number of events produced for an integrated luminosity of $\int dt\,\mathcal{L} = 10\,\mathrm{fb}^{-1}$, which corresponds to one year of operation at $\mathcal{L} = 10^{33}\,\mathrm{cm}^{-2}\mathrm{s}^{-1}$, is estimated to be:

$$\begin{aligned} 10\,\mathrm{fb}^{-1} \cdot \sigma\left(B_s^0 \to D_s^- a_1^+(\mu 6)\right) &= (\ 5.78 \pm 0.03\,(\mathrm{stat.}) \pm 3.22\,(\mathrm{BR})) \times 10^4, \\ 10\,\mathrm{fb}^{-1} \cdot \sigma\left(B_s^0 \to D_s^- a_1^+(\mu 4)\right) &= (13.64 \pm 0.08\,(\mathrm{stat.}) \pm 7.60\,(\mathrm{BR})) \times 10^4. \end{aligned}$$

Applying the trigger efficiencies from table 9.1 and the offline selection efficiencies from table A.1 results in the numbers summarized in table 10.1. Note that the event numbers for the $B_s^0 \to D_s^- a_1^+(\mu 4)$ process include those of the $B_s^0 \to D_s^- a_1^+(\mu 6)$ process.
Because of the large uncertainty of the B_s^0 branching ratio and the b quark pair production cross-section, the error on the number of events is dominated by the $B_s^0 \to D_s^- a_1^+$ cross-sections. An estimate of 3500 to 4100 $B_s^0 \to D_s^- a_1^+(\mu 6)$ events for $10\,\mathrm{fb}^{-1}$ is concluded for the trigger strategies listed in table 10.1. For $B_s^0 \to D_s^- a_1^+(\mu 4)$ processes, the expected event numbers range from 5000 to 6800 events per $10\,\mathrm{fb}^{-1}$, as the efficiencies of the trigger strategies vary over a larger range. These numbers do not take LVL2 muon confirmation into account.

10.2 Background Processes

For the background processes, cross-sections of:

$$\sigma\left(b\bar{b} \to \mu 6X\right) = (6.144 \pm 0.016\,(\mathrm{stat.}))\,\mu\mathrm{b} \tag{10.3}$$

for $b\bar{b} \to \mu 6X$ processes,

$$\sigma\left(b\bar{b} \to \mu 4X\right) = (19.1 \pm 0.3\,(\mathrm{stat.}))\,\mu\mathrm{b} \tag{10.4}$$

for $b\bar{b} \to \mu 4X$ processes, and:

$$\sigma\left(c\bar{c} \to \mu 4X\right) = (26.28 \pm 0.09\,(\mathrm{stat.}))\,\mu\mathrm{b} \tag{10.5}$$

for $c\bar{c} \to \mu 4X$ processes are assumed [14,54]. Like for signal processes, the systematic error due to the extrapolation of the b and c quark pair production cross-sections is estimated to be a factor of 2 in either direction.
At the envisaged luminosities for initial LHC running, this corresponds to the contributions to LVL1 and LVL2 rates summarized in tables 10.2 and 10.3.

Table 10.1: Expected event numbers and efficiencies for the LVL2 $D_s^{\mp}$ trigger and the offline analysis for $B_s^0 \to D_s^- a_1^+$ processes. The event numbers refer to an integrated luminosity of $10\,\mathrm{fb}^{-1}$. The uncertainties given for the cross-sections and event numbers do not take the uncertainty on the b quark pair production cross-section into account. Note that no LVL2 muon confirmation has been applied. The efficiencies given in the last column are calculated by multiplying the third and fifth columns.

Dataset	Cross-section number of events	Selection cut passes	Trigger signature	Trigger efficiency for selection cut passes	Reconstructable events passing trigger signature	
`BsDsA1mu6`	(6 ± 3) pb $(6 \pm 3) \times 10^4$	$(8.82 \pm 0.13)\%$	`FS&&MU00+`	$(79.8 \pm 0.6)\%$	4068	$(7.04 \pm 0.12)\%$
			`FS&&MU05+`	$(76.1 \pm 0.6)\%$	3880	$(6.71 \pm 0.11)\%$
			`FS&&MU06+`	$(75.5 \pm 0.6)\%$	3849	$(6.66 \pm 0.11)\%$
			`RoI&&MU00+`	$(72.8 \pm 0.7)\%$	3711	$(6.42 \pm 0.11)\%$
			`RoI&&MU05+`	$(69.5 \pm 0.7)\%$	3543	$(6.13 \pm 0.11)\%$
			`RoI&&MU06+`	$(68.9 \pm 0.7)\%$	3512	$(6.08 \pm 0.11)\%$
`BsDsA1mu4`	(14 ± 8) pb $(14 \pm 8) \times 10^4$	$(6.92 \pm 0.11)\%$	`FS&&MU00+`	$(71.9 \pm 0.8)\%$	6787	$(4.98 \pm 0.10)\%$
			`FS&&MU05+`	$(66.0 \pm 0.8)\%$	6230	$(4.57 \pm 0.09)\%$
			`FS&&MU06+`	$(58.6 \pm 0.8)\%$	5531	$(4.06 \pm 0.09)\%$
			`RoI&&MU00+`	$(64.0 \pm 0.8)\%$	6040	$(4.43 \pm 0.09)\%$
			`RoI&&MU05+`	$(58.8 \pm 0.8)\%$	5550	$(4.07 \pm 0.09)\%$
			`RoI&&MU06+`	$(52.5 \pm 0.8)\%$	4955	$(3.63 \pm 0.08)\%$

Table 10.2: Trigger rate contributions from $b\bar{b} \to \mu X$ processes. Note that no LVL2 muon confirmation has been applied.

$b\bar{b} \to \mu 6X$	
	$\mathcal{L} = 10^{32}\,\mathrm{cm}^{-2}\mathrm{s}^{-1}$
MU00+ rate (Hz)	530
MU05+ rate (Hz)	500
MU06+ rate (Hz)	500
FS&&MU00+ rate (Hz)	23
FS&&MU05+ rate (Hz)	22
FS&&MU06+ rate (Hz)	22
RoI&&MU00+ rate (Hz)	21
RoI&&MU05+ rate (Hz)	20
RoI&&MU06+ rate (Hz)	20
$b\bar{b} \to \mu 4X$	
	$\mathcal{L} = 10^{32}\,\mathrm{cm}^{-2}\mathrm{s}^{-1}$
MU00+ rate (Hz)	1360
MU05+ rate (Hz)	1210
MU06+ rate (Hz)	990
FS&&MU00+ rate (Hz)	40
FS&&MU05+ rate (Hz)	36
FS&&MU06+ rate (Hz)	32
RoI&&MU00+ rate (Hz)	34
RoI&&MU05+ rate (Hz)	32
RoI&&MU06+ rate (Hz)	29

Table 10.3: Trigger rate contributions from $c\bar{c} \to \mu X$ processes. Note that no LVL2 muon confirmation has been applied.

$c\bar{c} \to \mu 4X$	
	$\mathcal{L} = 10^{32}\,\mathrm{cm}^{-2}\mathrm{s}^{-1}$
MU00+ rate (Hz)	1850
MU05+ rate (Hz)	1630
MU06+ rate (Hz)	1330
FS&&MU00+ rate (Hz)	74
FS&&MU05+ rate (Hz)	66
FS&&MU06+ rate (Hz)	58
RoI&&MU00+ rate (Hz)	64
RoI&&MU05+ rate (Hz)	58
RoI&&MU06+ rate (Hz)	51

Table 10.4: Trigger rate contributions from decays of pions and kaons in flight. The same acceptances as for the `bbmu4X` dataset are assumed for the LVL1 muon trigger. Note that no LVL2 muon confirmation has been applied. The jet trigger efficiencies are taken from the RoI multiplicity distributions (figure 9.8).

Decays in flight	
	$\mathcal{L} = 10^{32}\,\mathrm{cm}^{-2}\mathrm{s}^{-1}$
`MU00+` rate (Hz)	1940
`MU05+` rate (Hz)	1710
`MU06+` rate (Hz)	1410
`JT04&&MU00+` rate (Hz)	1810
`JT04&&MU05+` rate (Hz)	1600
`JT04&&MU06+` rate (Hz)	1320
`JT05&&MU00+` rate (Hz)	1340
`JT05&&MU05+` rate (Hz)	1190
`JT05&&MU06+` rate (Hz)	980
`JT06&&MU00+` rate (Hz)	880
`JT06&&MU05+` rate (Hz)	780
`JT06&&MU06+` rate (Hz)	640

Despite the rejection of background events, the resulting LVL2 accept rates are still several orders of magnitude higher than the contribution of signal events. In order to save computing time of the high-level trigger (HLT), a muon confirmation by the LVL2 trigger will be necessary to reduce event filter (EF) seeding rates. For the EF, another iteration of the muon confirmation is foreseen.
The full scan (FS) trigger may be seeded by any process with muons of sufficient p_T in the final state. Hence, decays of charged pions [4]:

$$\pi^+ \to \mu^+\nu_\mu \qquad \text{branching ratio: } (99.98770 \pm 0.00004)\,\%$$

and decays of charged kaons [4]:

$$K^+ \to \mu^+\nu_\mu \qquad \text{branching ratio: } (63.44 \pm 0.14)\,\%$$

also contribute to the LVL1 muon trigger rate (table 10.4). The cross-sections for decays in flight are [54]:

$$\sigma(pp \to \mu 6X) = 4.4\,\mu\mathrm{b},$$
$$\sigma(pp \to \mu 4X) = 27\,\mu\mathrm{b}.$$

As no detailed study of the LVL1 muon trigger acceptance for decays in flight is available, the same acceptances as for $b\bar{b} \to \mu 4X$ processes are assumed. This assumption is equivalent to requiring the resulting muon to point to the interaction point, within the spacial resolution of the LVL1 muon trigger, and to assuming similar p_T spectra for the muons from both processes. These studies therefore constitute a conservative estimate.

Rate contributions for the LVL2 trigger rates are not given, as they are assumed to be negligible: Decays in flight are expected to be at least as efficiently rejected by the LVL2 $D_s^{\mp}$ trigger as $b\bar{b} \to \mu X$ and $c\bar{c} \to \mu X$ processes. Muons from decays in flight are assumed to originate mostly from secondary vertices significantly separated from the primary vertex. Hence, as inner detector data is used during LVL2 muon confirmation, an efficient rejection of decays is assumed for the LVL2 trigger.
For seeding the RoI-based LVL2 trigger, an additional jet RoI is required. Because there is no study available concerning the share of minimum bias events with jet RoIs, it is assumed that the same share of events with muonic decays in flight possess jet RoIs as the $b\bar{b} \to \mu X$ processes, with a mean RoI multiplicity of one. This assumption yields an upper bound for the contribution of decays in flight to the computing time (section 11.3).

Chapter 11

High-Level Trigger Computing Time Requirements

As concluded in chapter 10, the LVL2 trigger is predominantly initiated (seeded) by background processes. In order to estimate the high-level trigger (HLT) computing time required by the LVL2 $D_s^{\mp}$ trigger, the `bbmu6X` sample has been used. Separate runs for the algorithms using regions of interest (RoIs) and a full scan (FS), respectively, have been performed to allow a separation of the results.

11.1 Timing Measurements on a Workstation

The monitoring tools for timing measurements record four contributions of `TrigIDSCAN` algorithms to the track reconstruction times $t_{\mathrm{FS,RoI}}$ [50]:

1. The `SpacePointReader` (SPR) algorithm reads space point data from hits within the silicon trackers.

2. The `IDScanZFinder` (ZF) algorithm reconstructs the z-component of the primary vertex position [55].

3. The `HitFilter` (HF) algorithm performs a pattern recognition on the space points from silicon tracking hits to reconstruct a track from silicon tracker data [56].

4. The resulting track is extrapolated into the TRT in order to identify signal hits in the TRT. The `TrigTRT_TrackExtensionTool` (TRT-TET) associates TRT data to a given track, using a probabilistic data association filter [57].

Using raw data object files (section 6.1.3) for 2000 events from the `bbmu6X` dataset, a byte stream file is created to simulate data flow from the detector. On the byte stream file, the Athena-based algorithms required by the HLT are executed (section 7.2.3).
By processing 2000 events with CPU time monitoring [50], timing information for 1906 RoIs and 301 events processed by the FS algorithm were extracted. The trigger monitoring code in Athena release 12 cannot evaluate data from more than

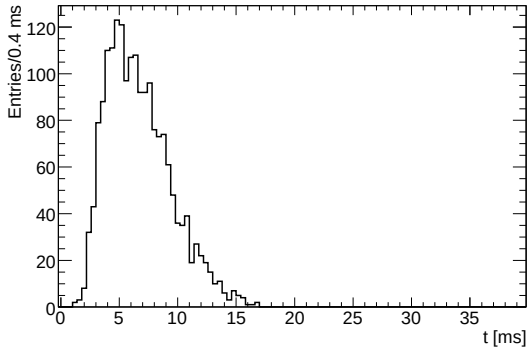

(a) `SpacePointReader`

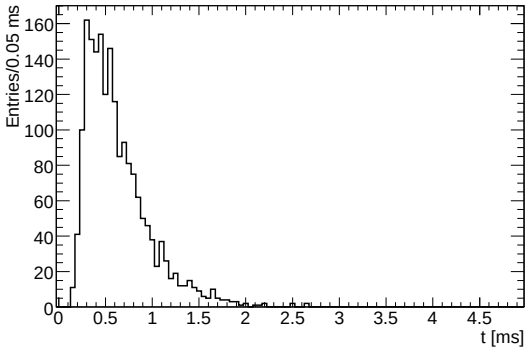

(b) `IDScanZFinder`

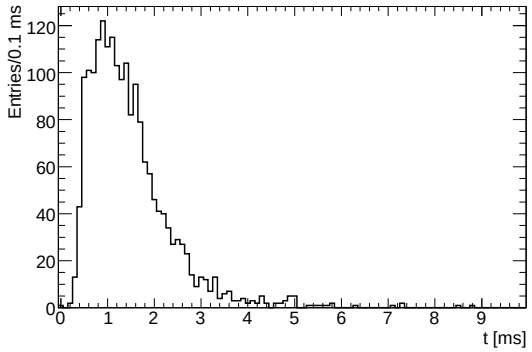

(c) `HitFilter`

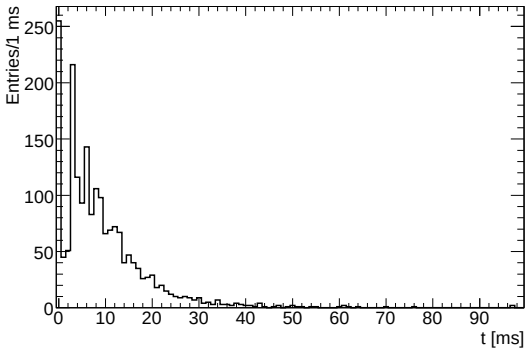

(d) `TrigTRT_TrackExtensionTool`

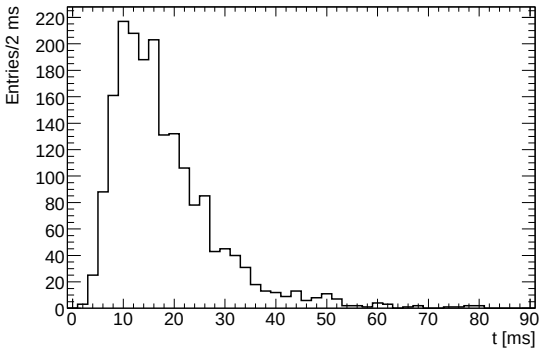

(e) total time IDSCAN

Figure 11.1: Contributions to the LVL2 CPU time requirement on a 3 GHz workstation per RoI — RoI-guided approach. The `TRT-TET` algorithm was not called for 183 events.

Table 11.1: Contributions to the LVL2 CPU time requirement on a 3 GHz workstation per RoI — RoI-guided approach.

Contribution	Mean of $t_{\mathrm{RoI}}^{\mathrm{workstation}}$ [ms]	RMS of $t_{\mathrm{RoI}}^{\mathrm{workstation}}$ [ms]
SPR	6.72 ± 0.06	2.75 ± 0.04
ZF	0.633 ± 0.008	0.349 ± 0.006
HF	1.48 ± 0.02	0.917 ± 0.015
TRT-TET	9.3 ± 0.2	9.57 ± 0.15
Total time IDSCAN	18.2 ± 0.3	11.00 ± 0.18

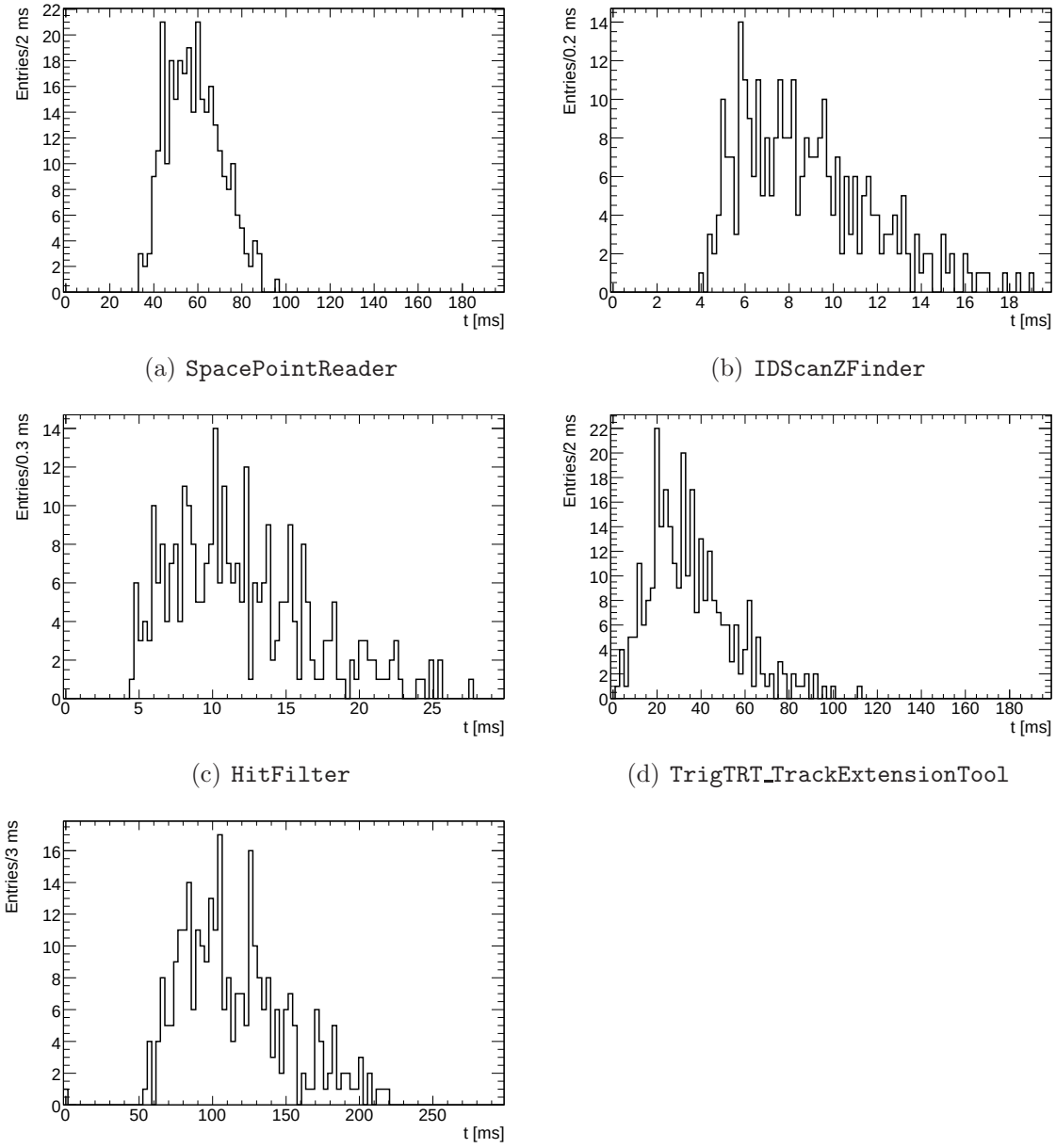

(a) `SpacePointReader` (b) `IDScanZFinder`

(c) `HitFilter` (d) `TrigTRT_TrackExtensionTool`

(e) total time IDSCAN

Figure 11.2: Contributions to the LVL2 CPU time requirement on a 3 GHz workstation per event — FS-guided approach.

Table 11.2: Contributions to the LVL2 CPU time requirement on a 3 GHz workstation per event — FS-guided approach.

Contribution	Mean of $t_{\mathrm{FS}}^{\mathrm{workstation}}$ [ms]	RMS of $t_{\mathrm{FS}}^{\mathrm{tech.\ run}}$ [ms]
SPR	58.6±0.7	12.3±0.5
ZF	8.86±0.17	3.00±0.12
HF	12.0±0.3	4.8±0.2
TRT-TET	35.8±1.1	19.4±0.8
Total time IDSCAN	114.9±2.1	36.5±1.5

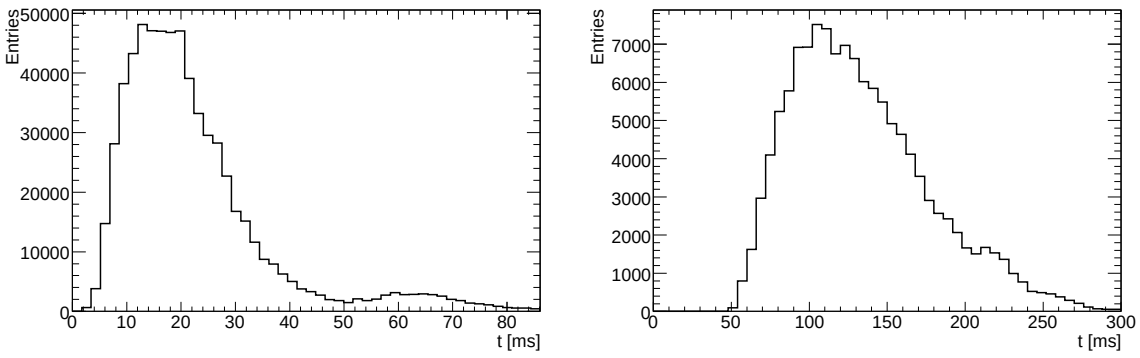

(a) time per RoI (b) time for FS

Figure 11.3: Results for LVL2 CPU time measurements for the total IDSCAN time from the HLT technical run $t_{\mathrm{FS,RoI}}^{\mathrm{tech.\ run}}$ [50].

one RoI per event [50]. Also, the majority of the events seeding the LVL2 FS trigger ($(71.74 \pm 0.14)\,\%$ of the events from the `bbmu6X` dataset fulfill `MU00+`) are not monitored. However, the computing time distributions obtained with Athena release 13 (figure 11.3) [50], for which these limitations have been removed, agree within the systematic uncertainties discussed in section 11.2.
The results from Athena release 12 for the RoI-based trigger approach are summarized in figure 11.1 and table 11.1, those for FS in figure 11.2 and table 11.2.
In both cases, the largest shares of the CPU time are used by the SPR and the TRT-TET. Comparing tables 11.1 and 11.2, the largest relative difference is found for the ZF algorithm, while the TRT algorithm changes most moderately. These different relative changes are attributed to different changes of combinatorics when increasing the number of tracks.
Overall, the RoI-based trigger shows a significantly lower computing time per RoI than the FS algorithm per event. This offers an opportunity to save HLT computing time with little efficiency loss, if the jet RoI threshold is carefully tuned with respect to RoI multiplicity and efficiency for signal events.

11.2 Timing Measurements during Technical Run

For the HLT technical run in November 2007, a trigger simulation for about 134000 $b\bar{b} \to \mu 6X$ events in the byte stream format was performed on ATLAS HLT nodes with 3 GHz LVL2 processing units[1] and Athena release 13 [50]. The FS- and RoI-based algorithms were examined separately. This study allows a more detailed analysis [50] and for checking whether the limitations of the timing analysis with Athena release 12 impose a bias.
The IDSCAN timing information obtained from the technical run for the LVL2 $D_s^{\mp}$ trigger (figure 11.3) is summarized in table 11.3.
For each trigger strategy, the execution times during the technical run were longer

[1] Woodcrest Core architecture

Table 11.3: Results for LVL2 CPU time measurements for the total IDSCAN time from the HLT technical run $t_{\mathrm{FS,RoI}}^{\text{tech. run}}$ [50]. The values for the RoI-based strategy are obtained for seeding by the `JT05` signature and are therefore expected to be larger than the workstation results due to the larger mean number of tracks per RoI.

LVL2 strategy		Mean of $t_{\mathrm{FS,RoI}}^{\text{tech. run}}$ [ms]	$\frac{t_{\mathrm{FS,RoI}}^{\text{tech. run}}}{t_{\mathrm{FS,RoI}}^{\text{workstation}}}$	RMS of $t_{\mathrm{FS,RoI}}^{\text{tech. run}}$ [ms]
RoI	Time per RoI	22.263±0.017	1.22	13.796±0.012
FS	Time per event	133.24±0.13	1.16	44.46±0.09

than for the workstation measurement. The possible technical resons for this include the different Athena version used and a different system performance of the system used for trigger simulation. However, the $b\bar{b} \to \mu 6X$ event topologies are too dissimilar to discern systematic differences in the timing requirements from the 2000 events processed on the workstation. The larger ratio between the results from both runs for the RoI-based trigger than for the FS strategy:

$$\frac{t_{\mathrm{RoI}}^{\text{tech. run}}}{t_{\mathrm{RoI}}^{\text{workstation}}} > \frac{t_{\mathrm{FS}}^{\text{tech. run}}}{t_{\mathrm{FS}}^{\text{workstation}}}$$

are attributed to the use of `JT05` for seeding in the technical run rather than `JT04`, which results in an increase of the mean number of tracks per RoI.
For Athena release 13, the LVL2 timing studies have been extended to monitor the feature extraction (FEX) algorithm. While a mean FEX execution time value of (0.2407 ± 0.0011) ms and an RMS of (0.3925 ± 0.0008) ms could be obtained for the FS approach, the monitoring histograms were improperly set up for probing the FEX execution time of the RoI strategy [50]. Due to the smaller detector region considered, it is assumed that the CPU time used by the FEX algorithm is lower for the RoI-based trigger than for FS and negligible compared to the IDSCAN computing time.

11.3 Computing Time Estimate for Background Processes

Assuming similar HLT computing time requirements for decays in flight, $b\bar{b} \to \mu 4X$, and $c\bar{c} \to \mu 4X$ background processes as obtained for $b\bar{b} \to \mu 6X$ from the technical run, the event rate estimates (section 10.2) are used to evaluate the number of necessary LVL2 processing units (L2PUs) for the LVL2 $D_s^{\mp}$ trigger (section 11.4). The contribution of pions and kaons decaying to muons in flight can only be assessed qualitatively: For the FS trigger, they are assigned the same LVL1 trigger acceptance as $b\bar{b} \to \mu 4X$ processes in order to provide a conservative estimate. For the RoI-based trigger, which is seeded by the combination of a LVL1 jet trigger RoI and `MU0X+`, the estimate is also based on `bbmu4X`: The same LVL1 jet trigger acceptances (obtained from the RoI multiplicity distribution in figure 9.8(a)) are used, assuming one RoI per passing event. Applying the muon trigger efficiencies from table 9.1

leads to RoI seeding rates, which are then multiplied by the average computing time per JT05 RoI.
The resulting seeding rates and HLT computing time requirements for a luminosity of $\mathcal{L} = 10^{32}\,\mathrm{cm}^{-2}\mathrm{s}^{-1}$ are summarized in table 11.4. The LVL1 and LVL2 rates for the $b\bar{b} \to \mu 4X$ and $c\bar{c} \to \mu 4X$ processes are taken from tables 10.2 and 10.3. The LVL1 rate estimates use the cross-sections for background processes [54] and the trigger efficiencies obtained from the bbmu4X dataset for decays in flight.
The initial HLT setup will provide 2232 LVL2 processing units [37] for all LVL2 trigger signatures and will be extended in the future within the limitations imposed by computing rack space and costs. These boundary conditions disallow a simple scaling of the HLT capacity proportional to the luminosity, but demand changes of the trigger menu at each anticipated luminosity stage (cited in section 4.1 [16]).
Therefore, at a luminosity of $\mathcal{L} = 10^{32}\,\mathrm{cm}^{-2}\mathrm{s}^{-1}$, a change from FS to an RoI-based strategy has to be considered, to save HLT computing time. As pileup is still a minor effect at this luminosity, the impact of pileup could then be examined separately from the change from FS to an RoI-guided trigger approach.
The RoI-based LVL2 trigger also offers the jet RoI energy threshold as a parameter for adjusting the LVL2 seeding rate. As shown in section 9.2, the RoI multiplicities are anticorrelated to the threshold energy. Increasing the RoI energy threshold therefore results in lower seeding rates for the RoI-based LVL2 strategies and reduced HLT computing time requirements. Table 9.3 shows upper bounds for the resulting LVL1 trigger efficiencies. As stated in section 9.2, it should be studied how the RoIs containing the $D_s^{\mp}$ decays are affected by changing the RoI threshold relative to the JT0X+ efficiencies. Such a study is indispensable for assessing LVL2 efficiencies for other jet RoI energy thresholds.
The current RoI energy threshold was chosen on the basis of earlier RoI multiplicity evaluations. For these evaluations, $b\bar{b} \to \mu 6X$ data generated with Athena release 9.0.4 and reconstructed with Athena release 10.0.6, leading to a LVL2 computing time of 23 ms per RoI, were used. The value obtained for the mean RoI multiplicity of 1.8 led to an estimate of 44 ms per event for seeding by JT04 [58]. This is considerably lower than 63 ms per event, which is the value obtained for the current bbmu4X dataset and corresponds to approximately the values now expected per event for JT05 (29 ms for bbmu4X and 37 ms for ccmu4X). This trigger item will be used for RoI seeding of the LVL2 $D_s^{\mp}$ trigger as of Athena release 13. The computing times shown in table 11.4 have been calculated using the results of the study with JT05 seeding (table 11.3).
Based on these results, table 12.2 summarizes a preliminary trigger strategy for luminosities up to $\mathcal{L} = 10^{32}\,\mathrm{cm}^{-2}\mathrm{s}^{-1}$ (not taking into account the LVL2 muon confirmation and the EF).

Table 11.4: Dependence of LVL2 computing time requirements on the trigger strategy ($\mathcal{L} = 10^{32}\,\mathrm{cm}^{-2}\mathrm{s}^{-1}$). The number of simultaneously occupied LVL2 processing units is obtained by multiplying the event rate and the mean CPU time required per event or RoI by the LVL2 $D_s^{\mp}$ trigger (table 11.3 [50]). For the RoI-based trigger, the result is multiplied by the RoI multiplicity for the seeding signature `JT04`/`JT05`/`JT06`. Note that no efficiencies for the RoI signatures seeded by `JT05` or `JT06` are available. The `JT04` trigger efficiency has been assumed to be 100 %. This allows using the overall RoI multiplicities for computing time calculations rather than the multiplicities for events containing at least one RoI.

Strategy	Process	LVL1 accept rate [kHz]	L2PUs required *initial HLT setup: 2232 L2PUs*
`FS&&MU00+`	$b\bar{b} \to \mu 4X$	1.36	181
	$c\bar{c} \to \mu 4X$	1.85	246
	decays in flight	1.94	258
			} 685
`FS&&MU05+`	$b\bar{b} \to \mu 4X$	1.21	161
	$c\bar{c} \to \mu 4X$	1.63	217
	decays in flight	1.71	228
			} 606
`FS&&MU06+`	$b\bar{b} \to \mu 4X$	0.99	132
	$c\bar{c} \to \mu 4X$	1.33	177
	decays in flight	1.41	188
			} 497
`RoI&&MU00+`	$b\bar{b} \to \mu 4X$	1.36	86/39/21
	$c\bar{c} \to \mu 4X$	1.85	133/68/41
	decays in flight	1.81/1.34/0.88	40/30/20
			} 259/137/82
`RoI&&MU05+`	$b\bar{b} \to \mu 4X$	1.21	77/35/19
	$c\bar{c} \to \mu 4X$	1.63	117/60/36
	decays in flight	1.60/1.19/0.78	36/26/17
			} 230/121/72
`RoI&&MU06+`	$b\bar{b} \to \mu 4X$	0.99	63/29/15
	$c\bar{c} \to \mu 4X$	1.33	96/49/30
	decays in flight	1.32/0.98/0.64	29/22/14
			} 188/100/59

Chapter 12

Conclusions and Outlook

Part IV of this thesis has demonstrated the capability of the B-trigger to select $B_s^0 \to D_s^- a_1^+$ decays for an observation of B_s^0 oscillations.
As the mixing analysis requires flavor tagging, the first-level (LVL1) trigger selects events with muons. As the transverse momentum spectra of the muons from the signal processes fall with higher p_T, the p_T threshold applied is highly relevant for the selection efficiency. The ATLAS LVL1 muon trigger provides significant acceptance only for muons above a p_T value of 4 GeV. For this reason, only $B_s^0 \to D_s^- a_1^+$ decays with p_T values of the tagging muon above 4 GeV contribute to the analysis. For these events, the LVL1 muon trigger achieves the efficiencies ϵ in dependence of the threshold setting. For the low-p_T muon trigger menu envisaged for initial running, the LVL1 muon trigger selects the following shares of the $B_s^0 \to D_s^- a_1^+(\mu 4)$ events contributing to the mixing analysis:

$$\begin{aligned}
\epsilon(\text{LVL1 } \mu(4\,\text{GeV}) &= (75.65 \pm 0.19\,(\text{stat.}))\,\%,\\
\epsilon(\text{LVL1 } \mu(5\,\text{GeV}) &= (68.4 \pm 0.2\,(\text{stat.}))\,\%,\\
\epsilon(\text{LVL1 } \mu(6\,\text{GeV}) &= (58.9 \pm 0.2\,(\text{stat.}))\,\%.
\end{aligned}$$

The events failing the LVL1 muon trigger are concentrated in several areas of inefficiency, which are caused by the geometric design of the muon trigger chambers.
In order to separate the signal events from background processes containing muons, the ATLAS high-level trigger (HLT) features track reconstruction capabilities, which are used for reconstructing $D_s^{\mp}$ candidates from detector tracks of the inner detector. Therefore, the HLT trigger item is used both for selecting hadronic B_s^0 decays following $B_s^0 \to D_s^- a_1^+$ as well as the channel $B_s^0 \to D_s^- \pi^+$. The selection is based on invariant mass values that are attributed to the reconstructed tracks by applying particle hypotheses.
Because a full scan of the tracks from the inner detector consumes more computing power than the HLT can provide (except for very low event rates), the LVL2 trigger provides a signature that only reconstructs a portion of the inner detector. This region of interest is distinguished by the LVL1 trigger by geometric association to an energy deposit within the hadronic calorimeter. Restricting the particle candidate reconstruction to a part of the inner detector reduces the average computing time required by the LVL2 trigger per event (t_{event}). The reduction may be tuned by

changing the jet region of interest (RoI) energy threshold (numbers for $b\bar{b} \to \mu 4X$ background processes):

$$\begin{aligned} t_{\text{event}}^{\text{full scan}} &= (133.24 \pm 0.13\,(\text{stat.}))\,\text{ms}, \\ t_{\text{event}}^{\text{RoI,4 GeV}} &= (63.4 \pm 0.05\,(\text{stat.}))\,\text{ms}, \\ t_{\text{event}}^{\text{RoI,5 GeV}} &= (29.0 \pm 0.02\,(\text{stat.}))\,\text{ms}. \end{aligned}$$

The efficiency difference between the approaches based on a full scan (FS) or on RoIs is especially large for events with a low p_T of the B_s^0 meson. As the kinematic distributions for signal events are dominated by events of low p_T, the overall efficiencies for the FS- and RoI-based algorithms differ significantly:

$$\begin{aligned} \epsilon^{\text{signal}}(\text{LVL2 FS \&\& LVL1 } \mu(6\,\text{GeV})) &= (19.13 \pm 0.19\,(\text{stat.}))\,\%, \\ \epsilon^{\text{signal}}(\text{LVL2 RoI \&\& LVL1 } \mu(6\,\text{GeV})) &= (16.10 \pm 0.18\,(\text{stat.}))\,\%. \end{aligned}$$

The according acceptances for $b\bar{b} \to \mu 4X$ background events are:

$$\begin{aligned} \epsilon^{\text{bg}}(\text{LVL2 FS \&\& LVL1 } \mu(6\,\text{GeV})) &= (1.71 \pm 0.04\,(\text{stat.}))\,\%, \\ \epsilon^{\text{bg}}(\text{LVL2 RoI \&\& LVL1 } \mu(6\,\text{GeV})) &= (1.50 \pm 0.04\,(\text{stat.}))\,\%. \end{aligned}$$

For an estimate of the numbers of events available for a mixing analysis, the efficiencies for signal events passing the offline data analysis is relevant:

$$\begin{aligned} \epsilon^{\text{offl. pass}}(\text{LVL2 FS \&\& LVL1 } \mu(6\,\text{GeV})) &= (75.5 \pm 0.6\,(\text{stat.}))\,\%, \\ \epsilon^{\text{offl. pass}}(\text{LVL2 RoI \&\& LVL1 } \mu(6\,\text{GeV})) &= (68.9 \pm 0.7\,(\text{stat.}))\,\%. \end{aligned}$$

Thus, the $D_s^{\mp}$ trigger is more efficient for events that pass the offline selection cuts than for other signal events. These events correspond to $(6.92 \pm 0.11)\,\%$ of the $B_s^0 \to D_s^- a_1^+(\mu 4)$ processes.
By concluding a branching ratio for $B_s^0 \to D_s^- a_1^+$ decays from B^0 values, the total number of $B_s^0 \to D_s^- a_1^+(\mu 4)$ events produced for an integrated luminosity of $10\,\text{fb}^{-1}$ is $(14 \pm 8) \times 10^4$ ($(9 \pm 5) \times 10^3$ reconstructable events) with an additional uncertainty factor of 2 in either direction from the b quark pair production cross-section.
These event numbers require an efficient event selection by the trigger system. The trigger strategies summarized in table 12.1 accept about 5000 to 6800 events per $10\,\text{fb}^{-1}$ (with similar uncertainties as the number of events). Table 12.1 also supplies an estimate how the LVL2 $D_s^{\mp}$ trigger contributes to the EF seeding rate, i.e., the rate at which the event filter (EF) $D_s^{\mp}$ trigger algorithm is initiated. The contribution of decays in flight to the event filter (EF) seeding rate is neglected. Even if the $D_s^{\mp}$ trigger finds a suitable $D_s^{\mp}$ candidate, the event is likely to be rejected by the LVL2 muon confirmation, as inner detector data is used to resolve the track irregularity caused by the decay.

Table 12.1: Dependence of LVL2 computing time requirements and LVL2 output rate on the trigger strategy ($\mathcal{L} = 10^{32}\,\mathrm{cm}^{-2}\mathrm{s}^{-1}$). The LVL2 trigger acceptance of background events containing decays in flight is neglected. The number of simultaneously occupied LVL2 processing units is obtained by multiplying the event rate and the mean CPU time required per event or RoI by the LVL2 $D_s^{\mp}$ trigger (table 11.3 [50]). For the RoI-based trigger, the result is multiplied by the RoI multiplicity for the seeding signature `JT04`/`JT05`/`JT06`. Note that no efficiencies for the RoI signatures seeded by `JT05` or `JT06` are available. The efficiencies stated for the RoI trigger are based on the `JT04` jet RoI energy threshold. The `JT04` trigger efficiency has been assumed to be 100 %. This allows using the overall RoI multiplicities for computing time calculations rather than the multiplicities for events containing at least one RoI. Note that the overall efficiency numbers in the last column for `LVL2&&MU0X+` do not take muon confirmation into account.

Strategy	Process	LVL1 accept rate [kHz]	L2PUs required *initial HLT setup: 2232 L2PUs*	LVL2 accept rate [Hz]	Efficiency for $B_s^0 \to D_s^- a_1^+(\mu 4)$ processes [%]
`FS&&MU00+`	$b\bar{b} \to \mu 4X$	1.36	181	40	71.9 ± 0.8
	$c\bar{c} \to \mu 4X$	1.85	246 } 685	74 } 114	
	decays in flight	1.94	258	negligible	
`FS&&MU05+`	$b\bar{b} \to \mu 4X$	1.21	161	36	66.0 ± 0.8
	$c\bar{c} \to \mu 4X$	1.63	217 } 606	66 } 102	
	decays in flight	1.71	228	negligible	
`FS&&MU06+`	$b\bar{b} \to \mu 4X$	0.99	132	32	58.6 ± 0.8
	$c\bar{c} \to \mu 4X$	1.33	177 } 497	58 } 90	
	decays in flight	1.41	188	negligible	
`RoI&&MU00+`	$b\bar{b} \to \mu 4X$	1.36	86/39/21	34	64.0 ± 0.8
	$c\bar{c} \to \mu 4X$	1.85	133/68/41 } 259/137/82	64 } 98	
	decays in flight	1.81/1.34/0.88	40/30/20	negligible	
`RoI&&MU05+`	$b\bar{b} \to \mu 4X$	1.21	77/35/19	32	58.8 ± 0.8
	$c\bar{c} \to \mu 4X$	1.63	117/60/36 } 230/121/72	58 } 90	
	decays in flight	1.60/1.19/0.78	36/26/17	negligible	
`RoI&&MU06+`	$b\bar{b} \to \mu 4X$	0.99	63/29/15	29	52.5 ± 0.8
	$c\bar{c} \to \mu 4X$	1.33	96/49/30 } 188/100/59	51 } 80	
	decays in flight	1.32/0.98/0.64	29/22/14	negligible	

As the $b\bar{b} \rightarrow \mu 4X$ and $c\bar{c} \rightarrow \mu 4X$ background processes do not offer such an easy means of discrimination, the LVL2 output rate will require an increase in background rejection by the LVL1 and/or LVL2 triggers when the luminosity reaches the order $\mathcal{O}(10^{33}\,\mathrm{cm}^{-2}\mathrm{s}^{-1})$. This luminosity would correspond to an accept rate of the LVL2 $D_s^{\mp}$ trigger of several hundreds of Hz at the assumed background rejection. This constitutes a too large fraction of the total LVL2 rate limitation of 2 kHz for all LVL2 trigger signatures. There are several handles to achieve an improvement of the background rejection within the $D_s^{\mp}$ trigger algorithm (chapter 9). If these measures fail to improve background rejection sufficiently, the trigger menu still allows imposing a tighter threshold on the p_T of the muon (LVL1 and/or LVL2) or even prescaling in order to reduce background rates.
The ansatz of raising the thresholds of the low-p_T muon trigger menu could not be fully studied from the available datasets, as re-running event reconstruction with another low-p_T muon trigger menu led to inconsistent results. However, these studies provided strong evidence that the LVL1 muon trigger efficiency decreases more slowly when raising the p_T threshold than the p_T spectra of the muons within the datasets. This would provide options such as requiring a muon with a p_T of at least 8 GeV on LVL1 for early background rejection, but requiring only a p_T of 6 GeV on LVL2 for maintaining a high efficiency for signal events.
Only a few fb^{-1} shall be collected at luminosities below the design luminosity of $\mathcal{L} = 10^{34}\,\mathrm{cm}^{-2}\mathrm{s}^{-1}$. At this luminosity, using HLT signatures initiated by low-p_T single muon trigger signatures is not feasible without prescaling. Therefore, the trigger selection must be as efficient as possible during early data taking, which may be achieved by employing the trigger menu proposed in table 12.2.

Outlook

Further study possibilities include investigating the performance of the HLT muon confirmation and studying trigger rate contributions from decays in flight in more detail. A study of how raising the muon trigger p_T thresholds and the jet RoI energy thresholds affects the analysis is also important. The data from LVL2 vertex fits has so far not been taken into account, either.
For luminosities of the order $\mathcal{O}(10^{33}\,\mathrm{cm}^{-2}\mathrm{s}^{-1})$, additional studies are necessary, because all of the strategies evaluated lead to estimates exceeding both the EF seeding rate and the LVL2 computing time limitations:

- The impact of the HLT muon confirmation could not be taken into account, because the HLT muon confirmation was not properly simulated for the given datasets. A significantly increased rejection of muons below the respective p_T thresholds and of muons from decays in flight is expected.

- The trigger rates and efficiencies for different low-p_T muon trigger thresholds between 6 and 10 GeV should be evaluated. Also, different values for the jet RoI energy threshold should be tested, as changing the threshold alters the

Table 12.2: Proposed trigger menu integration of the LVL2 $D_s^{\mp}$ trigger for luminosities up to $\mathcal{L} = 10^{32}\,\mathrm{cm}^{-2}\mathrm{s}^{-1}$. For initial luminosity, a full scan-based strategy seeded by an open p_T window of the LVL1 muon trigger is proposed. For $\mathcal{L} = 10^{32}\,\mathrm{cm}^{-2}\mathrm{s}^{-1}$, an RoI-based strategy with an RoI energy threshold of 5 GeV and the same muon condition is proposed. Due to the branching ration uncertainty, the event numbers carry a relative error of about 60 % and an additional uncertainty factor of 2 in either direction from the b quark pair production cross-section. The event number estimate for $\mathcal{L} = 10^{32}\,\mathrm{cm}^{-2}\mathrm{s}^{-1}$ uses an upper bound for the `JT05` efficiency. The event numbers given do not take the HLT muon confirmation and the efficiency of the event filter (EF) $D_s^{\mp}$ trigger signature into account.

Luminosity $[\mathrm{cm}^{-2}\mathrm{s}^{-1}]$	Trigger strategy	Number of events per $10\,\mathrm{fb}^{-1}$	Limiting factor
10^{31}	`FS&&MU00+`	6800	B-trigger uses 3 % of HLT computing power (compared to HLT initial setup)
10^{32}	`RoI&&JT05&&MU00+`	∼5000	B-trigger uses 6 % of HLT computing power (compared to HLT initial setup)

HLT computing time requirements by affecting both the seeding rate and the computing time demand per RoI as well as the trigger efficiency.

- A study, whether the χ^2 and invariant mass values obtained from LVL2 vertex fits can improve background rejection and therefore reduce EF seeding rates, should be performed.

- The seeding rate contribution of decays in flight needs to be assessed quantitatively.

Part V

Appendix

Appendix A

Summary of Datasets Used in this Thesis

Table A.1 summarizes the datasets used for analysis within this thesis. The uncertainty values given for the cross-sections do not take the uncertainty on the B_s^0 branching ratio for the $B_s^0 \to D_s^- a_1^+$ decay into account. The relative uncertainty on the branching ratio is assumed to be about 56 % (section 10.1). All cross-sections carry an additional uncertainty of a factor 2 in either direction due to the unknown b and c quark pair production cross-section at LHC energy scales. The cuts on kinematic variables (columns three to five) are described in section 6.1.1.
The signal datasets were produced locally, while the background samples originate from the official Grid production of the ATLAS computing system commissioning (CSC) effort. For the background samples, the `cutbq` selection cuts are applied to a quark or an antiquark of the given flavor (b quarks in all but the $c\bar{c}$ background sample `ccmu4X`). For the signal datasets, the kinematic cuts were applied to both a b quark and a $\bar{b}$ quark.

Table A.1: Summary of the datasets used for analysis. The cross-sections given are obtained from PYTHIA output. The uncertainty given only reflects the statistical error.

Label	Physics process	p_T cut on muon [GeV]	`ckin3`	`cutbq`	Number of events	Origin	Fraction of selection cut passes	Note
`BsDsA1mu6`	$B_s^0 \to D_s^- a_1^+(\mu 6)$ (5.78 ± 0.03) pb [14]	6	10	6 2.5 and 6 2.5	50000	`SiMPLE`	$(8.82 \pm 0.13)\,\%$	cuts (6.7) and (6.6) on final state particles
`BsDsA1mu4`	$B_s^0 \to D_s^- a_1^+(\mu 4)$ (13.64 ± 0.08) pb [14]	4	6	4 2.5 and 4 2.5	50000	`SiMPLE`	$(6.92 \pm 0.11)\,\%$	cuts (6.7) and (6.6) on final state particles
`bbmu6X`	$\bar{b}b \to \mu^{\pm} X$ $(6.144 \pm 0.016)\,\mu$b [15]	6	6	7 4.5 or 7 4.5	242150	Grid	$(6.2^{+\,1.8}_{-\,1.5}) \times 10^{-5}$	
`bbmu4X`	$\bar{b}b \to \mu^{\pm} X$ $(19.1 \pm 0.3)\,\mu$b [14, 54]	4	6	5 4.5 or 5 4.5	98450	Grid	$(5^{+\,3}_{-\,2}) \times 10^{-5}$	
`ccmu4X`	$\bar{c}c \to \mu^{\pm} X$ $(26.28 \pm 0.09)\,\mu$b [14, 54]	4	6	4 4.5 or 4 4.5	44750	Grid	$(2.2^{+\,3.4}_{-\,1.6}) \times 10^{-5}$	

Appendix B

Kinematic Distributions

B.1 $B_s^0 \to D_s^- a_1^+$ Datasets

B.1.1 No Trigger Requirement

Figures B.1 to B.4 show the kinematic distributions of the D_s^- mesons and the final state particles of the signal decay. A comparison of the distributions for the `BsDsA1mu6` and `BsDsA1mu4` datasets shows no significant differences, except for changes of the p_T spectra, which are expected due to different p_T cuts applied during MC generation.

B.1.2 Trigger Effects

Figure B.5 shows that the LVL2 $D_s^\mp$ trigger implementations introduce no significant changes to the η and ϕ distributions of the muons with the highest p_T per event (`BsDsA1mu6` dataset). The areas of reduced trigger efficiencies are caused by the detector feet ($\phi \approx -1, -2$) and by the transition region between barrel and end-caps of the muon trigger system ($\eta \approx \pm 1$). The latter effect is more pronounced for $\eta \approx +1$ because muons of negative charge dominate in the signal datasets. Muons of both charges are affected by the gap of the muon spectrometer at $\eta \approx 0$. The p_T spectra are shifted towards higher values due to the larger reconstruction efficiency for high-p_T events.
Figure B.6 illustrates that the `JT04` trigger signature affects the p_T spectrum of the B_s^0 mesons in the `BsDsA1mu4` data sample significantly by rejecting low-p_T events. The `BsDsA1mu6` is hardly affected due to the higher transverse momenta. The η distributions are not significantly impacted in either dataset.

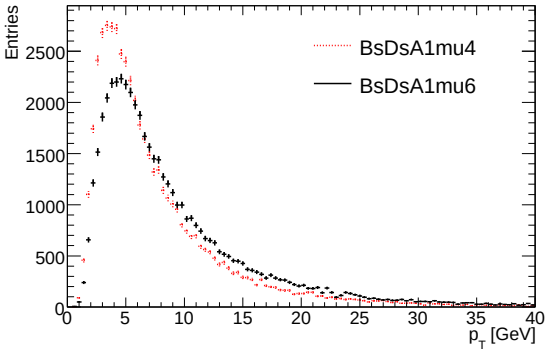

(a) $p_T^{\text{truth}}(D_s^-)$

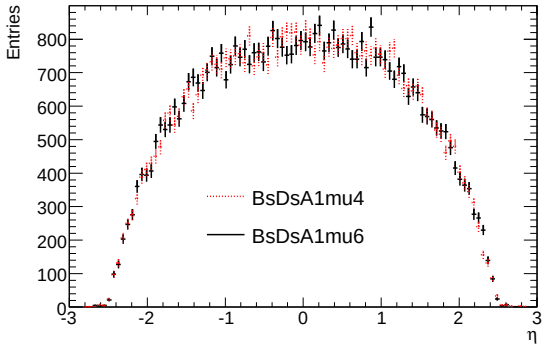

(b) $\eta^{\text{truth}}(D_s^-)$

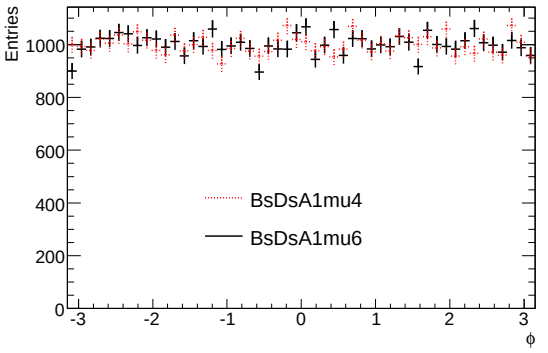

(c) $\phi^{\text{truth}}(D_s^-)$

Figure B.1: Distributions of the kinematic variables of the D_s^- mesons in the `BsDsA1mu6` and `BsDsA1mu4` samples (MC truth).

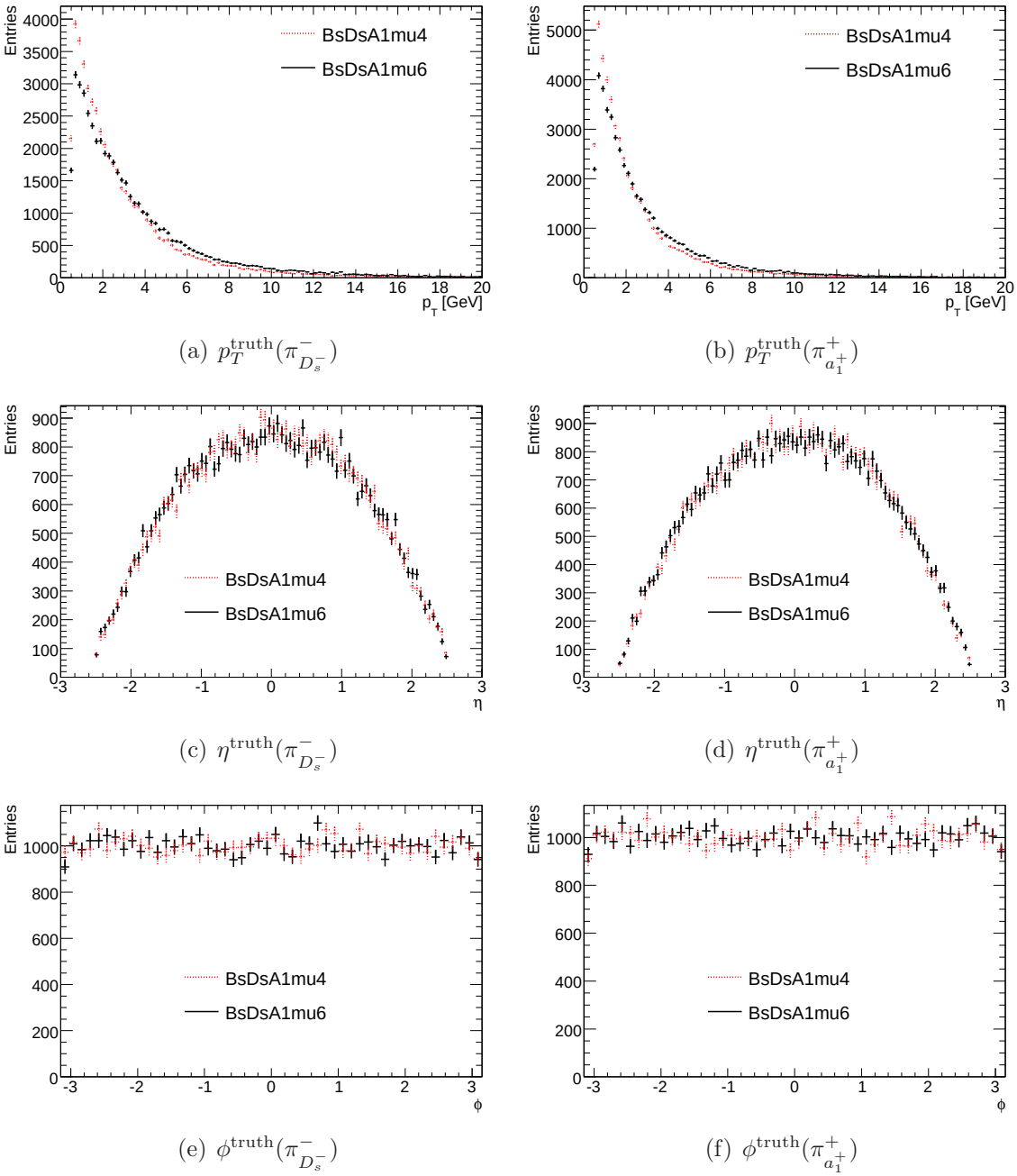

(a) $p_T^{\text{truth}}(\pi^-_{D_s^-})$

(b) $p_T^{\text{truth}}(\pi^+_{a_1^+})$

(c) $\eta^{\text{truth}}(\pi^-_{D_s^-})$

(d) $\eta^{\text{truth}}(\pi^+_{a_1^+})$

(e) $\phi^{\text{truth}}(\pi^-_{D_s^-})$

(f) $\phi^{\text{truth}}(\pi^+_{a_1^+})$

Figure B.2: Distributions of the kinematic variables of the $\pi^{\pm}$ mesons which originate from the D_s^- decay vertex ($\pi^-_{D_s^-}$) and from the a_1^+ meson decay ($\pi^+_{a_1^+}$) from the `BsDsA1mu6` and `BsDsA1mu4` samples (MC truth).

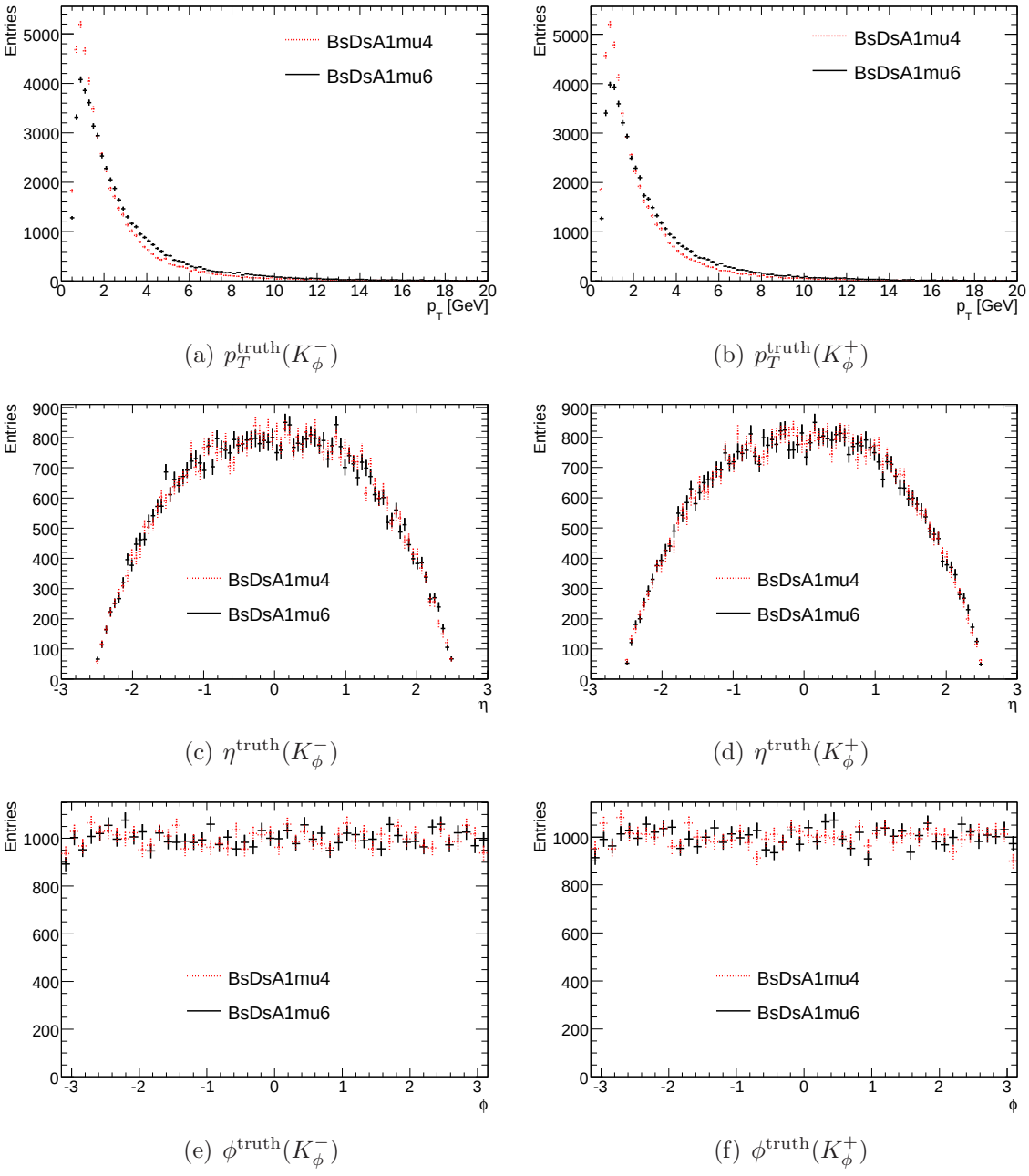

(a) $p_T^{\text{truth}}(K_\phi^-)$ (b) $p_T^{\text{truth}}(K_\phi^+)$

(c) $\eta^{\text{truth}}(K_\phi^-)$ (d) $\eta^{\text{truth}}(K_\phi^+)$

(e) $\phi^{\text{truth}}(K_\phi^-)$ (f) $\phi^{\text{truth}}(K_\phi^+)$

Figure B.3: Distributions of the kinematic variables of the $K^\pm$ mesons which originate from the ϕ particles from the `BsDsA1mu6` and `BsDsA1mu4` samples (MC truth).

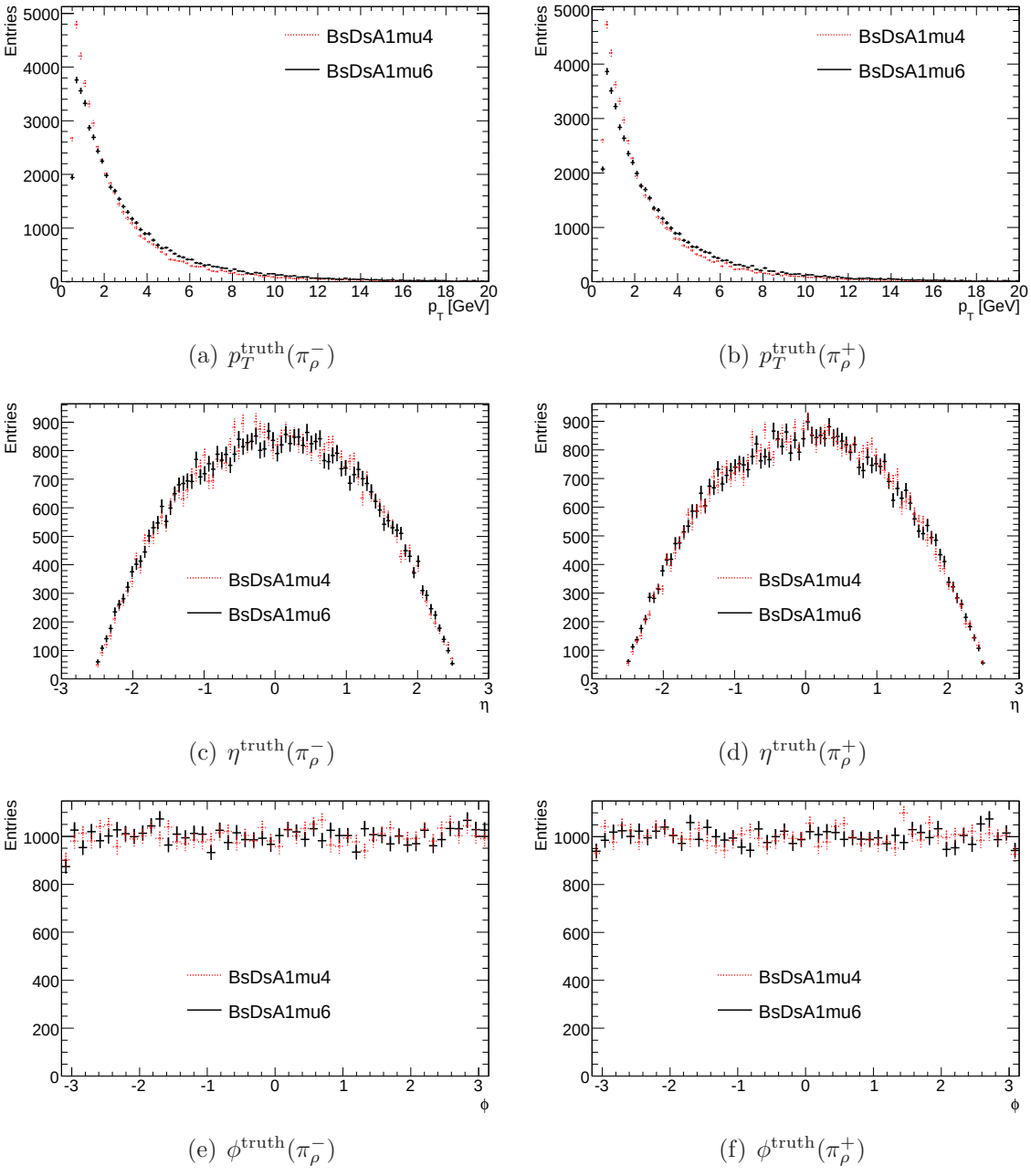

(a) $p_T^{\text{truth}}(\pi_\rho^-)$

(b) $p_T^{\text{truth}}(\pi_\rho^+)$

(c) $\eta^{\text{truth}}(\pi_\rho^-)$

(d) $\eta^{\text{truth}}(\pi_\rho^+)$

(e) $\phi^{\text{truth}}(\pi_\rho^-)$

(f) $\phi^{\text{truth}}(\pi_\rho^+)$

Figure B.4: Distributions of the kinematic variables of the $\pi^\pm$ mesons which originate from the ρ particles from the `BsDsA1mu6` and `BsDsA1mu4` samples (MC truth).

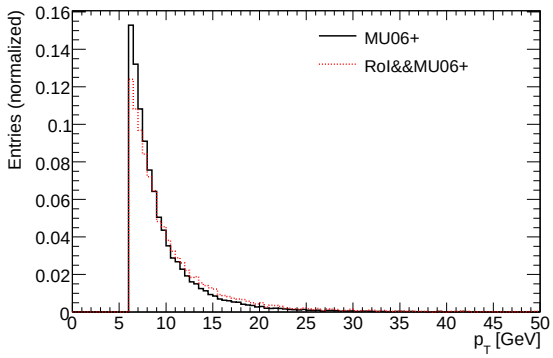

(a) $p_T^{\text{truth}}(\mu_{\text{highest } p_T})$ for `RoI` trigger

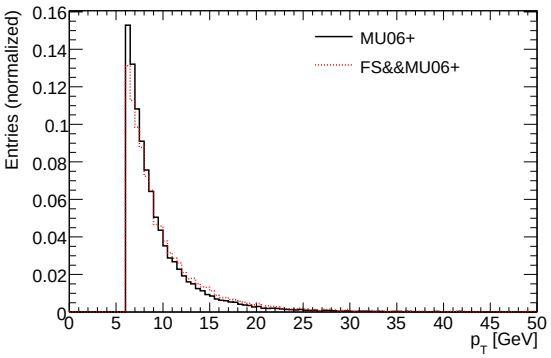

(b) $p_T^{\text{truth}}(\mu_{\text{highest } p_T})$ for `FS` trigger

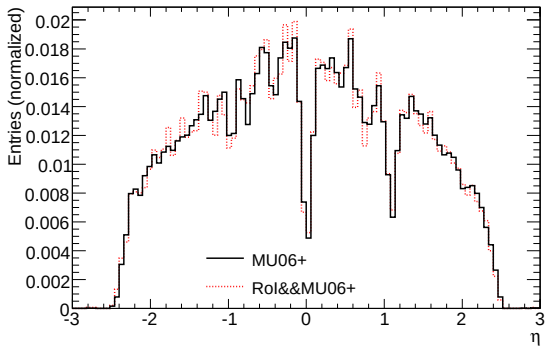

(c) $\eta^{\text{truth}}(\mu_{\text{highest } p_T})$ for `RoI` trigger

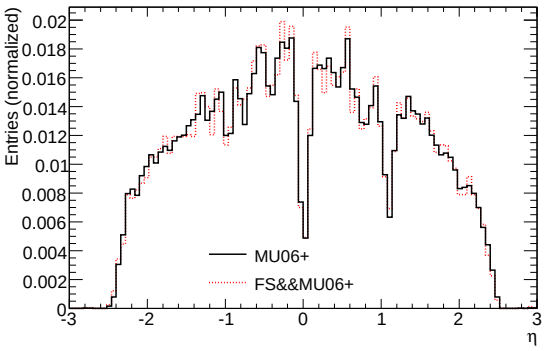

(d) $\eta^{\text{truth}}(\mu_{\text{highest } p_T})$ for `FS` trigger

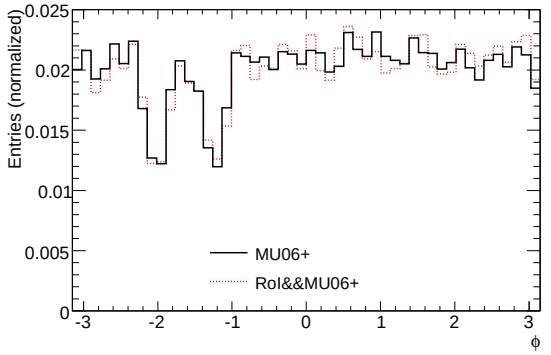

(e) $\phi^{\text{truth}}(\mu_{\text{highest } p_T})$ for `RoI` trigger

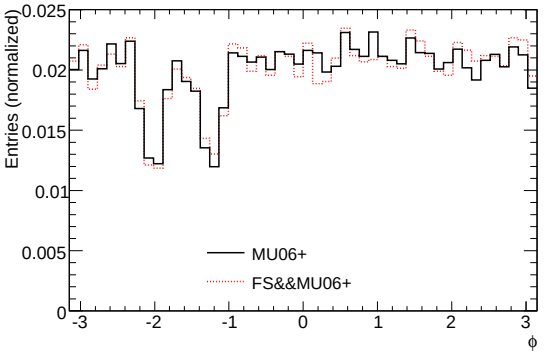

(f) $\phi^{\text{truth}}(\mu_{\text{highest } p_T})$ for `FS` trigger

Figure B.5: Normalized (with respect to the number of entries) distributions of the kinematic variables of $\mu_{\text{highest } p_T}$ in the `BsDsA1mu6` sample (MC truth), comparing events passing `MU06+` and events that also pass `RoI` and `FS`.

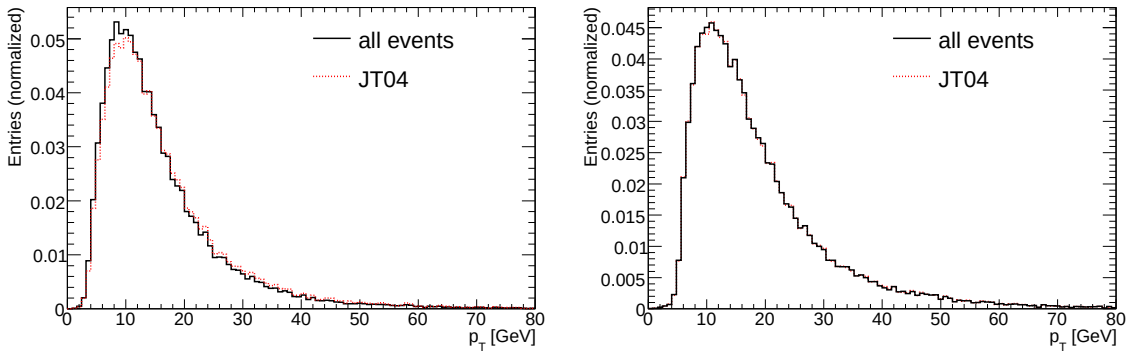

(a) $p_T^{\text{truth}}(B_s^0)$ in `BsDsA1mu4` sample

(b) $p_T^{\text{truth}}(B_s^0)$ in `BsDsA1mu6` sample

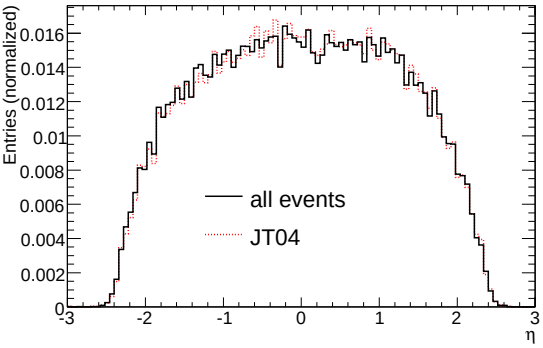

(c) $\eta^{\text{truth}}(B_s^0)$ in `BsDsA1mu4` sample

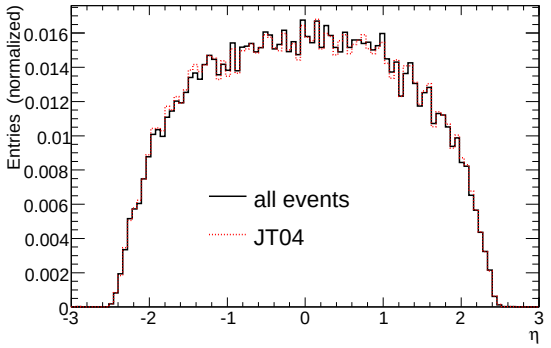

(d) $\eta^{\text{truth}}(B_s^0)$ in `BsDsA1mu6` sample

Figure B.6: p_T and η distributions of the B_s^0 particles in the `BsDsA1mu4` and `BsDsA1mu6` samples (MC truth), taking into account only events passing `JT04` (normalized with respect to the number of entries).

B.2 $b\bar{b} \to \mu X$ Datasets

Figure B.7 compares the kinematic distributions of the muon with the highest p_T per event from the `bbmu6X` and `bbmu4X` datasets. The only significant difference observed is the shift of the p_T distribution, caused by different cuts applied during generation.

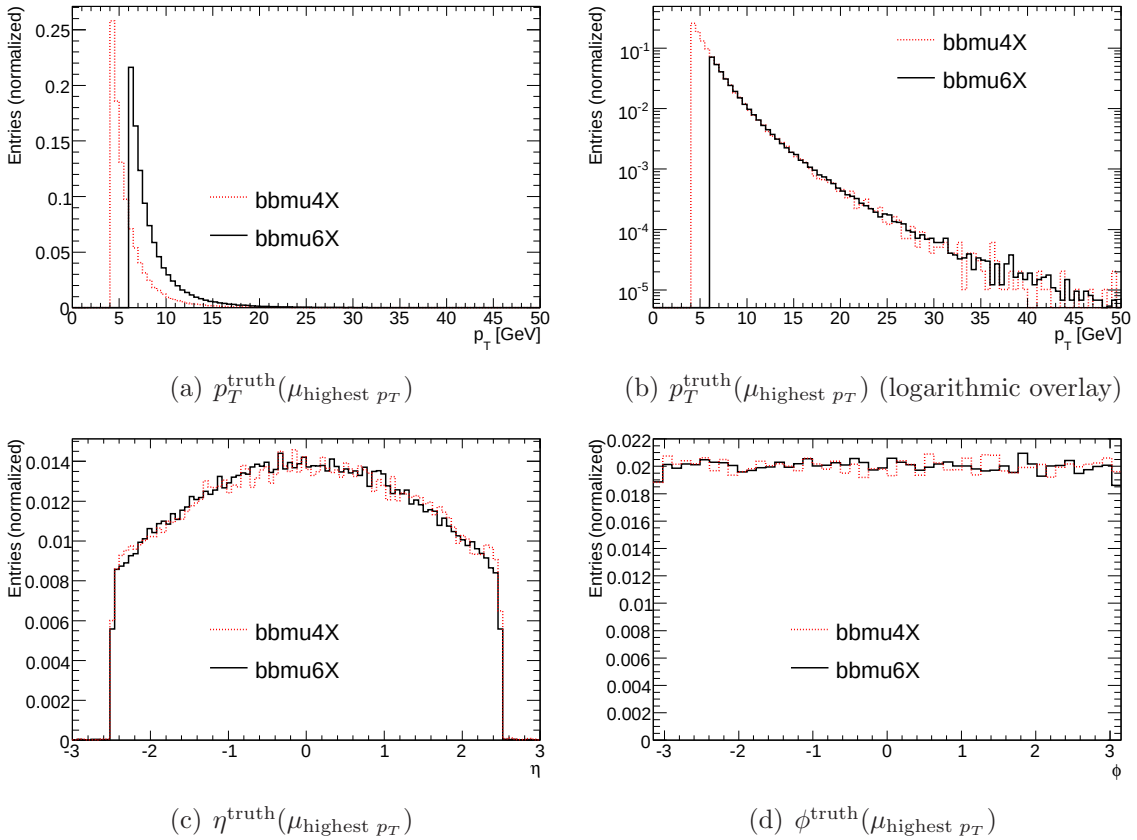

(a) $p_T^{\text{truth}}(\mu_{\text{highest } p_T})$

(b) $p_T^{\text{truth}}(\mu_{\text{highest } p_T})$ (logarithmic overlay)

(c) $\eta^{\text{truth}}(\mu_{\text{highest } p_T})$

(d) $\phi^{\text{truth}}(\mu_{\text{highest } p_T})$

Figure B.7: Normalized distributions (with respect to the number of entries) of the kinematic variables of $\mu_{\text{highest } p_T}$ in the `bbmu6X` and `bbmu4X` samples (MC truth). The normalized $p_T^{\text{truth}}(\mu_{\text{highest } p_T})$ distributions (logarithmic scale) show that the shape of the p_T distribution is unaffected by the generation cuts.

List of Abbreviations and Acronyms

ALICE ..... a large ion collider experiment, page 16
AOD ..... analysis object data, page 30
ATLAS ..... a toroidal LHC apparatus, page 18
BIS ..... barrel inner small [34], page 25
BMS ..... barrel middle small [34], page 25
BOS ..... barrel outer small [34], page 25
CKM ..... Cabibbo-Kobayashi-Maskawa, page 5
CMS ..... compact muon solenoid, page 16
CSC ..... computing system commissioning, page 31
DAQ ..... data acquisition, page 23
EF ..... event filter, page 23
FEX ..... feature extraction, page 30
FS ..... full scan, page 39
HF ..... `HitFilter`, page 73
HLT ..... high-level trigger, page 23
LEP ..... large electron-positron collider, page 14
LHC ..... large hadron collider, page 14
LVL1 ..... first-level trigger, page 23
LVL2 ..... level 2 trigger, page 23
MC ..... Monte Carlo, page 28
MDTs ..... monitored drift tubes, page 21
RoIs ..... regions of interest, page 23
RPCs ..... resistive plate chambers, page 25
SCT ..... semiconductor tracker, page 19
SiMPLE ..... Siegen multi-processor linux environment, page 31
SM ..... standard model, page 2
SPR ..... `SpacePointReader`, page 73
TGCs ..... thin gap chambers, page 25
TRT-TET ..... `TrigTRT_TrackExtensionTool`, page 73
TRT ..... transition radiation tracker, page 19
TTC ..... timing, trigger, and control, page 24
ZF ..... `IDScanZFinder`, page 73

List of Figures

List of Tables

Bibliography

[1] S. Weinberg, *A Model of Leptons*, Phys. Rev. Lett., 19(21):1264–1266, Nov 1967.

[2] A. Salam, *Weak and Electromagnetic Interactions*, Originally printed in Svartholm: Elementary Particle Theory, Proceedings Of The Nobel Symposium Held 1968 At Lerum, Sweden, Stockholm 1968, 367-377.

[3] S.L. Glashow, J. Iliopoulos, and L. Maiani, *Weak Interactions with Lepton-Hadron Symmetry*, Phys. Rev. D, 2(7):1285–1292, Oct 1970.

[4] W.-M. Yao et al., *Review of Particle Physics*, Journal of Physics G, 33:1+, 2006.

[5] G. Feldman and J. Steinberger, *The Number of families of matter: How experiments at CERN and SLAC, using electron - positron collisions, showed that there are only three families of fundamental particles in the universe*, Sci. Am., 352N2:70–75, 1991.

[6] N. Cabibbo, *Unitary Symmetry and Leptonic Decays*, Phys. Rev. Lett., 10(12):531–533, Jun 1963.

[7] M. Kobayashi and T. Maskawa, *CP Violation in the Renormalizable Theory of Weak Interaction*, Prog. Theor. Phys., 49:652–657, 1973.

[8] A.J. Buras, W. Slominski, and H. Steger, $B^0 - \bar{B}^0$ *Mixing, CP Violation and the B Meson Decay*, Nucl. Phys., B245:369, 1984.

[9] V. Tiwari, *Measurement of the* $B_s - \bar{B}_s$ *oscillation frequency using semileptonic decays*, FERMILAB-THESIS-2007-09.

[10] A. Lenz and U. Nierste, *Theoretical update of* $B_s - \bar{B}_s$ *mixing*, JHEP, 06:072, 2007.

[11] M. Beneke, G. Buchalla, C. Greub, A. Lenz, and U. Nierste, *Next-to-leading order QCD corrections to the lifetime difference of* B_s *mesons*, Phys. Lett., B459:631–640, 1999.

[12] T. Stahl, Ph.D. thesis, University of Siegen, in preparation.

[13] S. Ben-Ami, B. Epp, P. Jussel, E. Kajomovitz, J. Kirk, E. Kneringer, M. Pontz, H. von Radziewski, Y. Rozen, T. Stahl, and W. Walkowiak for the ATLAS Collaboration, *Trigger and Analysis Strategies for Purely Hadronic B-decays*, in preparation.

[14] T. Stahl, University of Siegen, private communication.

[15] A. Dewhurst, J. Ginzburg, D. Price, and M. Smizanska, T. Stahl, and W. Walkowiak, *Low p_T muon and di-muon rates in ATLAS*, internal communication, ATL-COM-PHYS-2007-089, CERN, Geneva, Nov 2007.

[16] M. Smizanska, Lancaster University, private communication.

[17] H. Albrecht et al., *A New determination of the $B^0 - \bar{B}^0$ oscillation strength*, Z. Phys., C55:357–364, 1992.

[18] H. Albrecht et al., *A Study of $\bar{B}^0 \to D^{*+} l\bar{\nu}$ and $B^0 - \bar{B}^0$ mixing using partial D^{*+} reconstruction*, Phys. Lett., B324:249–254, 1994.

[19] John E. Bartelt et al., *Two measurements of $B^0 - \bar{B}^0$ mixing*, Phys. Rev. Lett., 71:1680–1684, 1993.

[20] E. Barberio et al., *Averages of b-hadron properties at the end of 2006*, FERMILAB-FN-0815-E, 2007.

[21] J. Abdallah et al., *Search for $B_s^0 - \bar{B}_s^0$ oscillations and a measurement of $B_d^0 - \bar{B}_d^0$ oscillations using events with an inclusively reconstructed vertex*, Eur. Phys. J., C28:155, 2003.

[22] V.M. Abazov et al., *Direct Limits on the B_s^0 Oscillation Frequency*, Phys. Rev. Lett., 97:021802, 2006.

[23] A. Abulencia et al., *Observation of $B_s - \bar{B}_s$ Oscillations*, Phys. Rev. Lett., 97:242003, 2006.

[24] *CERN FAQ – LHC the guide*, CERN, Geneva, 2006.

[25] O. Bruning (Ed.) et al., *LHC design report, Vol. I: The LHC main ring*, CERN-2004-003-V-1, June 2004.

[26] V. Shiltsev, *Status of Tevatron collider Run II and novel technologies for luminosity upgrades*, September 2007, FERMILAB-CONF-04-123-AD.

[27] C.W. Fabjan, L. Riccati, K. Safarík, and H. de Groot, *ALICE Physics Performance Technical Design Report*, CERN/LHCC/2005-030, Geneva, 2005.

[28] M. Della Negra, L. Foà, A. Hervé, and A. Petrilli, *CMS Physics Technical Design Report*, CERN/LHCC/2006-001, Geneva, 2006.

[29] *LHCb Technical Proposal*, CERN/LHCC/98-004, Geneva, 1998.

[30] ATLAS Collaboration, *ATLAS detector and physics performance TDR 14*, volume I, CERN/LHCC/99-14, May 1999.

[31] ATLAS Collaboration, *ATLAS Technical Proposal for a General-Purpose pp Experiment at the Large Hadron Collider at CERN*, CERN/LHCC/94-43, December 1994.

[32] ATLAS Collaboration, *ATLAS Calorimeter Performance TDR 1*, CERN/LHCC/96-40, December 1996.

[33] ATLAS Collaboration, *ATLAS Liquid Argon Calorimeter TDR 2*, CERN/LHCC/96-41, December 1996.

[34] ATLAS Collaboration, *ATLAS Muon Spectrometer TDR 10*, CERN/LHCC/97-22, May 1997.

[35] ATLAS Collaboration, *ATLAS High-Level Trigger, Data Acquisition and Controls TDR 016*, CERN/LHCC/2003-022, June 2003.

[36] ATLAS Collaboration, *ATLAS Level-1 Trigger TDR 12*, CERN/LHCC/98-14, June 1998.

[37] ATLAS Collaboration, *The ATLAS experiment at the CERN Large Hadron Collider*, in preparation.

[38] A. Di Mattia and L. Luminari, *Performances of the Level-1 Trigger System in the ATLAS Muon Spectrometer Barrel*, ATL-DAQ-2002-008, April 2002.

[39] G. Ünel, *Trigger and Data Acquisition system of the ATLAS experiment at CERN*, in 4th Eurasian Conference on Nuclear Science and its Applications, ATL-COM-DAQ-2007-026, 2006.

[40] S. Lloyd (Ed.) et al., *The ATLAS Computing Workbook*, December 2007, `https://twiki.cern.ch/twiki/bin/view/Atlas/WorkBook`, version r105, ATLAS twiki.

[41] T. Sjostrand, S. Mrenna, and P. Skands, *PYTHIA 6.4 physics and manual*, JHEP, 05:026, 2006.

[42] W. Walkowiak, University of Siegen, private communication.

[43] S. Kretzer, H. L. Lai, F. I. Olness, and W. K. Tung, *CTEQ6 parton distributions with heavy quark mass effects*, Phys. Rev., D69:114005, 2004.

[44] M. Smizanska, *PythiaB interface to Pythia6 dedicated to simulation of beauty events*, ATL-COM-PHYS-2003-038, August 2003.

[45] G. Folger and G. Cosmo. *Geant4*. CERN, Geneva, 2002.

[46] V. Tsulaia (Ed.) et al., *Top level tags in the ATLAS Geometry Database*, December 2007, `https://twiki.cern.ch/twiki/bin/view/Atlas/AtlasGeomDBTags`, version r26, ATLAS twiki.

[47] Monika Wielers (Ed.) et al., *TriggerMenuVersions*, July 2007, `https://twiki.cern.ch/twiki/bin/view/Atlas/TriggerMenuVersions`, version r31, ATLAS twiki.

[48] S. Rajagopalan (Ed.) et al., *L31TriggerMenu*, September 2007, `https://twiki.cern.ch/twiki/bin/view/Atlas/L31TriggerMenu`, version r8, ATLAS twiki.

[49] J. Baines, Rutherford Appleton Laboratory, private communication.

[50] J. Kirk, Rutherford Appleton Laboratory, private communication.

[51] R. Brun and F. Rademakers, *ROOT - An Object Oriented Data Analysis Framework*, in Proceedings AIHENP'96 Workshop, Lausanne, Nucl. Inst. & Meth. in Phys. Res. A 389 (1997) 81-86, September 1996, see also `http://root.cern.ch/`.

[52] T. Ullrich and Z. Xu, *Treatment of Errors in Efficiency Calculations*, arXiv:physics/0701199v1, January 2007.

[53] L. Moneta, PH/SFT, CERN, Geneva, private communication.

[54] P. Jussel (Ed.) et al., *BPhysWorkingGroupCrossSections*, November 2007, `https://twiki.cern.ch/twiki/bin/view/Atlas/BPhysWorkingGroupCrossSections`, version r20, ATLAS twiki.

[55] N.P. Konstantinidis, and H. Drevermann, *Determination of the z position of primary interactions in ATLAS 014*, ATL-DAQ-2002-014, CERN, Geneva, July 2002.

[56] N.P. Konstantinidis and H. Drevermann, *Algorithms to select space points of tracks from single primary interactions in ATLAS*, internal communication, ATL-COM-DAQ-2003-040, CERN, Geneva, August 2003.

[57] D. Emeliyanov, *The Probabilistic Data Association Filter for the fast tracking in ATLAS Transition Radiation Tracker 037*, ATL-DAQ-CONF-2006-012, ATL-COM-DAQ-2005-037, CERN, Geneva, October 2005.

[58] J. Kirk, J.T.M. Baines, and A.T. Watson, *ATLAS B-physics Trigger Studies using EM and Jet RoIs*, ATL-DAQ-PUB-2006-004, CERN, Geneva, June 2006.

Acknowledgements

I would like to express my gratitude towards all people who have supported my efforts:

- my supervisor Prof. Dr. Peter Buchholz for his support, broad view, his professional guidance, and his leadership qualities,
- my co-reviewer Prof. Dr. Markus Schumacher for his support and faith in me,
- Dr. Wolfgang Walkowiak for his help and guidance throughout my work as a masters student, fruitful and friendly discussions, and for proof-reading this thesis, and
- Thorsten Stahl for many things, amongst which I want to stress his constant readiness to help and discuss, the support while getting started and when amending the analysis code, proof-reading of this thesis, and the hardly surpassable working climate: "So long, and thanks for all the tea!" (adapted from Douglas Adams' *Hitchhiker's* series)

Furthermore, to

- Dr. Julie Kirk for source code templates, implementation of trigger analysis elements, her support, and good cooperation,
- Dr. Matthew Beckingham for great cooperation,
- Kai Grybel for his LaTeX thesis template,
- the entire experimental particle physics group for great working conditions and a good work climate,

and last, but not least, to my family and friends, who kept me out of harm's way and always helped me to see the brighter side.

Erklärung

Hiermit erkläre ich, dass ich die vorliegende Masterarbeit selbständig verfasst und keine anderen als die angegebenen Quellen und Hilfsmittel benutzt, sowie Zitate und Ergebnisse anderer kenntlich gemacht habe.

Siegen	17.12.2007	Holger von Radziewski
(Ort)	(Datum)	(Unterschrift)